



**POLITECNICO
DI TORINO**

MASTER OF SCIENCE THESIS

Combustion modelling of a NG engine using detailed chemistry in CONVERGE

Author: Lorenzo TESTA

Supervisors:
Daniela MISUL
Mirko BARATTA
Rainer ROTHBAUER

*To my mother and to Valeria
the two most important women in my life*

Table of Contents

1	Abstract	5
2	CFD modelling	7
2.1	Introduction	7
2.2	Governing equations of Fluid Flow	8
2.2.1	Introduction	8
2.2.2	Continuity equation	9
2.2.3	Momentum equation	10
2.2.4	Energy equation	13
2.2.5	Equation of State	14
2.2.6	Chemically reactive flows	15
2.3	Numerical solution methods	17
2.3.1	Discretization Approaches	18
2.4	Turbulence and its modelling	19
2.5	Converge CFD software	23
2.5.1	Grid control	24
3	NG-Engine: experimental data	29
3.1	Introduction	29
3.2	Engine main characteristic	29
3.2.1	Engine fuel	30
3.2.2	Intake system	30
3.2.3	Fuel supply system	31
3.2.4	Measuring system	32
3.3	Experimental parameters for model validation	35
3.3.1	Data conditioning	37
3.4	Operating points considered	38
3.4.1	O.P. 2000 [rpm] x 3.6 [bar] x lambda=1	38
3.4.2	O.P. 2000 [rpm] x 7.9 [bar] x lambda=1	39
3.4.3	O.P. 3300 [rpm] x 7.9 [bar] x lambda=1	41
4	NG-Engine: CFD modelling	43
4.1	Geometry and regions	43
4.2	Fuel composition	44
4.3	Boundary and Initial conditions	45
4.3.1	Boundary conditions	45
4.3.2	Initial conditions	46
4.4	Turbulence modelling	46
4.4.1	$k - \varepsilon$ models	47
4.4.2	Law of Wall	48
4.5	Ignition modelling	49
4.6	Mesh settings	50
4.6.1	"Coarse" mesh settings	50
4.6.2	"Fine" mesh settings	52

4.6.3	"Finest" mesh settings	53
5	Combustion modelling	57
5.1	Introduction	57
5.2	Chemical kinetics and its application to combustion	58
5.3	Combustion models in CONVERGE	60
5.3.1	Simplified Combustion Models in CONVERGE	60
5.4	SAGE Detailed Chemical Kinetics Solver	61
5.4.1	Mechanisms used	63
5.4.2	Mechanisms validation and comparison	66
5.4.3	Mechanism reduction	74
6	Results and conclusions	83
6.1	Introduction	83
6.2	O.P. 2000[rpm] x 3.6[bar] x lambda=1	83
6.2.1	Pure CH ₄	84
6.2.2	Actual fuel composition	114
6.3	2000[rpm] x 7.9[bar] x lambda=1	119
6.4	3300[rpm] x 7.9[bar] x lambda=1	129
6.5	Conclusions and future developments	132
7	Acknowledgements	135
8	Nomenclature	137
9	Acronyms	141
10	List of figures	143
11	List of tables	151
12	Bibliography	153

Abstract

This thesis project fits in the study and the development of the combustion modelling of natural gas (NG) engines, by means of the powerful tool of the CFD analysis. CFD, namely "*Computational fluid dynamics*", is a branch of fluid mechanics in which the use of numerical analysis and data structures is involved to solve problems regarding fluid flows; it is a very well-established tool used in lots of engineering applications, since it provides great time and cost reduction in designing. The CFD commercial code used is **CONVERGE**, a new and innovative software which saves a great deal of time, as it automatically generates the mesh and contains sophisticated algorithms to refine it locally.

The work supports the European research project *GasOn*, whose aim is to develop low environmental impact engines, and has been carried out at the CFD company **Convergent Science GmbH** (Austria) by using experimental data regarding a *Fiat FIRE 1.4 16V Turbo CNG* engine gathered at the DENERG laboratories, in **Politecnico di Torino**.

The project is focused on the *SAGE detailed chemistry* model, coupled with several reaction mechanisms of chemical kinetics, and involves also a thorough validation against the aforementioned experimental data.

The study accomplished can be split into four main parts, all linked together.

The first part deals with the validation of the different reaction mechanisms considered, by comparing 0-D and 1-D simulations results in the matter of ignition delay and laminar flame speed against experimental data found in literature. This part also involves 0-D and 1-D simulations at conditions close to those characterizing the operating points taken into consideration from the engine experimental data available, in order to see how differently the reaction mechanisms might behave.

The second part concerns the reaction mechanisms reduction, in order to reduce the simulations runtime. In **CONVERGE** the reduction can be made in two ways, i.e. skeletal or dynamic; the first is implemented *before* the simulation, while the second *during* that.

The third part copes with the engine fuel: two different compositions have been involved, i.e. "*Pure CH₄*" and one closer to the real fuel, as it takes into account, beyond the methane, other species (small) percentages present in the original fluid; the latter is here named as "*Actual fuel composition*".

The fourth part handles the choice of the best mesh settings to couple with the mechanisms for the engine operating points treated. Three meshes have been considered, i.e. a coarser one, called "*Coarse*", a finer one, named "*Fine*", and an even more finer one, called "*Finest*". The mechanisms have been thus compared for the different meshes.

CFD modelling

2.1 Introduction

Computational fluid dynamics (CFD) is the analysis of systems involving fluid flow, heat transfer and associated phenomena such as chemical reactions by means of computer-based simulations, spanning a wide range of industrial and non-industrial applications and areas.

CFD techniques have become more and more popular with the availability of high performance computing hardware and the introduction of user-friendly interfaces, leading to a more and more complete description of fluid flow in less time cost. Nowadays, CFD is becoming a vital component in the design of industrial product and processes.

There are several unique advantages of CFD over experiment-based approaches to fluid system design, such as the substantial reduction of lead times and costs of new designs, the ability to study systems where controlled experiments are difficult or impossible to perform, the possibility to study systems under hazardous conditions at and beyond their normal performance limits and the practically unlimited level of detail of results.

CFD codes are structured around the numerical algorithms that can tackle fluid flow problems. All codes typically contain three main elements:

Pre-processor: it consists of the input of a flow problem to a CFD program by means of an operator-friendly interface and the subsequent transformation of this input into a suitable form for the solver. The activities involve the definition of the geometry and the physical bounds of the region of interest, the grid generation, the selection of the physical and chemical phenomena that need to be modelled (e.g. definition of the equations of fluid motion), the definition of fluid properties, and the specification of appropriate boundary conditions at cells which coincide with or touch the domain boundaries;

Solver: it solves iteratively the equations of fluid motion as a steady-state or transient by means of numerical techniques, e.g. *Finite elements method*, *Finite differences method*, or *Finite volume method*;

Post-processor: it allows the user to analyse and visualise the results of the simulation. Nowadays the leading CFD packages are equipped with versatile data visualization tools. These include: domain geometry and grid display, vector plots, line and shaded control plots, 2D and 3D surface plots, particle tracking, view manipulation, colour post script output, animation for dynamic result display.

Before going any further, the fundamental basis of the CFD problems will be described, i.e. the governing equations of fluid flow, the numerical solution methods and turbulence.

2.2 Governing equations of Fluid Flow

2.2.1 Introduction

As previously introduced, Computational Fluid Dynamics (CFD) provides a cost effective means of simulating real flows by the numerical solution of the governing equations.

Fluids are substances whose molecular structure offers no resistance to external shear deformation. Although a significant distinction exists between liquids and gases, both types of fluids obey the same laws of motion. In most cases of interest, a fluid can be regarded as continuum, i.e. a continuous substance.

Fluid flow is caused by the action of externally applied forces, e.g. pressure differences, gravity, shear, rotation, and surface tension. They can be classified as surface forces (e.g. shear force or pressure) and body forces (e.g. gravity and forces induced by rotation).

Even though all fluids show a similar behaviour under the action of external forces, their macroscopic properties differ considerably. Density and viscosity can be regarded as the most important properties of simple fluids, while others, such as Prandtl number, specific heat, and surface tension affect fluid flows only under certain conditions, e.g. when there are large temperature differences. Fluid properties are functions of other thermodynamic variables (e.g. temperature and pressure). Also fluid flow affects in a considerable way its properties; at low enough speeds, the inertia of the fluid may be ignored and we have creeping flow. This regime is of importance in flows containing small particles (suspensions), in flows through porous media or in narrow passages (coating techniques, micro-devices). As the speed is increased, inertia becomes important but each fluid particle follows a smooth trajectory; the flow is then said to be laminar. Further increases in speed may lead to instability that eventually produces a more random type of flow that is called turbulent; the process of laminar-turbulent transition is an important area in its own right. The ratio of the flow speed on the local speed of sound in the fluid (the Mach number, Ma) is an other important parameter determining the fluid properties: for small Mach numbers, $Ma < 0.3$, the flow may be considered incompressible; otherwise, it is compressible. If $Ma < 1$, the flow is called subsonic; when $Ma > 1$, the flow is supersonic and shock waves are possible. Finally, for $Ma > 5$, the compression may create high enough temperatures to change the chemical nature of the fluid; such flows are called hypersonic. These distinctions affect the mathematical nature of the problem and therefore the solution method.

In many flows, the effects of viscosity are important only near walls, so that the flow in the largest part of the domain can be considered as inviscid. There are several viscosity laws; in this thesis work the Newton's law of viscosity will be the only one considered.

Many other phenomena affect fluid flow, such as temperature differences, differences in concentration of solutes, phase changes (boiling, condensation, melting and freezing). [1]

The cornerstone of computational fluid dynamics is the fundamental governing equations of fluid dynamics: the continuity, the momentum and the energy equations. Before developing any computational solutions to any problem, it is necessary to derive and understand the physical meaning of these equations, which are the mathematical statements of three fundamental physical principles upon which all of fluid dynamics is based:

- Mass is conserved;
- Newton's second law: $\mathbf{F} = m\mathbf{a}$;
- Energy is conserved.

The equation that comes from applying the conservation of mass law to a fluid flow is called the *Continuity equation*. The conservation of momentum applied to a fluid flow yields a vector equation known as the *Momentum equation*. The conservation of energy law is identical to the first law of thermodynamics and the resulting fluid dynamic equation is named *Energy equation*. In addition to the equations developed from these universal laws, it is necessary to establish relationships between fluid properties in order to close the system of equations. An example of such a relationship is the equation of state, which relates the thermodynamic variables pressure p , density ρ and temperature T . [7]

These physical principles must be applied to a suitable model of the flow; there are two main models for the fluid flow:

"Eulerian model" , or *Finite control volume model*, is a way of looking at fluid motion that focuses on specific locations (finite control volume) in the space through which the fluid flows as time passes;

"Lagrangian model" or *Infinitesimal fluid element model*, is a way of looking at fluid motion where the observer follows an individual fluid parcel (infinitesimal fluid element) as it moves through space and time.

In the *Eulerian approach*, the control volume is a reasonably large, finite region of the flow. The fundamental physical principles are applied to the fluid inside the control volume. Therefore, instead of looking at the whole flow field at once, with the control volume model the attention is limited to just the fluid in the finite region of the volume itself. The fluid flow equations that are directly obtained by applying the fundamental physical principles to a finite control volume are in integral form. These integral forms of the governing equations can be manipulated to indirectly obtain partial differential equations.

In the *Lagrangian approach* the fluid element is infinitesimal in the same sense as differential calculus; however, it is large enough to contain a huge number of molecules so that it can be viewed as a continuous medium. The fluid element may be fixed in space with the fluid moving through it, or it may be moving along a streamline with a vector velocity equal to the flow velocity at each point. Again, instead of looking at the whole flow field at once, the fundamental physical principles are applied to just the fluid element itself. This application leads directly to the fundamental equations in partial differential equation form.

In this section the governing equations of fluid flow will be derived, without going too much into detail on all the steps.

2.2.2 Continuity equation

The *Lagrangian approach* is considered first. The mass of the fluid particle, δm , is fixed and occupies a volume δV . Therefore:

$$\delta m = \rho \delta V \quad (2.1)$$

The mass conservation principle states that the time-rate-of-change of the mass of the fluid element is zero as the element moves along with the flow, so:

$$\frac{D(\delta m)}{Dt} = 0 \quad (2.2)$$

where $\frac{D(\delta m)}{Dt}$ is time rate of change of mass of the given fluid element as it moves through space (substantial derivative).

Combining equations 2.1 and 2.2:

$$\frac{D(\rho \delta V)}{Dt} = \delta V \frac{D\rho}{Dt} + \rho \frac{D(\delta V)}{Dt}$$

Dividing by δV and applying the physical meaning of $\nabla \cdot \mathbf{v}$, which is the time rate of change of the volume of a moving fluid element per unit volume, the continuity equation is obtained:

$$\frac{D\rho}{Dt} + \rho \nabla \cdot \mathbf{v} = 0 \quad (2.3)$$

The *Eulerian approach* is now considered. At a point on the control surface, the flow velocity is \mathbf{v} , the vector elemental surface area is $d\mathbf{S}$ and dV is an elemental volume inside the finite control volume. The mass conservation principle applied to this control volume acquires now the following meaning: the rate of change of the mass inside the control volume is equal to the net rate of mass flowing through the surface that bounds the volume. The mathematical expression of this physical statement is:

$$\frac{\partial \rho}{\partial t} + \nabla \cdot (\rho \mathbf{v}) = 0 \quad (2.4)$$

which is the continuity equation in the Eulerian approach.

For a Cartesian coordinate system, where v_x, v_y, v_z represent the x, y, z components of the velocity vector, equation 2.4 becomes:

$$\frac{\partial \rho}{\partial t} + \frac{\partial}{\partial t}(\rho v_x) + \frac{\partial}{\partial t}(\rho v_y) + \frac{\partial}{\partial t}(\rho v_z) = 0 \quad (2.5)$$

The continuity equation can be also expressed in integral form, by integrating eq. 2.4 over the entire fluid volume V :

$$\frac{\partial}{\partial t} \iiint_V \rho dV + \iint_S \rho \mathbf{v} d\mathbf{S} = 0 \quad (2.6)$$

A flow in which the density of each fluid element remains constant is called *incompressible*. Mathematically, this implies that:

$$\frac{D\rho}{Dt} = 0$$

which reduces eq. 2.3 to:

$$\nabla \cdot \mathbf{v} = 0 \quad (2.7)$$

or eq. 2.5 to:

$$\frac{\partial v_x}{\partial t} + \frac{\partial v_y}{\partial t} + \frac{\partial v_z}{\partial t} = 0 \quad (2.8)$$

For steady air flows with speed <100 m/s the assumption of incompressibility is a good approximation.[7]

2.2.3 Momentum equation

The momentum equation provides a mathematical expression of Newton's second law applied to fluids, which states that the net force on the fluid element is equal to its mass multiplied by the acceleration of the fluid element. This is a vector relation; therefore it can be split into three scalar expressions: along the $x, y,$ and z -axes. The forces acting on the particle can be distinguished into:

Body forces , which are forces acting directly on the volumetric mass of the fluid element. These forces "act at a distance"; examples are gravitational, electric and magnetic forces, Coriolis forces;

Surface forces , which act directly on the surface of the fluid element. They are due to the pressure distribution acting on the surface, imposed by the outside fluid surrounding the fluid element, and the shear and normal stress distributions acting on the surface, also imposed by the outside fluid "tugging" or "pushing" on the surface by means of friction.

For the derivation of the momentum equation, the x-axis and the *Lagrangian approach* will be the considered; the mathematical expression of the aforementioned physical principle along the x-axis is:

$$F_x = ma_x \quad (2.9)$$

Focusing on the left hand side of 2.9, in particular on the body forces, and denoting the body force per unit mass acting on the fluid element by \mathbf{f} (with f_x its x-component), it holds:

$$\{\text{Body force on the fluid element in the } x \text{ direction}\} = \rho f_x dx dy dz$$

where $dx dy dz$ is the volume of the fluid element.

The surface forces are now considered and sketched in Fig. 2.1. According to the

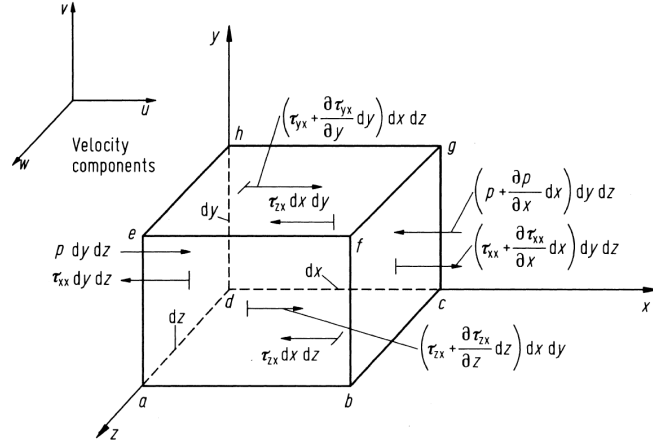


Figure 2.1: Surface forces in the x-direction exerted on the fluid element

convention in Fig. 2.1, the summation of the surface forces on the moving fluid element in the x-direction is:

$$\begin{aligned} \{\text{Net surface force in the } x \text{ direction}\} &= \left[p - \left(p + \frac{\partial p}{\partial x} dx \right) \right] dy dz + \\ &+ \left[\left(\tau_{xx} + \frac{\partial \tau_{xx}}{\partial x} dx \right) - \tau_{xx} \right] dy dz + \left[\left(\tau_{xy} + \frac{\partial \tau_{xy}}{\partial y} dy \right) - \tau_{xy} \right] dx dz + \\ &+ \left[\left(\tau_{xz} + \frac{\partial \tau_{xz}}{\partial z} dz \right) - \tau_{xz} \right] dx dy \quad (2.10) \end{aligned}$$

where τ_{xx} is the normal stress in x-direction and τ_{xy} and τ_{xz} are the shear stresses in the other directions.

Therefore the left hand side of Eq. 2.9 is:

$$F_x = \left(-\frac{\partial p}{\partial x} + \frac{\partial \tau_{xx}}{\partial x} + \frac{\partial \tau_{xy}}{\partial y} + \frac{\partial \tau_{xz}}{\partial z} \right) dx dy dz + \rho f_x dx dy dz \quad (2.11)$$

Considering the right-hand side of Eq. 2.9 and recalling that the mass of the fluid element is fixed and is $m = \rho \cdot dx dy dz$ and that the acceleration of the fluid element is the time-rate-of-change of its velocity, it is possible to write:

$$ma_x = \rho \cdot dx dy dz \cdot \frac{Dv_x}{Dt} \quad (2.12)$$

where the substantial derivative has been adopted since the *infinitesimal fluid element* model is here considered.

By combining Eqs. 2.12, 2.11 and 2.9, the x-component of the momentum equation for a viscous flow is obtained, i.e.:

$$\rho \frac{Dv_x}{Dt} = -\frac{\partial p}{\partial x} + \frac{\partial \tau_{xx}}{\partial x} + \frac{\partial \tau_{xy}}{\partial y} + \frac{\partial \tau_{xz}}{\partial z} + \rho f_x \quad (2.13)$$

For the y- and z- components respectively, it holds:

$$\rho \frac{Dv_y}{Dt} = -\frac{\partial p}{\partial y} + \frac{\partial \tau_{yy}}{\partial y} + \frac{\partial \tau_{yx}}{\partial x} + \frac{\partial \tau_{yz}}{\partial z} + \rho f_y \quad (2.14)$$

$$\rho \frac{Dv_z}{Dt} = -\frac{\partial p}{\partial z} + \frac{\partial \tau_{zz}}{\partial z} + \frac{\partial \tau_{zx}}{\partial x} + \frac{\partial \tau_{zy}}{\partial y} + \rho f_z \quad (2.15)$$

whose compact form can be written as:

$$\rho \frac{D\mathbf{v}}{Dt} = \rho \mathbf{f} + \nabla \cdot \mathbf{P}_{ij} \quad (2.16)$$

where \mathbf{P}_{ij} is the stress tensor, which represents the surface forces per unit volume, whose components contain the normal and the shearing stresses (τ_{ii} and τ_{ij}).

Eqs. 2.13, 2.14 and 2.15 are scalar equations, and are called the *Navier-Stokes* equations in honour of Frenchman M. Navier and G. Stokes, who independently obtained the equations in the first half of the nineteenth century.

The shear stress, τ_{xy} , and the normal stresses, τ_{xx} , in a fluid are related to the time-rate-of-change of the deformation of the fluid element: τ_{xy} is related to the time rate-of-change of the shearing deformation of the fluid element, while τ_{xx} is related to the time-rate-of-change of volume of the fluid element. According to Isaac Newton, shear stress in a fluid is proportional to the time-rate-of-strain, i.e. velocity gradients. Such fluids are called *Newtonian fluids*; most of the fluids can be considered Newtonian. For this kind of fluids it holds:

$$\begin{aligned} \tau_{xx} &= -\frac{2}{3}\mu \nabla \cdot \mathbf{v} + 2\mu \frac{\partial v_x}{\partial x} \\ \tau_{yy} &= -\frac{2}{3}\mu \nabla \cdot \mathbf{v} + 2\mu \frac{\partial v_y}{\partial y} \\ \tau_{zz} &= -\frac{2}{3}\mu \nabla \cdot \mathbf{v} + 2\mu \frac{\partial v_z}{\partial z} \\ \tau_{xy} = \tau_{yx} &= \mu \left(\frac{\partial v_x}{\partial x} + \frac{\partial v_y}{\partial y} \right) \\ \tau_{xz} = \tau_{zx} &= \mu \left(\frac{\partial v_x}{\partial x} + \frac{\partial v_z}{\partial z} \right) \\ \tau_{yz} = \tau_{zy} &= \mu \left(\frac{\partial v_y}{\partial y} + \frac{\partial v_z}{\partial z} \right) \end{aligned}$$

Therefore, the complete *Navier-Stokes* equations are:

$$\begin{aligned} \rho \frac{Dv_x}{Dt} = \rho f_x - \frac{\partial p}{\partial x} + \frac{\partial}{\partial x} \left[\frac{2}{3}\mu \left(2\frac{\partial v_x}{\partial x} - \frac{\partial v_y}{\partial y} - \frac{\partial v_z}{\partial z} \right) \right] + \\ + \frac{\partial}{\partial y} \left[\mu \left(\frac{\partial v_x}{\partial y} + \frac{\partial v_y}{\partial x} \right) \right] + \frac{\partial}{\partial z} \left[\mu \left(\frac{\partial v_x}{\partial z} + \frac{\partial v_z}{\partial x} \right) \right] \end{aligned} \quad (2.17)$$

$$\begin{aligned} \rho \frac{Dv_y}{Dt} = \rho f_y - \frac{\partial p}{\partial y} + \frac{\partial}{\partial y} \left[\frac{2}{3}\mu \left(2\frac{\partial v_y}{\partial y} - \frac{\partial v_x}{\partial x} - \frac{\partial v_z}{\partial z} \right) \right] + \\ + \frac{\partial}{\partial x} \left[\mu \left(\frac{\partial v_y}{\partial x} + \frac{\partial v_x}{\partial y} \right) \right] + \frac{\partial}{\partial z} \left[\mu \left(\frac{\partial v_y}{\partial z} + \frac{\partial v_z}{\partial y} \right) \right] \end{aligned} \quad (2.18)$$

$$\rho \frac{Dv_z}{Dt} = \rho f_z - \frac{\partial p}{\partial z} + \frac{\partial}{\partial z} \left[\frac{2}{3} \mu \left(2 \frac{\partial v_z}{\partial z} - \frac{\partial v_x}{\partial x} - \frac{\partial v_y}{\partial y} \right) \right] + \frac{\partial}{\partial x} \left[\mu \left(\frac{\partial v_z}{\partial x} + \frac{\partial v_x}{\partial z} \right) \right] + \frac{\partial}{\partial y} \left[\mu \left(\frac{\partial v_z}{\partial y} + \frac{\partial v_y}{\partial z} \right) \right] \quad (2.19)$$

If the flow is incompressible and the coefficient of viscosity μ is assumed to be constant, the *Navier-Stokes* equation will reduce to:

$$\rho \frac{D\mathbf{v}}{Dt} = \rho \mathbf{f} - \nabla p + \mu \nabla^2 \mathbf{v} \quad (2.20)$$

[4]

2.2.4 Energy equation

The energy equation is the mathematical expression of the first law of thermodynamics, which states that heat is a form of energy; this means that thermodynamic processes follow the principle of conservation of energy. Heat energy, therefore, cannot be created or destroyed; nevertheless, it can be transferred from one location to another and converted to and from other forms of energy. The rate of change of energy is equal to the sum of the rate of heat addition and the rate of work done on a fluid particle.

The first law of thermodynamics applied to a fluid passing through an infinitesimal, fixed control volume yields the following energy equation:

$$\frac{\partial E_t}{\partial t} + \nabla \cdot E_t \mathbf{v} = \frac{\partial Q}{\partial t} - \nabla \cdot \mathbf{q} + \rho \mathbf{f} + \nabla \cdot (\mathbf{P}_{ij} \cdot \mathbf{v}) \quad (2.21)$$

where E_t is the total energy per unit volume given by:

$$E_t = \rho \left(e + \frac{v^2}{2} + \text{potential energy} + \dots \right) \quad (2.22)$$

and e is the internal energy per unit mass.

The terms on the left hand side of eq. 2.21 are respectively the rate of increase of E_t in the control volume and the rate of total energy lost by convection (per unit volume) through the control surface. The terms on the right hand side are respectively the rate of heat produced per unit volume by external agencies, the rate of heat lost by conduction (per unit volume) through the control surface, the work done on the control volume by the body forces (per unit volume), and the work done by the surface forces.

The term $\nabla \cdot \mathbf{q}$ can be written in a different way, since, according to the Fourier's law for heat transfer, it holds:

$$\mathbf{q} = -k \nabla T \quad (2.23)$$

where k is the coefficient of thermal conductivity and T is the temperature. For a Cartesian coordinate system, eq. 2.21 becomes:

$$\begin{aligned} \frac{\partial E_t}{\partial t} - \frac{\partial Q}{\partial t} - \rho(f_x v_x + f_y v_y + f_z v_z) + \\ + \frac{\partial}{\partial x} (E_t v_x + p v_x - v_x \tau_{xx} - v_y \tau_{xy} - v_z \tau_{xz} + q_x) + \\ + \frac{\partial}{\partial y} (E_t v_y + p v_y - v_x \tau_{xy} - v_y \tau_{yy} - v_z \tau_{yz} + q_y) + \\ + \frac{\partial}{\partial z} (E_t v_z + p v_z - v_x \tau_{xz} - v_y \tau_{yz} - v_z \tau_{zz} + q_z) \end{aligned} \quad (2.24)$$

Using the continuity equation, the left hand side of eq. 2.21 can be written as:

$$\frac{\partial E_t}{\partial t} + \nabla \cdot E_t \mathbf{v} = \rho \frac{D}{Dt} \left(\frac{E_t}{\rho} \right) = \rho \frac{De}{Dt} + \rho \frac{D}{Dt} \frac{v^2}{2} \quad (2.25)$$

with the assumption that only kinetic and internal energy are significant in eq. 2.22. By making the scalar product and considering eq. 2.16, it holds:

$$\rho \frac{D\mathbf{v}}{Dt} \cdot \mathbf{v} = \rho \mathbf{f} \cdot \mathbf{v} + \nabla p \cdot \mathbf{v} + (\mathbf{t}_{ij}) \cdot \mathbf{v} \quad (2.26)$$

Combining eqs. 2.25 and 2.26 and substituting into 2.21, it holds:

$$\rho \frac{De}{Dt} + p(\nabla \cdot \mathbf{v}) = \frac{\partial Q}{\partial t} - \nabla \cdot \mathbf{q} + \nabla \cdot (\mathbf{t}_{ij} \cdot \mathbf{v}) - (\nabla \cdot \mathbf{t}_{ij}) \cdot \mathbf{v} \quad (2.27)$$

the last two terms of the right hand side can be combined into a single term, Φ , which is called the dissipation function. It represents the rate at which the mechanical energy is expended in the process of deformation of the fluid due to viscosity. Equation 2.27 thus becomes:

$$\rho \frac{De}{Dt} + p(\nabla \cdot \mathbf{v}) = \frac{\partial Q}{\partial t} - \nabla \cdot \mathbf{q} + \Phi \quad (2.28)$$

Considering the definition of enthalpy, i.e. $h = e + \frac{p}{\rho}$, and the continuity equation, equation 2.28 can be rewritten as:

$$\rho \frac{Dh}{Dt} = \frac{Dp}{Dt} + \frac{\partial Q}{\partial t} - \nabla \cdot \mathbf{q} + \Phi \quad (2.29)$$

which, for an incompressible flow and with the assumption of a constant thermal conductivity, is:

$$\rho \frac{De}{Dt} = \frac{\partial Q}{\partial t} + k \nabla^2 T + \Phi \quad (2.30)$$

[7]

2.2.5 Equation of State

The governing equation of fluid dynamics are, as seen, a coupled system of non-linear partial differential equations, and therefore are very difficult to solve analytically; in fact, there is no general closed-form solution to these equations.

The system contains five equations in terms of several unknown flow-field variables, i.e. ρ , p , v_x , v_y , v_z , e , T .

As previously introduced, it is necessary to establish relations between the thermodynamic variables (p , ρ , T , e , h) in order to close the system of fluid dynamic equations (i.e. *equations of state*), as well as to relate the transport properties (μ , k) to those variables.

According to the state principle of thermodynamics, the local thermodynamic state is fixed by any two independent thermodynamic variables, provided that the chemical composition of the fluid is not changing owing to diffusion or finite-rate chemical reactions.

For most problems in gas dynamics, it is possible to assume a *perfect gas*, which means that the gas intermolecular forces are negligible. A perfect gas is subjected to the perfect gas equation of state, which is:

$$p = \rho RT \quad (2.31)$$

where R is the gas constant.

The intermolecular forces become important under conditions of high pressure and relatively low temperature. For these conditions, the gas no longer obeys to the perfect gas equation of state, and an alternative equation of state must be used, e.g.

the *Waals equation of state*.

For problems involving a perfect gas at relatively low temperatures, it is possible to also assume a *calorically perfect gas*, which means that the gas is a perfect gas with constant specific heats, namely c_v , c_p and their ratio γ .

Coefficient of viscosity μ and thermal conductivity k can be related to thermodynamic variables using kinetic theory, e.g. *Sutherland's* formulas for viscosity and thermal conductivity. [7]

2.2.6 Chemically reactive flows

The assumption of a *calorically perfect gas* is valid if intermolecular forces are negligible and the temperature is relatively low. As the temperature of the gas increases, the gas can no longer be considered as calorically perfect; in fact, the vibrational energy of the molecules becomes excited and the specific heats c_p and c_v are function of temperature. It is very common to assume the fluid as *thermally perfect*, which means that the specific heats are only function of temperature. As the temperature of the gas increases further, chemical reactions (e.g. dissociation) begin to take place and the gas is no longer thermally perfect. For most chemically reacting gases, it is possible to assume that the intermolecular forces are negligible, and, hence, each individual species obeys to the perfect gas equation of state, whose equation of state can be written as:

$$p = \rho \frac{\mathcal{R}}{\mathcal{M}} T \quad (2.32)$$

where \mathcal{R} is the universal gas constant [83140.34 J/(kg mol K)] and \mathcal{M} is the molecular mass of the mixture of gases.

The molecular weight of the mixture can be calculated using

$$\mathcal{M} = \left(\sum_{i=1}^n \frac{c_i}{\mathcal{M}_i} \right)^{-1} \quad (2.33)$$

in which c_i and \mathcal{M}_i are respectively the mass fraction and the molecular weight of species i .

The species mass fractions in a reacting mixture of gases are determined by solving the species continuity equations, which are given by

$$\frac{\partial \rho_i}{\partial t} + \nabla \cdot [\rho_i (\mathbf{v} + \mathbf{u}_i)] = \dot{\omega}_i \quad (2.34)$$

where ρ_i is the species density, \mathbf{u}_i is the species diffusion velocity and $\dot{\omega}_i$ is the rate of production of species i due to chemical reactions.

The rate of production of each species $\dot{\omega}_i$ is evaluated by using an appropriate chemistry model to simulate the reacting mixture. A chemistry model consists of m reactions, n species and n_t reactants and can be symbolically represented as

$$\sum_{i=1}^{n_t} \nu'_{l,i} A_i = \sum_{i=1}^{n_t} \nu''_{l,i} A_i \quad (2.35)$$

with $l = 1, 2, \dots, m$, $\nu'_{l,i}$ and $\nu''_{l,i}$ as stoichiometric coefficients and A_i as the chemical symbol for the i th reactant.

Once the chemistry model is specified, the rate of production of species i can be computed using the law of mass action (Vincenti and Kruger, 1965):

$$\dot{\omega}_i = \mathcal{M}_i \sum_{i=1}^m (\nu''_{l,i} - \nu'_{l,i}) \left[K_{fi} \prod_{j=1}^{n_t} (\rho \gamma_j)^{\nu'_{l,j}} - K_{bi} \prod_{j=1}^{n_t} (\rho \gamma_j)^{\nu''_{l,j}} \right] \quad (2.36)$$

where γ_j is the mole-mass ratio of reactants, and K_{fi} and K_{bi} are the forward and backward reaction rates for the l th reaction, which are functions of temperature and

can be expressed in the modified Arrhenius form as:

$$K_{fi} = \exp\left(\ln K_1 + \frac{K_2}{T} + K_3 \ln T\right)$$

$$K_{bi} = \exp\left(\ln K_4 + \frac{K_5}{T} + K_6 \ln T\right)$$

Depending on the rate of reaction rates, a chemically reacting mixture of gases can be classified as:

Frozen: if the reaction rates are essentially zero, so the rate of production of species i $\dot{\omega}_i$ is zero;

In chemical equilibrium: if the reaction rates approach infinity;

In chemical non-equilibrium: if the reaction rates are finite and eq. 2.36 is used to find $\dot{\omega}_i$.

The thermodynamic properties of a chemically reacting mixture of gas in chemical non-equilibrium are functions of both temperature and mass fractions.

2.3 Numerical solution methods

As previously introduced, flows and related phenomena can be described by partial differential equations that cannot be solved analytically except in special cases. To obtain an approximate solution numerically, discretization methods are needed; they approximate the differential equations to a system of algebraic equations, which can then be solved on a computer.

The approximations are applied to small domains in space and/or time so the numerical solution provides results at discrete locations in space and time.

Numerical results are always approximate, since first of all the differential equations may contain idealizations, then the discretization process yields other approximations, while the iterative methods used for solving the discretized equations add further inexactnesses to the solution, unless they are run for a very long time.

When the governing equations are known accurately (e.g. the Navier-Stokes equations for incompressible Newtonian fluids), solutions of any desired accuracy can be achieved in principle. However, for many phenomena (e.g. turbulence, combustion, and multiphase flow) the exact equations are either not available or numerical solution is not feasible. This makes introduction of models a necessity.

Even if the equations are solved exactly, the solution would not be a correct representation of reality. In order to validate the models, one has to rely on experimental data. Discretization errors can be reduced by applying the approximations to smaller regions but this usually increases the time and cost of obtaining the solution. Compromise is usually needed.

Each numerical solution method is composed by:

Mathematical model: it consists in the set of partial differential or integro-differential equations (e.g. the Navier-Stokes equations) and boundary conditions. The mathematical model must be appropriate for the application considered (e.g. incompressible, turbulent, laminare, 2-D or 3-D, etc.);

Discretization Method: it approximates the differential equations to a system of algebraic equations, whose variables are located at some small discrete locations in space and time. The main approaches are: the *finite difference method*, the *finite volume method* and the *finite element method*. Some examples of other methods are the *spectral schemes method* and the *boundary element method*, whose use is limited to special classes of problems. All the methods should yield the same solution if the grid is very fine;

Coordinates: The conservation equations can be written in many different forms, depending on the coordinate system and the basis vectors used. For example one can select Cartesian, cylindrical, spherical, curvilinear orthogonal or non-orthogonal coordinate systems, which may be fixed or moving. The choice depends on the target flow, and may influence the discretization method and grid type to be used;

Numerical grid: it defines the discrete locations at which the variables are to be calculated. The numerical grid (or mesh) is essentially a discrete representation of the geometric domain on which the problem is to be solved. It divides the solution domain into a finite number of subdomains (elements, control volumes etc.). There are several kinds of grid, e.g. *structured grid* (identified by regular connectivity), *block structured grid* (in which there is a two or more level subdivision of solution domain), *unstructured grid* (which is the most flexible type of grid as it can fit an arbitrary solution domain boundary, thanks to the fact that the elements or control volumes may have any shape). By transforming a physical region to a simpler region, one removes the complication of the shape of the physical region from the problem. The accuracy of a CDF solution depends

on the number of cells in the grid. Generally speaking, the bigger the number of the cells, the higher the solution accuracy. Both the accuracy of a solution and its cost in terms of necessary computer hardware and calculation time are dependent on the dimensions of the grid. The knowledge of the system under observation is therefore crucial for the right choice of the mesh settings. Setting a mesh refinement in some critical regions (e.g. where there are flow deviations, or where particular phenomena happen, such as injection or ignition in an internal combustion engine) could lead to accurate results, while for computational time saving a coarse grid could be applied in the rest of the geometry. The grid could also be adjusted finer or a coarser according to the evolution in time of the simulation. If the simulation is not steady state a finer mesh may be used when the rate of variation of the thermo-physical quantity is higher, while a coarser one is to be preferred during non-critical simulation times;

Solution method: Discretization yields a large system of non linear algebraic equations. Since the equations are non-linear, an iteration scheme is used to solve them. These methods use successive linearization of the equations and the resulting linear systems are almost always solved by iterative techniques. The choice of solver depends on the grid type and the number of nodes involved in each algebraic equation;

Convergence criteria: it states when to stop the iterative process, e.g. by taking into account the desired accuracy level.

The numerical solution method should have some important properties, i.e.:

Consistency: the difference between the discretized equations and the exact ones, i.e. the truncation error, must become zero when the grid spacing tends to zero;

Stability: the numerical solution does not amplify the errors appearing during the numerical solution process, nor damp out small fluctuations in the input data;

Convergence: the solution of the discretized equations tends to the exact solution of the differential equation as the grid spacing tends to zero. If the method is stable and all the approximations used in the discretization process are consistent, the solution usually converges to a grid-independent solution;

Conservation: the numerical scheme should respect the conservation laws, since the equations to be solved are the mathematical expression of those laws. This means that, at steady state and in absence of sources, the amount of a conserved property leaving a closed volume must be equal to the amount entering that volume. This property is really important since it imposes a constraint on the solution error.

Boundedness: numerical solutions must lie within proper bounds;

Accuracy: numerical solutions always include three kinds of errors, i.e. *modelling errors* (difference between the actual flow and the exact solution of the mathematical model), *discretization errors* (difference between the exact solution of the conservation equations and the exact solution of the algebraic system of equations obtained by discretizing these equations), and *iteration errors* (difference between the iterative and the exact solutions of the algebraic equations systems).

2.3.1 Discretization Approaches

Finite Difference Method

The starting point of the *Finite Difference Method* is the conservation equation in differential form. The solution domain is covered by a grid. At each grid point, the

differential equation is approximated by replacing the partial derivatives by approximations in terms of the nodal values of the functions. The result is one algebraic equation per grid node, in which the variable value at that and a certain number of neighbour nodes appear as unknowns.

On structured grids, this method is very simple and effective.

The disadvantage of the *Finite Difference Method* is that the conservation is not enforced unless special care is taken. Also, the restriction to simple geometries is a significant disadvantage in complex flows.

Finite Volume Method

The *Finite Volume Method* method uses the integral form of the conservation equations as its starting point. The solution domain is subdivided into a finite number of contiguous control volumes, and the conservation equations are applied to each of them. At the centroid of each control volume lies a computational node at which the variable values are to be calculated. Interpolation is used to express variable values at the control volume surface in terms of the nodal values. Surface and volume integrals are approximated using suitable quadrature formulae. As a result, one obtains an algebraic equation for each CV, in which a number of neighbour nodal values appear. The *Finite Volume Method* can accommodate any type of grid, so it is suitable for complex geometries.

This approach is probably the simplest to understand and to program.

Finite Element Method

The *Finite Element Method* is similar to the *Finite Volume Method*. The domain is broken into a set of discrete volumes or finite elements that are generally unstructured. The distinguishing feature of this method is that the equations are multiplied by a weight function before they are integrated over the entire domain. In the simplest case, the solution is approximated by a linear shape function within each element in a way that guarantees continuity of the solution across element boundaries. Such a function can be constructed from its values at the corners of the elements. The weight function is usually of the same form. This approximation is then substituted into the weighted integral of the conservation law and the equations to be solved are derived by requiring the derivative of the integral with respect to each nodal value to be zero; this corresponds to selecting the best solution within the set of allowed functions (the one with minimum residual). The result is a set of non-linear algebraic equations.

An important advantage of finite element methods is the ability to deal with arbitrary geometries; it is mostly used in structural analysis, but also applicable to heat transfer, fluid flow, mass transport, and electromagnetic potential.[2]

2.4 Turbulence and its modelling

All flows encountered in engineering applications become unstable above a certain Reynolds number (Re), which is defined as:

$$Re = u \cdot \frac{l}{\nu}$$

Experiments on fluid systems have shown that at Reynolds numbers below the supercritical one, the flow is smooth and adjacent layers of fluid slide past each other in an orderly fashion. If applied boundary conditions do not change with time, the flow is steady and the regime so described is called *laminar flow*. This kind of flows is completely described by the mass conservation and the *Navier Stokes equations*; in simplest cases laminar flows can be solved analytically, while more complex flows can be tackled numerically with CFD techniques, e.g. the finite volume method, without

any additional approximations.

At values of Re above the critical one, a several complex series of events takes place, which could eventually lead to a radical change of the flow character. The motion becomes intrinsically unsteady even with constant imposed boundary conditions, and velocity and other flow properties vary in a random and chaotic way. This kind of regime described is called *turbulent flow*; most engineering flows of engineering significance are turbulent. [1]

Further properties which characterize turbulent flows are:

- They can be characterised in terms of mean values of flow properties (u , ν , p , etc.) and some statistical properties of their fluctuations (u' , ν' , p' , etc.) superimposed on them. These fluctuations arise from instabilities that grow until non-linear interactions cause them to break down into finer and finer whirls;
- They are three-dimensional. The time-averaged velocity may be a function of only two coordinates, but the instantaneous field fluctuates rapidly in all three spatial dimensions;
- They contain a great deal of vorticity. Indeed, vortex stretching is one of the principal mechanisms by which the intensity of turbulence is increased;
- Turbulence increases the rate at which conserved quantities are stirred. Stirring is a process in which parcels of fluid with differing concentrations of at least one of the conserved properties are brought into contact. The actual mixing is accomplished by diffusion. Nonetheless, this process is often called turbulent diffusion;
- Particles of fluid which are initially separated by a long distance can be brought together by the eddying motions in turbulent flows. As a consequence, heat, mass and momentum are very effectively exchanged. Such effective mixing gives rise to high values of diffusion coefficients for mass, momentum and heat;
- Turbulence brings fluids of differing momentum content into contact. The reduction of the velocity gradients due to the action of viscosity reduces the kinetic energy of the flow; in other words, mixing is a dissipative process. The lost energy is irreversibly converted into internal energy of the fluid;
- Turbulent flows fluctuate on a broad range of length and time scales. This property makes direct numerical simulation of turbulent flows very difficult.

A remarkable research effort has been dedicated for developing numerical methods for capturing turbulence and its effects; these methods can be grouped into the following six categories (according to Bardina et al., 1980), which can be also distinguished in sub-categories:

- Use of correlations as a function of the Reynolds number or the Nusselt number of heat transfer as a function of the Reynolds and Prandtl numbers. This method is very useful but is limited to simple types of flows. Its use does not require the use of a computer.
- Use of integral equations, which can be derived from the equations of motion by integrating over one or more coordinates. Usually this reduces the problem to one or more ordinary differential equations which can be easily solved.
- The **Turbulence models for Reynolds-averaged-Navier-Stokes (RANS) equations**: the attention is focused on the mean flow and the effects of turbulence on the mean flow properties. Prior to the application of numerical methods, the equations of motion are averaged over time (if the flow is statistically steady), over a coordinate in which the mean flow does not vary, or over an ensemble of realizations (an imagined set of flows in which all controllable factors

are kept fixed). In this way it is possible to obtain a set of partial differential equations, called the Reynolds-averaged-Navier-Stokes (or RANS) equations. Extra terms appear in the time-averaged (or Reynolds-averaged) flow equations due to the intersections between various turbulent fluctuations. These extra terms are modelled with classical turbulence models: among the best known ones are the *k-epsilon model* and the *Reynolds stress model*. The computing resources required for reasonably accurate flow computations are modest.

- Use of equations for the correlation of the velocity components at two spatial points or, more often, the Fourier transform of these equations. These methods are rarely used except for homogeneous turbulence.
- The **Large eddy simulation (LES)**. This is an intermediate form of turbulence calculations which tracks the behaviour of larger eddies. The method involves space filtering of the unsteady Navier-Stokes equations prior the computations, which passes the larger eddies and rejects the smaller eddies. The effects on the resolved flow (mean flow plus large eddies) due to the smallest, unresolved eddies are included by means of a so called sub-grid scale model. Unsteady flow equations must be solved, so demands on computing resources are large.
- The **Direct numerical simulation (DNS)**. These simulations compute the mean flow and all the turbulent velocity fluctuations. The unsteady Navier Stokes equations are solved on spatial grids that are sufficiently fine that they can solve the Kolomogorov length scales at which energy dissipation takes place and with time steps sufficiently small to resolve the period of fluctuations. These calculations are highly costly in terms of computing resources.

The last two methods hold lower approximations, therefore they turn out to be more exact; however the computation time for these methods is considerably higher than the others. [2]

RANS models

The vast majority of turbulent flow computations is carried out with procedures based on the Reynolds-averaged Navier Stokes (RANS) equations, since resolving all the details of the turbulence flow is unnecessary for most engineering purposes and time-averaged properties of the flow (e.g. mean velocities, mean pressures, mean stresses, etc.) turn out to be satisfying; in fact, common applications are normally concerned in knowing just a few quantitative properties of a turbulent flow, e.g. the average forces on a body and its distribution, the degree of mixing between two incoming streams of fluid, or the amount of a substance that has reacted. For this reason the RANS Turbulence models will be the only ones described in this thesis work.

In Reynolds-averaged approaches to turbulence, all of the unsteadiness is averaged out i.e. all unsteadiness is regarded as part of the turbulence.

On averaging, the non-linearity of the Navier-Stokes equations gives rise to terms that must be modelled.

In a statistically steady flow, every variable can be written as the sum of a time-averaged value and a fluctuation about that value:

$$\phi(x_i, t) = \bar{\phi}(x_i) + \phi'(x_i, t) \quad (2.37)$$

where:

$$\bar{\phi}(x_i) = \lim_{T \rightarrow \infty} \int_0^T \phi(x_i, t) dt \quad (2.38)$$

in which t is the time and T is the averaging interval, which must be large with regards to the typical time scale of the fluctuations.

If the flow is unsteady, time averaging cannot be used and it must be replaced by *ensemble averaging*, so instead of 2.38, it holds:

$$\bar{\phi}(x_i) = \lim_{N \rightarrow \infty} \frac{1}{N} \sum_{n=1}^N \phi(x_i, t) dt \quad (2.39)$$

where N is the number of members of the ensemble and must be large enough to eliminate the effects of the fluctuations.

This type of averaging can be applied to any type of flow, by applying it to the Navier-Stokes equations, the Reynolds-averaged-Navier-Stokes (RANS) equations are obtained.

From eqs. 2.38 and 2.39 it holds: $\overline{\phi'} = 0$, so averaging any linear term in the conservation equations simply gives the identical term for the averaged quantity.

From a quadratic nonlinear term, two terms are obtained, i.e. the product of the average and a covariance:

$$\overline{u_i \phi} = \overline{(\bar{u}_i + u'_i)(\bar{\phi} + \phi')} = \bar{u}_i \bar{\phi} + \overline{u'_i \phi'} \quad (2.40)$$

The last term of eq. 2.40 is null only if the two quantities are not correlated, but this is quite rare in turbulent flows; therefore the conservation equations generally contain terms such as $\rho \overline{u'_i u'_j}$, called the *Reynolds stresses*, and $\rho \overline{u'_i \phi'}$, known as the *turbulent scalar flux*, among others. These cannot be represented uniquely in terms of the mean quantities.

The averaged continuity and momentum equations for fluid dynamics, for incompressible flows without body forces, in tensor notation and Cartesian coordinates, are, respectively:

$$\frac{\partial(\rho \bar{u}_i)}{\partial x_i} = 0 \quad (2.41)$$

$$\frac{\partial(\rho \bar{u}_i)}{\partial t} + \frac{\partial}{\partial x_j} (\rho \bar{u}_i \cdot \bar{u}_j + \rho \overline{u'_i u'_j}) = -\frac{\partial \bar{p}}{\partial x_i} + \frac{\partial \bar{\tau}_{ij}}{\partial x_j} \quad (2.42)$$

where $\bar{\tau}_{ij}$ are the mean viscous stress tensor components, i.e.:

$$\bar{\tau}_{ij} = \mu \left(\frac{\partial \bar{u}_i}{\partial x_j} + \frac{\partial \bar{u}_j}{\partial x_i} \right)$$

The equation for the mean of a scalar quantity can be written as:

$$\frac{\partial(\rho \bar{\phi})}{\partial t} + \frac{\partial}{\partial x_j} (\rho \bar{u}_j \cdot \bar{\phi} + \rho \overline{u'_j \phi'}) = -\frac{\partial}{\partial x_j} \left(\Gamma \frac{\partial \bar{\phi}}{\partial x_j} \right) \quad (2.43)$$

The Reynolds-averaged-Navier-Stokes equations turn out to be not closed because of the presence of the Reynolds stresses and turbulent scalar flux; in fact, the number of variables is higher than the number of equations. Some approximations are therefore needed in order to solve these equations.

Usually the approximations involve the Reynolds stress tensor and turbulent scalar fluxes be written in terms of the mean quantities. The approximations introduced are called *turbulence models*, reported in table 2.1. For a turbulence model to be useful it must have a wide applicability, be accurate, simple and economical to run. The most common RANS turbulence models are classified on the basis of additional transport equations that need to be solved along with the RANS flow equations:

Among the Turbulence models shown in the table, the $k - \varepsilon$ and the *Mixing length* models are the most widely used and validated.

Table 2.1: RANS Turbulence models

<i>No. of extra transport equations</i>	<i>Turbulence model name</i>
Zero	Mixing length model
One	Spalart-Allmaras model
Two	$k - \varepsilon$ model $k - \omega$ model Algebraic stress model
Seven	Reynolds stress model

2.5 Converge CFD software

The program adopted in this thesis project is CONVERGE CDF software. CONVERGE was developed by engine simulation experts and can be used for both engine and non-engine simulations. Unlike many CFD programs, this software automatically generates a perfectly orthogonal, structured grid at runtime based on user-defined grid control parameters. This grid generation method completely eliminates the need to manually generate a grid.

CONVERGE allows the user to simulate three-dimensional, incompressible or compressible, transient or steady-state, chemically reacting flows in complex geometries with stationary or moving surfaces. The software can perform calculations with any number of species and chemical reactions, as well as transient liquid sprays and laminar or turbulent flows.



Figure 2.2: CONVERGE CFD software logo

Traditionally, boundary-fitted grids morph the vertices and cells in the interior of the domain to conform to the shape of the geometry. There are two significant disadvantages of using a traditional boundary fitted grid. First, whether structured or unstructured, fitting a grid to a complex geometry prevents the use of simple orthogonal grids. This in turn eliminates the benefits of numerical accuracy and computational efficiency associated with orthogonal grids. Second, generating a traditional boundary-fitted grid for a complex moving geometry can be time consuming and difficult. Often the grid generation difficulties and significant time requirements are a roadblock to simulating complex moving geometries such as an internal combustion engine.

CONVERGE uses a different strategy: a boundary-fitted approach eliminates the need for the computational grid to coincide with the geometry of interest. This method has two significant advantages. First, the type of grid used is chosen for computational efficiency instead of geometry. This allows the use of simple orthogonal grids, which simplifies the numerics of the solver. Second, the grid generation complexity and the time required are greatly reduced, as the complex geometry only needs to be mapped onto the underlying orthogonal grid. You are required to provide only a file containing the surface geometry represented as a closed triangulated surface. This file is easily written in Stereo Lithography (STL) format in most CAD packages. Given a proper STL file for the geometry of interest, it will take mere minutes to

prepare a surface for even complex geometries. Note that this user time is not spent creating a grid, as CONVERGE performs the grid generation internally at runtime. Your time is spent uniquely identifying various portions of the surface so that you can specify mesh motion and boundary conditions.

At runtime, CONVERGE uses the given triangulated surface to cut the cells that are intersected by the surface. There are many benefits of generating the grid internally by the code at runtime rather than requiring you to generate the grid as an input to the code.

Runtime grid generation allows the grid to be changed during the simulation. Possible changes include scaling the cell size of the entire domain, locally refining or coarsening during the simulation, and adaptively refining the mesh. Another major advantage of runtime grid generation is the ability of CONVERGE to regenerate the grid near moving boundaries during the simulation without any input from you. This means that setting up a case with a moving boundary is no more difficult than setting up a stationary case.

In addition to its novel approaches to grid generation and boundary treatment, CONVERGE includes state-of-the-art numerical techniques and models for physical processes including turbulence, spray, combustion, conjugate heat transfer, and cavitation.

With these models, CONVERGE can simulate a wide variety of flow problems. The models in CONVERGE have been extensively validated for internal combustion engine cases.

2.5.1 Grid control

CONVERGE includes several tools for controlling the grid size before and during a simulation:

- *Grid scaling*: coarsens or refines the base grid size;
- *Fixed embedding*: refines the grid at specified locations and times;
- *Adaptive Mesh Refinement (AMR)*: automatically changes the grid based on fluctuating and moving conditions.

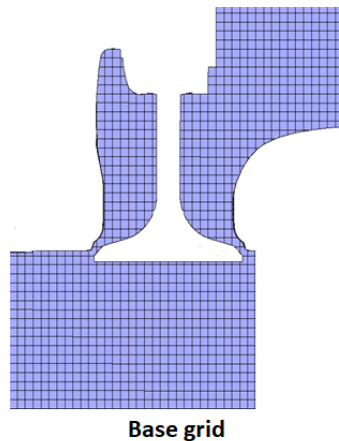


Figure 2.3: Example of *Base grid*

Grid Scaling

Grid scaling refers to changing the base grid size at specified times during a simulation. Grid scaling can greatly reduce runtime by coarsening the grid during non-critical simulation times and can help capture critical flow phenomena by refining

the grid at other times. For example, for an in-cylinder diesel engine simulation that includes spray and combustion modelling, the grid needs a higher resolution to ensure accurate results during spray and combustion but lower grid resolution may be sufficient during compression. Thus it is possible to direct CONVERGE to coarsen the grid during compression and refine the grid when spray begins for example, once specified the original base grid size via dx_base , dy_base , and dz_base . CONVERGE uses the $grid_scale$ parameter to change the base grid size according to

$$scalegrid = \frac{dx_base}{2^{grid_scale}}$$

where $grid_scale$ is the scaling factor and scaled grid is the new base grid size. A $grid_scale$ value of 0 will leave the base cells unchanged, a negative value will coarsen the base grid, and a positive value will refine the base grid. CONVERGE also scales dy_base and dz_base according to the previous equation.

Fixed embedding

Fixed embedding, as introduced, refines the grid at specific locations in the domain where a finer resolution is critical to the accuracy of the solution, by just specifying an embedding scale that indicates how CONVERGE will refine the grid in that location. It allows the rest of the grid to remain coarse to minimize simulation time. It is important to specify an embedding scale that indicates how CONVERGE will refine the grid in that location. The $embed_scale$ parameter scales the base grid sizes (dx_base , dy_base , and dz_base) according to:

$$dx_embed = \frac{dx_base}{2^{embed_scale}}$$

Adaptive mesh refinement

Adaptive Mesh Refinement (AMR), as said, automatically refines the grid based on fluctuating and moving conditions such as temperature or velocity. This option is useful for using a highly refined grid to accurately simulate complex phenomena such as flame propagation or high-velocity flow without unnecessarily slowing the simulation with a globally refined grid.

Ideally, a good AMR algorithm will add higher grid resolution (embedding) where the flow field is most under-resolved or where the sub-grid field is the largest (i.e., where the curvature [gradient] of a specified field variable is the highest). The AMR method in CONVERGE estimates the magnitude of the sub-grid field to determine where CONVERGE will add embedding. AMR can be activated for several fields, such as velocity, number of parcels per cell, temperature, void fraction, species, passives, or boundary, specifying different embedding scale and different sub-grid criterion for each condition, as well as the time when the AMR will start and when it will end for each field.

Ideally, a good AMR algorithm will add higher grid resolution (embedding) where the flow field is most under-resolved or where the sub-grid field is the largest (i.e., where the curvature [gradient] of a specified field variable is the highest). The AMR method in CONVERGE estimates the magnitude of the sub-grid field to determine where CONVERGE will add embedding.

For a scalar, the sub-grid field is defined as the difference between the actual field and the resolved field or

$$\phi' = \phi - \bar{\phi} \tag{2.44}$$

where ϕ is the actual scalar field, $\bar{\phi}$ is the resolved scalar field, and ϕ' is the sub-grid scalar field. The sub-grid for any scalar can be expressed as an infinite series (Bedford

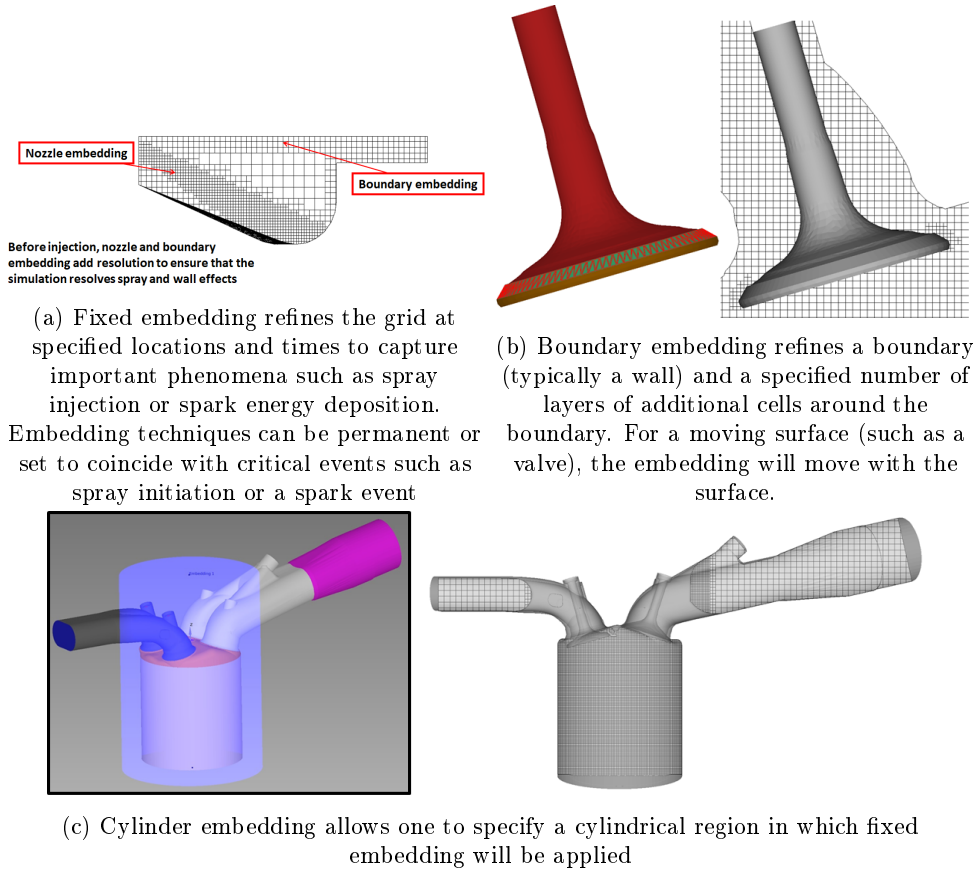


Figure 2.4: Examples of *Fixed Embedding*

and Yeo, 1993, and Pomraning, 2000) given by:

$$\phi' = -\alpha_{[k]} \frac{\partial^2 \bar{\phi}}{\partial x_k \partial x_k} + \frac{1}{2!} \alpha_{[k]} \alpha_{[l]} \frac{\partial^4 \bar{\phi}}{\partial x_k \partial x_k \partial x_l \partial x_l} - \frac{1}{3!} \alpha_{[k]} \alpha_{[l]} \alpha_{[m]} \frac{\partial^6 \bar{\phi}}{\partial x_k \partial x_k \partial x_l \partial x_l \partial x_m \partial x_m} + \dots \quad (2.45)$$

where $\alpha_{[k]}$ is $dx_k^2/24$ for a rectangular cell and the brackets $[\]$ indicate no summation. Since it is not possible to evaluate the entire series, only the first term (the second-order term) in the series is used to approximate the scale of the sub-grid. A cell is embedded if the absolute value of the sub-grid field is above a user-specified value. Conversely, a cell is released (i.e., the embedding is removed) if the absolute value of the sub-grid is below 1/5th of the user-specified value.

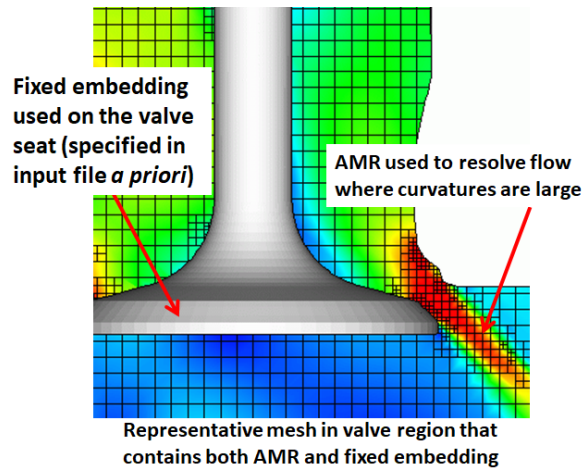
The the maximum overall number of cells can be specified and if the number of cells in the grid reaches the maximum number, CONVERGE uses the AMR routine to determine where to put the embedding in a manner that best resolves the flow field and meets the maximum number of cells. To make optimal use of all of the cells when the cell limit is reached, CONVERGE will adjust the user-specified sub-grid value criteria as needed. That is, if there are too many cells, CONVERGE will increase the value of the user-specified sub-grid criteria.

The minimum number of cells can be also specified and if the pre-AMR cell count is less than the specified value, CONVERGE will automatically add embedding, based on the sub-grid calculations. That is, CONVERGE will lower the user-specified sub-grid value until the grid consists of the minimum number of cells.

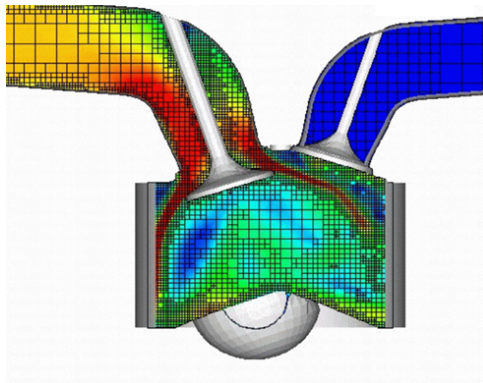
AMR can be enabled for any or as many of the following fields as you wish: velocity, number of parcels per cell, temperature, void fraction, species, passives, or boundary (y^+).

In some simulations, the flow conditions may be such that sub-grid scale quantities

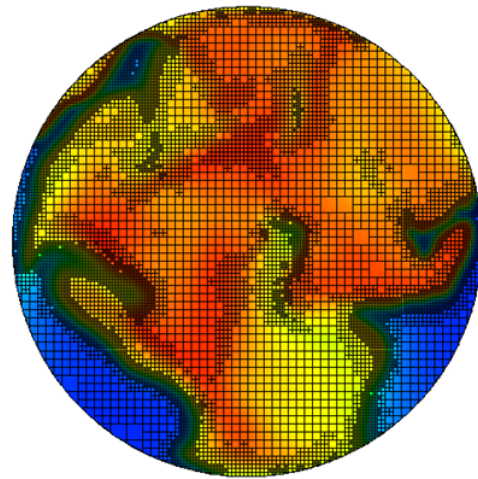
near solid walls trigger AMR. The flow features near the wall, however, may not be of interest. When CONVERGE refines the grid near a wall, the total cell count will increase, which may prevent additional refinement near relevant flow features. Also, excessive refinement near the wall may cause the cell count to exceed maximum number of cells, preventing further refinement. Another problem with AMR refinement near walls is that, if the y^+ value of a cell adjacent to a wall falls outside of the range for the chosen model, the results might be physically unrealistic. To avoid these problems, CONVERGE includes an option for y^+ AMR restriction, i.e. a target value for y^+ must be specified (on a boundary-by-boundary basis), and CONVERGE will remove refinement from AMR in an effort to maintain the desired target value. [3]



(a) AMR



(b) Example 1: AMR capturing flapping jet found in intake flow simulation



(c) Example 2: AMR capturing flame front for spark-ignited engine simulation using detailed chemistry

Figure 2.5: *Adaptive Mesh Refinement (AMR)*

NG-Engine: experimental data

3.1 Introduction

As previously introduced, this thesis project is aimed at the development of an accurate and efficient CFD model of a 1.4 liter-natural gas-internal combustion engine in CONVERGE, by means of a thorough calibration and validation against experimental data available at *Politecnico di Torino*. The project is focused on the combustion simulation by using the SAGE-detailed chemistry model, coupled to a suitable reaction mechanism among some found in literature.

In this chapter the engine studied is described, as well as its related experimental for the validation of the model developed.

3.2 Engine main characteristic

The engine examined is a *Fiat FIRE 1.4 16V Turbo CNG*, assembled by "Centro Ricerche FIAT" (CFR) in Orbassano (TO), and installed in the Energy department Lab. in Politecnico di Torino. The engine is optimized for methane and natural gas combustion.

Table 3.1 reports the engine technical data, while Figure 3.1 shows the engine and the test bench under construction.

Table 3.1: Engine main data

Cycle	Otto (4 strokes)
Fuel supply	Matatron METAFUEL 6AO.PNT injector
Valves	16V, two camshaft in head
Intake valve opening (IVO)	TDC -3°
Intake valve closing (IVC)	BDC $+37^\circ$
Exhaust valve opening (EVO)	BDC $+37^\circ$
Exhaust valve closing (EVC)	TDC -3°
Cylinders	4 (inline)
Bore	72 mm
Stroke	84 mm
Displacement	1368 cm ³
Connecting rod length	129 mm
Compression ratio (CR)	9.8



Figure 3.1: Engine and test bench under construction

3.2.1 Engine fuel

Internal combustion engines are the most widespread technology for automotive applications but, at the same time, one of the main sources of urban environment pollution. Hence, worldwide emission standards are getting stricter and stricter and low emission engines with alternative fuels are under development. Worthwhile alternatives to petroleum products engines, e.g. gasoline and diesel fuels, are natural gas, bio-diesel, bio-ethanol and methanol engines. The engine considered in this thesis project is a natural gas engine, whose composition is mainly constituted by methane. The fuel composition is:

- $\text{CH}_4 > 98\%$;
- $\text{C}_2\text{H}_6 < 1\%$;
- $\text{C}_4\text{H}_{10} < 0.6\%$;
- $\text{CO}_2 < 1\%$.

This kind of fuel has a low carbon level, thus it turns out to be one of the less polluting fuels in terms of carbon monoxide, carbon dioxide and hydrocarbon. Moreover, methane has high anti-knock properties, which allows to deal with higher compression ratios for spark-ignition engines and therefore higher thermal efficiencies. Nevertheless, methane has a rather low burning rate, which causes remarkable cycle to cycle variations and lower thermal efficiencies for piston engines.

3.2.2 Intake system

The Fiat FIRE engine intake system is composed by:

Indirect air mass flow rate meter (*Speed Density-Lambda type*): sensor measuring the absolute pressure and temperature in the intake manifold of each cylinder. The air mass flow rate is then computed indirectly from these two gathered data;

Wired controlled butterfly valve: valve whose role is to control the engine load. It is shown in figure 3.2a and 3.2b;

Idle air control actuator: actuator which ensures sufficient air so that the engine can win the friction work and can still work when the throttle is closed;

Centrifugal radial compressor: aimed at forcing extra air into the combustion chamber to increase the engine's efficiency and power output, the compressor used for the turbo-charging is manufactured by *IHI Corporation*;

Intercooler air-water: device whose role is to cool the hot air coming from the compressor, ensuring that more oxygen reaches the engine. It is shown in figure 3.2d.

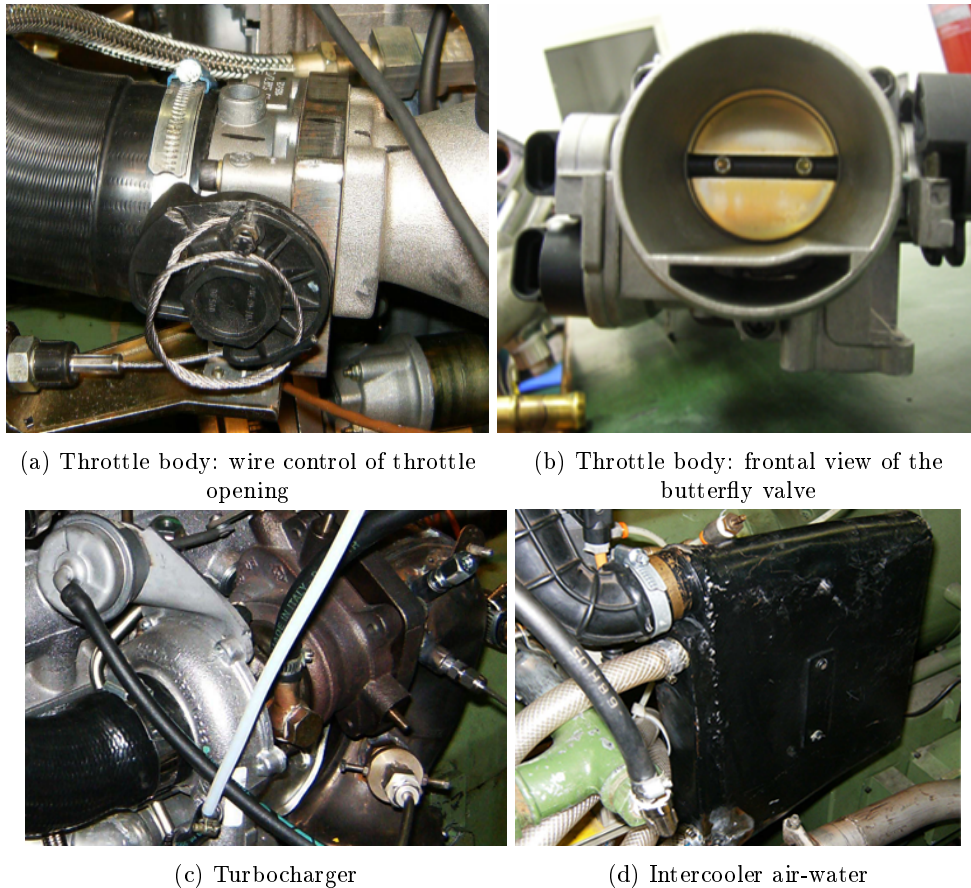


Figure 3.2: Intake system

3.2.3 Fuel supply system

The Fiat FIRE engine fuel supply system is made by three main components:

Tartarini Meta M pressure regulator: Self-regulated valve, calibrated to give a pressure at the outlet of about 8.9 bar, while can be accept as inlet pressure between 15 and 200 bar. It is equipped with the following sensors: Piezo-resistive high pressure sensor *Keller Pa 22 M*, Piezo-resistive low pressure sensor *Kavlico P4000*, Type K thermocouple. It is shown in Figure ??;

Injectors rail: connect the injectors dedicated for each cylinder. The main difference with respect to the gasoline injection system is the bigger nozzle diameter and the higher pressure (8÷10 bar). It is shown in Figure 3.4;

Gas electro-injectors per cylinder.

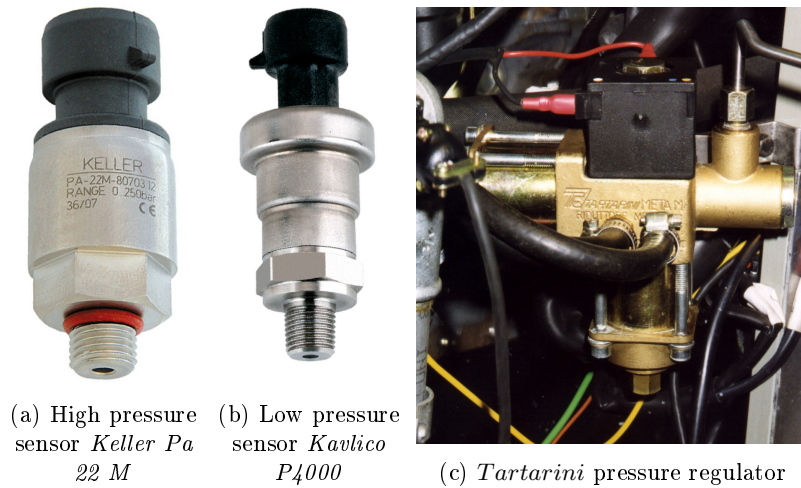


Figure 3.3: *Tartarini* Meta M pressure regulator

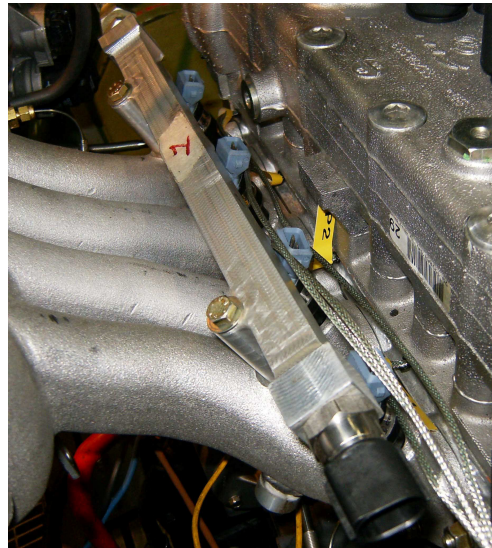


Figure 3.4: Gas feeding rail

3.2.4 Measuring system

The main physical quantities (e.g. temperature, pressure, mass flow rate, gas components mass fractions) are measured by an accurate measuring system involving lots of sensors and transducers. The measurements done can be grouped into four main categories:

- On engine measurements;
- Intake system measurements;
- Exhaust system measurements;
- On brake measurements.

On engine measurements

This category collects the following data:

- Pressure and temperature in inlet manifold (**HF**: p_{AMAP} ; **LF**: p_{AMAP_LF} , T_{AMAP});

- Pressure in the chamber of each cylinder ($p_{_Cyl1}$, $p_{_Cyl2}$, $p_{_Cyl3}$, $p_{_Cyl4}$);
- Pressure in the four intake runners ($p_{_Arun1}$, $p_{_Arun2}$, $p_{_Arun3}$, $p_{_Arun4}$) and in the exhaust ones ($p_{_Erun1}$, $p_{_Erun2}$, $p_{_Erun3}$, $p_{_Erun4}$);
- Pressure wave in the manifold ($p_{_Arun22}$) by an additional pressure sensor at the inlet runner of cylinder 2;
- Temperature in the inlet ($T_{_Arun1}$, $T_{_Arun2}$, $T_{_Arun3}$, $T_{_Arun4}$) and outlet runners ($T_{_Erun1}$, $T_{_Erun2}$, $T_{_Erun3}$, $T_{_Erun4}$);
- Pressure and temperature in the compressor inlet and outlet (inlet: $p_{_AbTC}$, $T_{_AHyg}$; outlet: $p_{_AaTC}$, $T_{_AaTC}$);
- Pressure and temperature in the turbine inlet and outlet (inlet: $p_{_EbTrb}$, $T_{_EbTrb}$; outlet: $p_{_EaTrb}$, $T_{_EaTrb}$);
- Water and temperature at the inlet and outlet of engine cooling system ($T_{_H2Oin}$, $T_{_H2Oout}$);
- Pressure and temperature of lubrication oil ($p_{_oil}$, $T_{_oil}$).

The instruments used for gathering the pressure data are:

Piezo-resistive transducer 4073 A10 made by Kistler to measure the pressure in intake manifold, shown in figure 3.5a;

Miniaturized piezoresistive transducer 4005BASF by Kistler to measure the pressure in intake and exhaust runners, shown in figure 3.5b;

Kistler piezo-electric transducer 6052C to measure the pressure in the chamber. It is important to underline the fact that it measures a quantity whose variability is particularly high since it subjected to very rapid phenomena (e.g. combustion) and also to high temperature; therefore, this traducer has been chosen for its higher performance (high frequency band, and high working temperature).

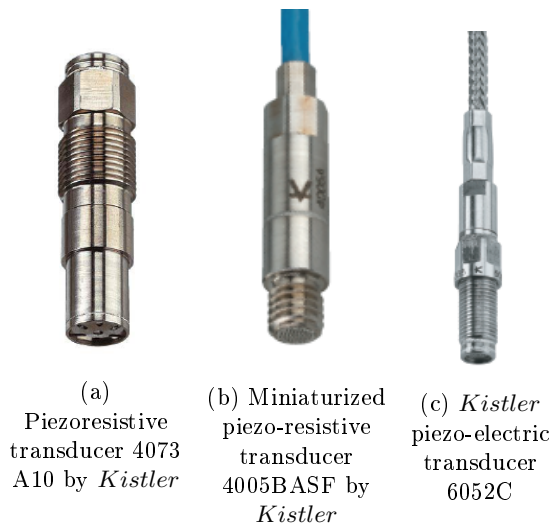


Figure 3.5: Pressure sensors

Intake system measurements

This category collects a set of data which are particularly crucial for the mixture control, i.e.

- Environment pressure and temperature (p_{env} , T_{env}), measured by the transducer "Sensy flow P" by *Hartmann and Brown*;
- Air mass flow rate (M_A);
- Pressure and temperature in the setting chamber (p_{Ainlet} , T_{Ainlet});
- Fuel mass flow rate, consumption and temperature (M_F , M_{FFreq} , T_F);
- Pressure and temperature after the inter-cooler (p_{AaIC} , T_{AaIC});
- Water temperature at the inter-cultural inlet and outlet (T_{H2ObIC} , T_{H2OaIC}).



Figure 3.6: Intake pressure transducers location

Exhaust system measurements

To monitor the exhaust gas the following data have been gathered:

- Air to fuel ratio (A/F) ($UEGO_L$, $UEGO_R$);
- Pollutions (E_{THC} , E_{CH4} , E_{HCO} , E_{LCO} , E_{CO2} , E_{O2} , E_{CO2EGR} , E_{NOx})

by using 2 lambda-sensors made by *NGK*, also known as Universal Exhaust Gas Oxygen (UEGO).

On brake measurements

The data collected in this category are the following:

- Engine torque and speed ($Torque$, $Speed$);
- High accuracy speed ($Speedenc$)

by using a dynamo-meter FE 260-S by *Borghi and Saveri* (fig. 3.7) and a high accuracy incremental encoder 59 CA TX made by *Elcis*.

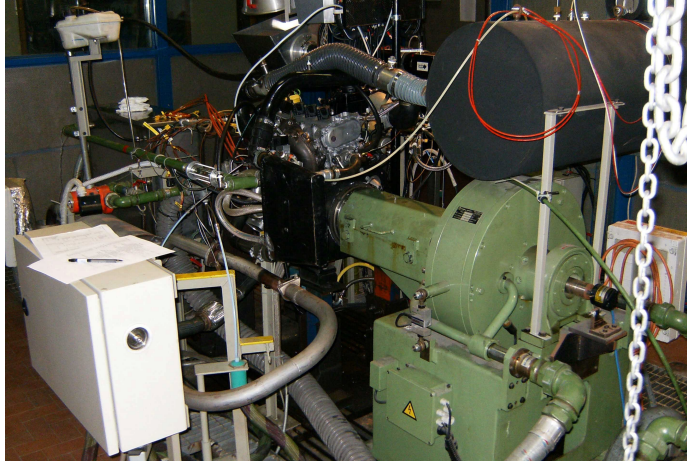


Figure 3.7: Dynamo-meter FE 260-S by *Borghi and Saveri*

3.3 Experimental parameters for model validation

All the information gathered through the measurement process, i.e. all the experimental data of the engine at different engine operating points, are stored in files with extension ".TSMS" (Technical Data Management Streaming); to use them one needs an Add-In Tool for Microsoft Excel.

Each file represents a specific engine working condition, i.e. revolutions per minute and load; for example the document named 2000_360_04.tdms stands for the operating point "2000 rpm x 3.6 bar".

Each file is composed by many sheets, which in turn contain all the data gathered for that engine point; therefore, each file is really heavy.

It is important to underline that in this thesis work the validation has been carried out by considering just cylinder 1, since the boundary conditions available are referred just to that.

The most important experimental data for the CFD model validation are:

- Pressure in cylinder 1, p_1 , which can be found in the in the TSMS file as `p_Cyl1` in the sheet `TAF`;
- Ensemble average pressure in cylinder 1, $p_{ens,1}$, which can be found in the in the TSMS file as `p_Cyl1_ens` in the sheet `p_Cyl1_ens`;
- Fuel mass flow rate, \dot{m}_f , which can be found in the in the TSMS file as `M_FFreq` in the sheet `####_###_##(root)`;
- Air-fuel ratio, α , which can be found in the in the TSMS file as `a_LCO` or `a_HCO` in the sheet `LFStatistic`;

Validation is carried out by considering two different problems, i.e. the *Fluid dynamic problem* and the *Thermal problem (Combustion)*.

Fluid dynamic problem

Described by the Navier-Stokes equations, the *Fluid dynamic problem* gives the velocity field \mathbf{v} and the pressure distribution p . The parameters that need to be considered for the model validation are:

$p_{SA,1}$, i.e. pressure at the spark advance in cylinder 1 [bar]. It is the value of the pressure at the spark advance angle θ_{SA} (the value of this crank angle can be

found, for each operating point, in the in the TSMS file as `Spark_Adv_deg` in the sheet `####_###_(root)`). So, one reads $p_{SA} = p_{ens,1}(\theta_{SA,1})$.

m_f , i.e. fuel mass in the cylinder [kg]. It is the mass of fuel in the chamber after the intake phase, whose experimental value can be determined by using the experimental data regarding the fuel mass flow rate \dot{m}_f :

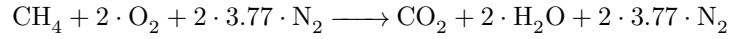
$$m_{f,exp} = \frac{\dot{m}_{f,exp}[\text{kg/h}]/3600}{n[\text{rpm}]/60} \cdot \frac{1}{2} \quad (3.1)$$

$m_{cyl,1}$, i.e. trapped mass in the chamber [kg]. It is the value of the total mass in the chamber after the intake phase. It can be computed through two different methods:

Without considering the combustion residues: the calculation involves the experimental data α and the fuel mass flow rate (computed as 3.1). The trapped mass is therefore:

$$m_{cyl,1,exp} = (1 + \alpha) \cdot m_{f,exp} \quad (3.2)$$

Considering the combustion residues: the calculation is based on the feasible hypothesis that the experimental combustion residues percentage can be assumed to be the same of the model one. First of all the model total mass, $m_{model}(\theta)$, and the mass of CO_2 , $m_{\text{CO}_2,model}(\theta)$, in the chamber must be considered. In CONVERGE, these data are respectively available in the output files `thermo_region1.out` and `species_mass_region1.out`. One must focus on the mass trapped in the cylinder, which is the one between intake valve closing crank angle (θ_{IVC}) and exhaust valve opening crank angle (θ_{EVO}), and the mass of CO_2 between intake valve closing crank angle (θ_{IVC}) and spark advance crank angle (θ_{SA}). The mass fraction of CO_2 in the exhausts (x_{CO_2}) can be computed by considering the following combustion balance equation:



where 3.77 is the mean molar ratio of nitrogen over oxygen in air. So

$$\mathcal{M}_{\text{CH}_4} = (\mathcal{M}_{\text{CO}_2} + 2 \cdot \mathcal{M}_{\text{H}_2\text{O}} + 2 \cdot 3.77 \mathcal{M}_{\text{N}_2})$$

$$m_{f,model}(1 + \alpha) = \frac{m_{f,model}}{\mathcal{M}_{\text{CH}_4}} (\mathcal{M}_{\text{CO}_2} + 2 \cdot \mathcal{M}_{\text{H}_2\text{O}} + 2 \cdot 3.77 \mathcal{M}_{\text{N}_2}) = m_{exh,model}$$

and so

$$\frac{m_{\text{CO}_2}}{m_{exh}} = x_{\text{CO}_2} = \frac{\mathcal{M}_{\text{CO}_2}}{\mathcal{M}_{\text{CH}_4}(1 + \alpha)} = \frac{44.01[\text{kg/mol}]}{16.04[\text{kg/mol}] \cdot (1 + \alpha)}$$

the mass fraction of combustion residues can be therefore obtained by:

$$x_{r,model} = \frac{m_{\text{CO}_2}}{x_{\text{CO}_2} \cdot m_{cyl,1,exp}} \quad (3.3)$$

where $m_{cyl,1,exp}$ is computed through eq. 3.2. With the assumption that $x_{r,model} = x_{r,exp} = x_r$, the trapped mass in the chamber with combustion residues turns out to be:

$$m_{cyl,1} = m_{f,exp}(1 + \alpha)(1 + x_r) \quad (3.4)$$

In this thesis project the latter method is the one considered.

Thermal problem (Combustion)

Combustion is composed by many chemical and physical phenomena and can be in principle described by a set of *Arrhenius* and diffusion equations, which provide the concentration of the several species involved and the heat release of every reaction.

The crank angle range on which the analysis must be concerned is that between the spark advance ($\theta_{SA,1}$) and the exhaust valve opening ($\theta_{EVO,1}$) in cylinder 1, i.e. the period in which the chamber can be considered a closed system.

The parameters that must be dealt with for the model validation are:

$p_{peak,1}$, i.e. peak pressure in cylinder 1 [bar].

$\theta_{peak,1}$, i.e. crank angle corresponding to the peak pressure in cylinder 1 [deg].

$HRR,1$, i.e. heat release rate in cylinder 1 [J/deg]. Since heat losses through the walls are always present, it is necessary to make a distinction between *Gross-HRR* and *Net-HRR*, which can be expressed as:

$$HRR_{Gross} = \frac{dQ_b}{d\theta} = \frac{k}{k-1}p \frac{dV}{d\theta} + \frac{1}{k+1}V \frac{dp}{d\theta} + \frac{dQ_l}{d\theta} \quad (3.5)$$

$$HRR_{Net} = \frac{dQ_b}{d\theta} - \frac{dQ_l}{d\theta} = \frac{k}{k-1}p \frac{dV}{d\theta} + \frac{1}{k+1}V \frac{dp}{d\theta} \quad (3.6)$$

where $\frac{dQ_b}{d\theta}$ is the heat supplied by the burning fuel, $\frac{dQ_l}{d\theta}$ is the heat losses through the walls, and k is the heat capacity ratio. In this thesis project the *Net-HRR* is the only one considered, because of the difficulty to determine the losses. For the computation of the heat capacity ratio k , the Michael F.J. Brunt methodology[9] has been adopted, which holds:

$$k = 1.338 - 6 \cdot 10^{-5} \cdot T + 6 \cdot 10^{-8} \cdot T^2 \quad (3.7)$$

$IHR,1$, i.e. integrated heat release in cylinder 1 [J]. It is obtained by integrating eq. 3.6 over the interval between (θ_{SA}) and (θ_{EVO}), giving:

$$IHR = Q_b - Q_l = \int_{\theta_{SA}}^{\theta_{EVO}} \left(\frac{dQ_b}{d\theta} - \frac{dQ_l}{d\theta} \right) d\theta \quad (3.8)$$

3.3.1 Data conditioning

As previously mentioned, natural gas engines are characterized by a remarkable cycle-to-cycle variability, choosing an engine cycle to be considered the "*most representative*" (i.e. the most probable pressure profile) happens to be essential. For this purpose, statistical analysis comes to the rescue and, in particular, the *ensemble average* concept. *Experimental ensemble average* is computed considering all the engine cycles measured, which must be in vast numbers. The result of this kind of averaging is a pressure profile which is an average of experimental pressure values at given crank angles and a *standard deviation vector*, which is an indicator of the goodness of the data. This information is stored in the TDMS files.

However *Experimental ensemble average* is not a "real" cycle, and since in this thesis project the number of simulation cycles computed for each case is not high, it is natural to perform the model validation by referring to the experimental cycle whose pressure profile is the closest to the experimental ensemble average one. This has to be compared to the simulation cycle whose pressure profile, again, is the closest to the experimental ensemble average.

The computation of these cycles has been performed through GNU-Octave scripts, which calculates the distances between each single measured pressure curve and the experimental ensemble average one; then it computes the mean values of the distances and takes the smallest value among them, which corresponds to the cycle

whose pressure profile is the closest to the experimental ensemble average one, i.e. the "*experimental reference cycle*".

Once this has been identified, all the experimental parameters such as $p_{SA,1}$, $p_{peak,1}$, $\theta_{peak,1}$, HRR_1 , and IHR_1 must be determined by considering it.

From now on, since all the parameters are related just to cylinder 1, the suffix "1" will no more be used.

3.4 Operating points considered

In this thesis work, the engine operating points on which the model validation has been carried out are:

Table 3.2: Engine operating points considered

Engine speed [rpm]	bmep [bar]	lambda [-]
2000	3.6	1
2000	7.9	1
3300	7.9	1

3.4.1 O.P. 2000 [rpm] x 3.6 [bar] x lambda=1

This is a low load operating point, characterized by:

- Spark advance = 26 deg;
- Air-to-Fuel ratio $\alpha = 17.121008$;
- Fuel mass flow rate $\dot{m}_f = 37$ [kg/s];
- Number of engine cycles measured = 100.

As it can be noticed in figures 3.8 and 3.9, this operating point is characterized by a remarkable cycle to cycle variability.

Referring to the experimental reference cycle, the peak pressure happens to be at around 734 crank angle degree, and its value is about 2.4 MPa.

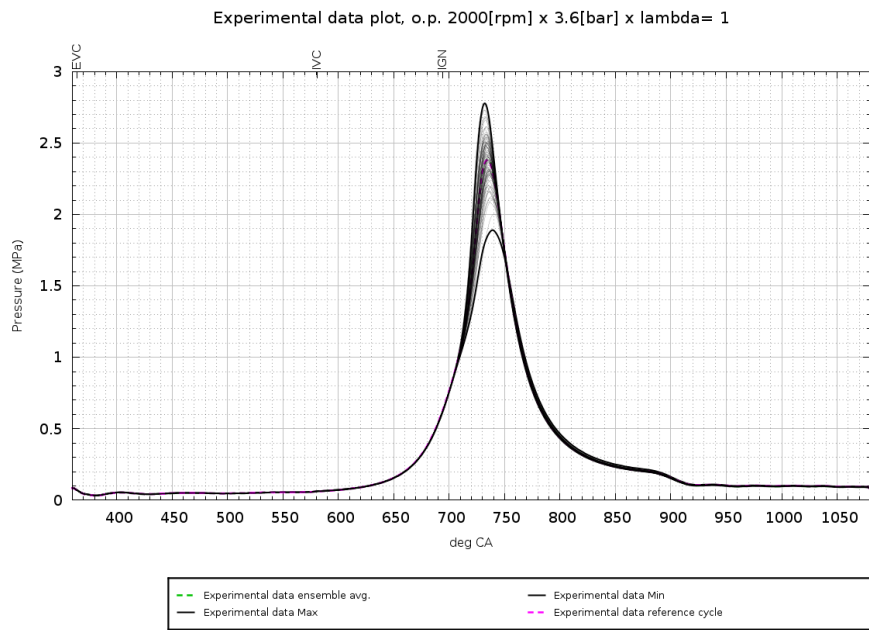


Figure 3.8: Experimental data plot: Pressure in cylinder 1, complete engine cycle

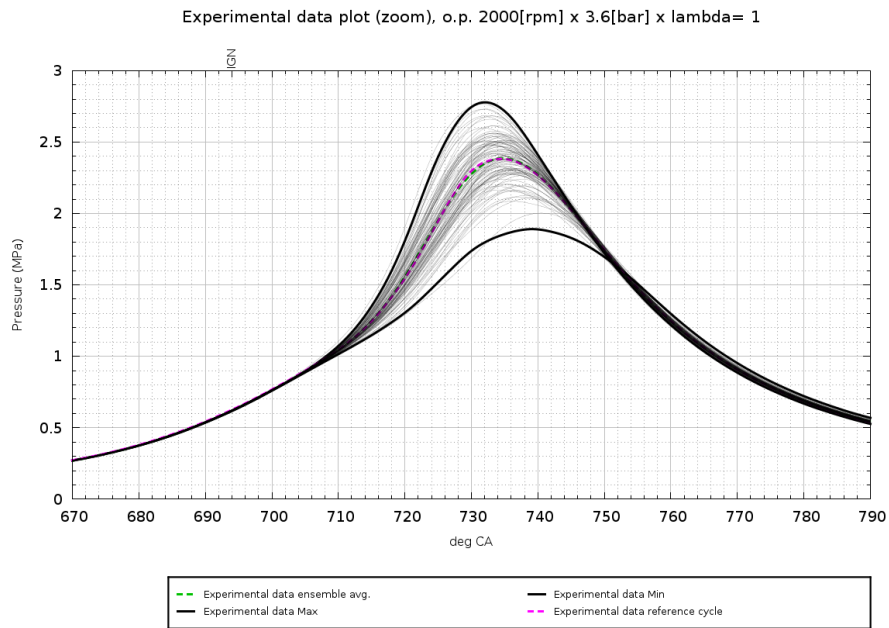


Figure 3.9: Experimental data plot: Pressure in cylinder 1, zoom around peak Pressure

3.4.2 O.P. 2000 [rpm] x 7.9 [bar] x lambda=1

This engine operating point is characterized by:

- Spark advance = 20 deg;
- Air-to-Fuel ratio $\alpha = 17.04550487$;

- Fuel mass flow rate $\dot{m}_f = 67$ [kg/s];
- Number of engine cycles measured = 100.

As it can be noticed in figures 3.10 and 3.11, this operating point is characterized by a remarkable cycle to cycle variability.

Referring to the experimental reference cycle, the peak pressure happens to be at around 735 crank angle degree, and its value is about 4.2 MPa.

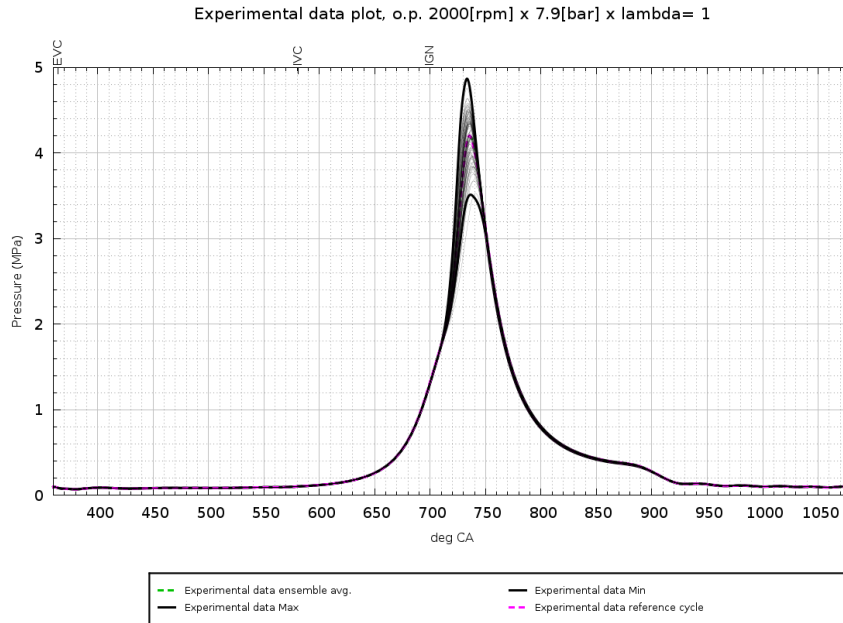


Figure 3.10: Experimental data plot: Pressure in cylinder 1, complete engine cycle

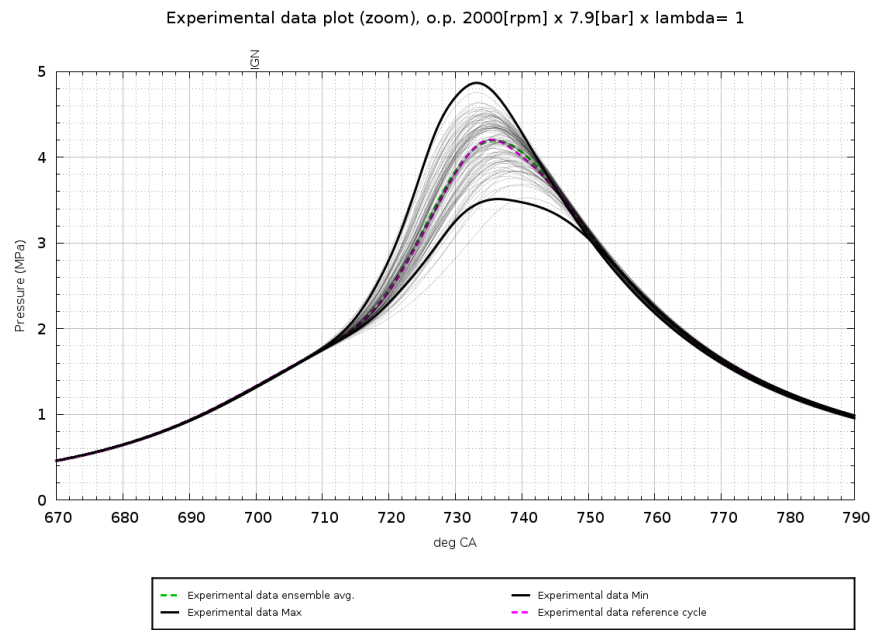


Figure 3.11: Experimental data plot: Pressure in cylinder 1, zoom around peak Pressure

3.4.3 O.P. 3300 [rpm] x 7.9 [bar] x lambda=1

This engine operating point is characterized by:

- Spark advance = 26 deg;
- Air-to-Fuel ratio $\alpha = 17.10327848$;
- Fuel mass flow rate $\dot{m}_f = 113$ [kg/s];
- Number of engine cycles measured = 100.

As it can be noticed in figures 3.12 and 3.13, this operating point is characterized by a remarkable cycle to cycle variability.

Referring to the experimental reference cycle, the peak pressure happens to be at around 733 crank angle degree, and its value is about 4.8 MPa.

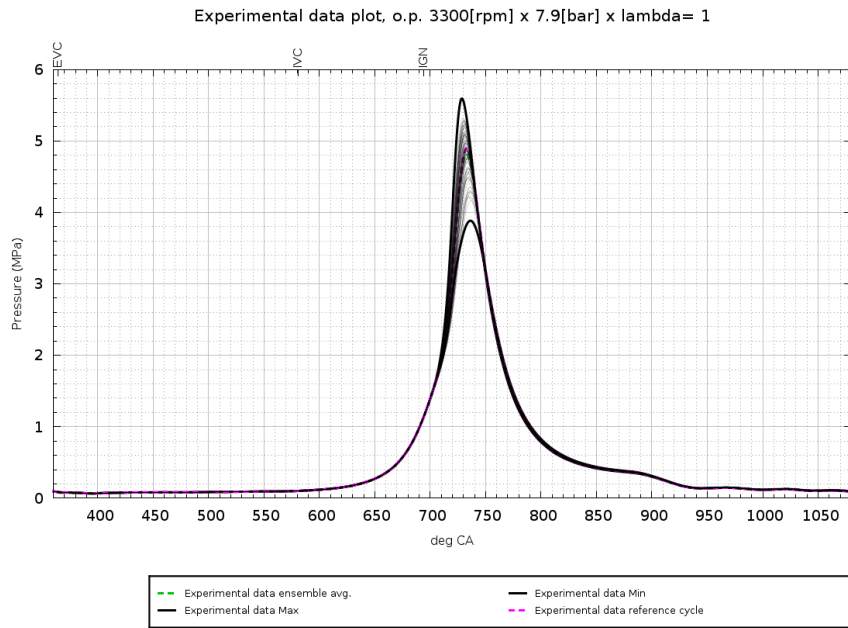


Figure 3.12: Experimental data plot: Pressure in cylinder 1, complete engine cycle

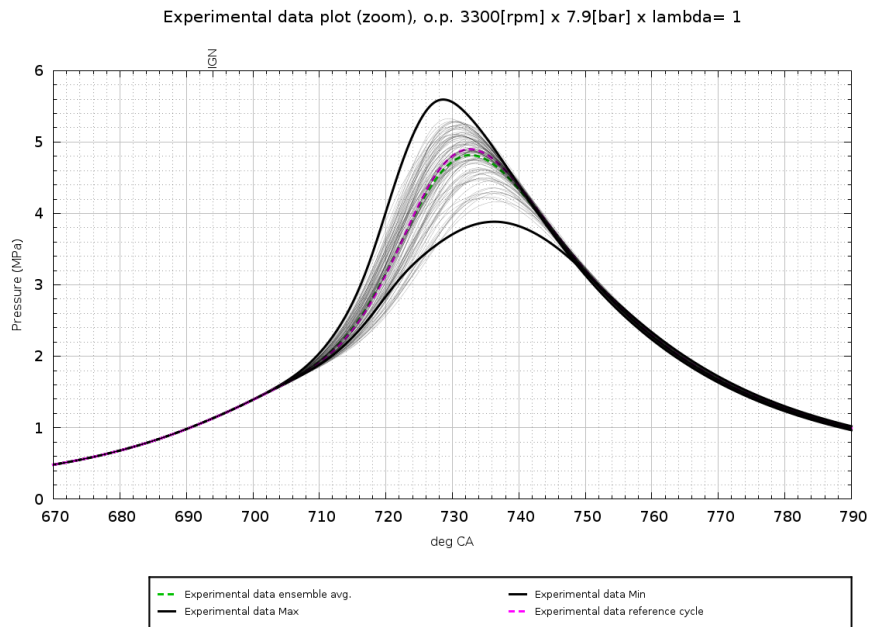
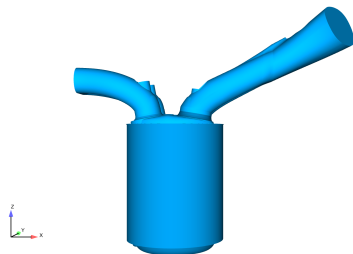


Figure 3.13: Experimental data plot: Pressure in cylinder 1, zoom around peak Pressure

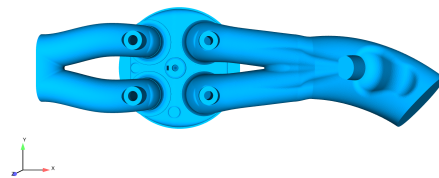
NG-Engine: CFD modelling

4.1 Geometry and regions

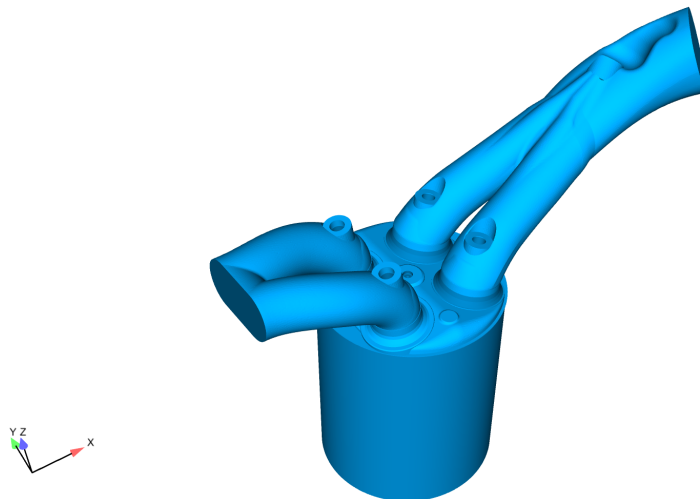
Fiat FIRE 1.4 16V Turbo CNG engine 3-D geometry has been provided by CRF as a CAD file, which defines the Control Volume of the model, V .



(a) Engine CAD geometry, view 1



(b) Engine CAD geometry, view 2



(c) Engine CAD geometry, view 3

Figure 4.1: Engine CAD geometry

This can be split into three regions, i.e.

Intake system, V_0 , or *Region 0*, it is the volume identified by the intake runner, the intake valve top and angle and the inflow port. In CONVERGE it is described by `region0`;

Cylinder, V_1 , or *Region 1*, it is the volume described by head, piston, liner, spark plug and intake valve bottom. In CONVERGE it is described by `region1`;

Exhaust system, V_2 , or *Region 2*, it is the volume bounded by the exhaust runner, exhaust valve top and angle and the outflow port. In CONVERGE it is described by `region2`.

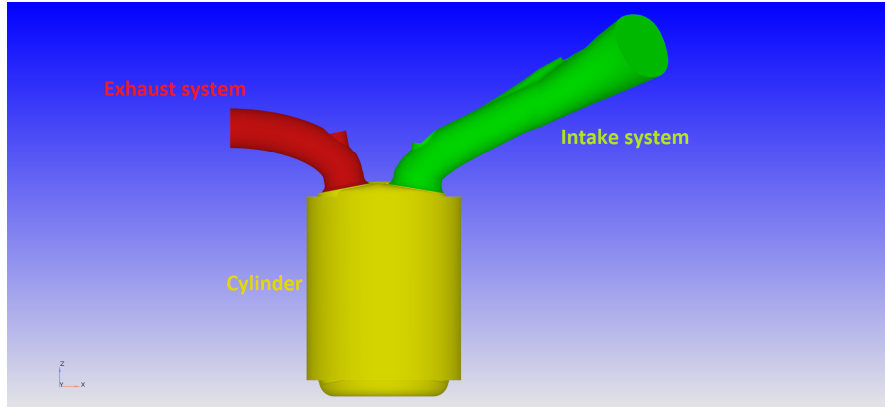


Figure 4.2: Regions

This subdivision naturally holds the definition of different boundaries, namely:

Boundary 0, S_0 , surface concerning the inlet runner and intake valve top and angle;

Boundary 1, S_1 , surface including the piston head, liner, cylinder head, spark plug and valves bottom;

Boundary 2, S_2 , surface defined by the outlet runner and the exhaust valve top and angle;

Boundary in, S_{in} , inflow port;

Boundary out, S_{out} , outflow port.

4.2 Fuel composition

In this thesis project two different fuels have been considered, which differ one another on the level of approximation of the real fuel composition:

Pure CH_4 , which is an admissible approximation, since in the real fuel composition the volume percentage of methane is more than 98%;

"Actual fuel composition", which is actually still an approximation, but closer to the real fuel composition with regards to the former one. It is composed by CH_4 , C_2H_6 , CO_2 .

Actual fuel composition

For the determination of this fuel composition, small approximations have been done. First of all, starting from the real fuel composition, the following fuel percentages have been assumed:

- $CH_4 > 98\% \rightarrow CH_4 = 98\%$;
- $C_2H_6 < 1\% \rightarrow C_2H_6 = 0.6\%$;
- $C_4H_{10} < 0.6\% \rightarrow C_4H_{10} = 0.4\%$;

- $\text{CO}_2 < 1\% \rightarrow \text{CO}_2 = 1\%$.

Then, since the species C_4H_{10} is not present among those included in the kinetic mechanisms considered in this thesis project, its mass fraction has been added to that of C_2H_6 .

4.3 Boundary and Initial conditions

Conservation, Momentum and Energy equations are, as previously discussed, partial differential equations (PDE); in order to be specified, a PDE's problem needs a set of boundary the initial conditions.

4.3.1 Boundary conditions

The boundary conditions of the problem, for different operating points, have been computed by a Matlab script, whose inputs are obviously the experimental data available at Politecnico di Torino.

Continuity equation

The boundary conditions regarding the continuity equation consist into the prescription of the fuel mass fractions at the inlet. For example, in case of *Pure CH₄* as fuel, they are given by:

$$Y_{CH_4} = \frac{1}{1 + \alpha} \quad (4.1)$$

$$Y_{O_2} = \frac{\alpha}{1 + \alpha} \cdot \frac{1}{1 + 3.77} \quad (4.2)$$

$$Y_{N_2} = \frac{\alpha}{1 + \alpha} \cdot \frac{3.77}{1 + 3.77} \quad (4.3)$$

while on the exhaust side combustion products are present, therefore compositions are not supposed to be prescribed.

Momentum equation

For what concerns the momentum equation, the boundary conditions are:

- Pressure at the inflow and the outflow ports, $p_{int}(\theta, S_{in})$ and $p_{exh}(\theta, S_{out})$, are prescribed (directly measured from the sensors in the runners);
- Velocity at the other boundaries, i.e. $\mathbf{v}(\theta, S_0)$, $\mathbf{v}(\theta, S_1)$, $\mathbf{v}(\theta, S_2)$, is prescribed by using the *Law of Wall* (described below), setting *no-slip condition*.

Energy equation

For the energy equation, it is assumed that the temperature is steady state on boundaries S_0 (spark wall temperature is set at 823.15 K), S_1 , S_2 , S_{in} , while for S_{out} , an adiabatic boundary condition is assumed, i.e.

$$\frac{\partial q}{\partial n} = 0$$

4.3.2 Initial conditions

Continuity equation

Initial conditions provide the initial gas composition in the three regions. For example, in case of *Pure CH₄* as fuel, for the intake manifold, the conditions are set by eqs. 4.1, 4.2, 4.3, while for the exhaust gas composition, one uses:

$$Y_{N_2} = \frac{1}{1 + \alpha} \cdot \frac{\mathcal{M}_{CO_2}}{\mathcal{M}_{CH_4}} \quad (4.4)$$

$$Y_{H_2O} = Y_{CO_2} \cdot \frac{\mathcal{M}_{H_2O}}{\mathcal{M}_{CO_2}} \cdot 2 \quad (4.5)$$

$$Y_{N_2} = \frac{\alpha}{1 + \alpha} \cdot \frac{3.77}{1 + 3.77} \quad (4.6)$$

$$Y_{O_2} = \frac{\alpha}{1 + \alpha} \cdot \frac{3.77}{1 + 3.77} - 2 \cdot Y_{CO_2} \frac{\mathcal{M}_{O_2}}{\mathcal{M}_{CO_2}} \quad (4.7)$$

Momentum equation

In the matter of momentum equation, initial conditions consist of setting the initial velocity field according to piston and valves position at the starting time, for example a null velocity field in the two runners and a linear decreasing field in the piston, in the case in which the BDC is in the exhaust phase.

Energy equation

Initial conditions for the energy equation include a constant temperature for each region, i.e. intake runner, exhaust runner and cylinder.

4.4 Turbulence modelling

In this thesis project, Reynolds averaged Navier-Stokes (RANS) equations have been implemented, with RNG (Renormalization Group) $k - \varepsilon$ as turbulence model.

As all the RANS models available in CONVERGE, RNG $k - \varepsilon$ is a two-equation model in which the flow variables (e.g., velocity) are decomposed into an ensemble mean and a fluctuating term as follows:

$$u_i = \bar{u}_i + u'_i \quad (4.8)$$

where u_i is the instantaneous velocity, \bar{u}_i the ensemble mean velocity term and u'_i the fluctuating velocity term.

Substituting eq. 4.8 into the continuity and momentum equations, it holds, respectively:

$$\frac{\partial \bar{\rho}}{\partial t} + \frac{\partial \bar{\rho} \tilde{u}_j}{\partial x_j} = 0 \quad (4.9)$$

$$\frac{\partial \bar{\rho} \tilde{u}_i}{\partial t} + \frac{\partial \bar{\rho} \tilde{u}_i \tilde{u}_j}{\partial x_j} = -\frac{\partial \bar{P}}{\partial x_i} + \frac{\partial}{\partial x_j} \left[\mu \left(\frac{\partial \tilde{u}_i}{\partial x_j} + \frac{\partial \tilde{u}_j}{\partial x_i} \right) - \frac{2}{3} \mu \frac{\partial \tilde{u}_k}{\partial x_k} \delta_{ij} \right] + \frac{\partial}{\partial x_j} (-\bar{\rho} \tilde{u}'_i \tilde{u}'_j) \quad (4.10)$$

where $\tilde{u}_i = \frac{\bar{\rho} u_i}{\bar{\rho}}$ is the *Favre* average.

The ensemble averaging of the equations introduces additional terms called the Reynolds stresses that represent the effects of turbulence. The Reynolds stress τ_{ij} is given by:

$$\tau_{ij} = -\bar{\rho} \tilde{u}'_i \tilde{u}'_j \quad (4.11)$$

The turbulence model simply models the Reynolds stress in order to obtain closure for Equation 4.10.

4.4.1 $k - \varepsilon$ models

RANS models use an effective turbulent viscosity to model the Reynolds stress term. Thus, additional turbulent diffusion (i.e., diffusive mixing) models the turbulent convective mixing.

RNG $k - \varepsilon$ model

The modelled Reynolds stress for the Standard k - ε and RNG models is given by:

$$\tau_{ij} = -\bar{\rho} u'_i \tilde{u}'_j = 2 \cdot \mu_t S_{ij} - \frac{2}{3} \delta_{ij} \left(\rho k + \mu_t \frac{\partial \tilde{u}_i}{\partial x_i} \right) \quad (4.12)$$

In eq. 4.12 k is the turbulent kinetic energy, defined as half of the trace of the stress tensor, i.e.

$$k = \frac{1}{2} u'_i \tilde{u}'_i \quad (4.13)$$

and μ_t is the turbulent viscosity, given by:

$$\mu_t = c_\mu \rho \frac{k^2}{\varepsilon} \quad (4.14)$$

where c_μ is a model constant which can be tuned for the specific flow, and ε is the dissipation of turbulent kinetic energy. S_{ij} is the mean strain rate tensor and is given by:

$$S_{ij} = \frac{1}{2} \left(\frac{\partial \tilde{u}_i}{\partial x_j} + \frac{\partial \tilde{u}_j}{\partial x_i} \right) \quad (4.15)$$

The Standard k - ε and RNG models use turbulent diffusion and turbulent conductivity terms to account for the presence of turbulence in mass transport (D_t) and energy transport (K_t). The turbulent diffusion and conductivity terms are:

$$D_t = \frac{1}{Sc_t} \mu_t \quad (4.16)$$

and

$$K_t = \frac{1}{Pr_t} \mu_t c_p \quad (4.17)$$

where Sc_t is the turbulent Schmidt number, Pr_t is the turbulent Prandtl number, D_t is the turbulent diffusion, and K_t is the turbulent conductivity.

The standard $k - \varepsilon$ and RNG $k - \varepsilon$ models require additional transport equations to obtain the turbulent viscosity given by eq. 4.14. One equation is needed for the turbulent kinetic energy k and one for the dissipation of turbulent kinetic energy ε . The turbulent kinetic energy transport equation is given by:

$$\frac{\partial \rho k}{\partial t} + \frac{\partial \rho u_i k}{\partial x_i} = \tau_{ij} \frac{\partial u_i}{\partial x_j} + \frac{\partial}{\partial x_j} \frac{\mu}{Pr_k} \frac{\partial k}{\partial x_j} - \rho \varepsilon + \frac{c_s}{1.5} S_s \quad (4.18)$$

where the factor of 1.5 is an empirical constant. The transport equation for the dissipation of turbulent kinetic energy is given by:

$$\frac{\partial \rho \varepsilon}{\partial t} + \frac{\partial \rho u_i \varepsilon}{\partial x_i} = \frac{\partial}{\partial x_j} \frac{\mu}{Pr_\varepsilon} \frac{\partial \varepsilon}{\partial x_j} - \rho \varepsilon + c_{\varepsilon 3} \rho \varepsilon \frac{\partial u_i}{\partial x_i} + \left(c_{\varepsilon 3} \frac{\partial u_i}{\partial x_j} \tau_{ij} - c_{\varepsilon 2} \rho \varepsilon + c_s S_s \right) \frac{\varepsilon}{k} + S + \rho R \quad (4.19)$$

in which S is the user-supplied source term and S_s is the source term that represents the interactions with discrete phase. The $c_{\varepsilon i}$ terms are model constants that account for compression and expansion. For the RNG $k - \varepsilon$ model R is given by:

$$R = \frac{C_\mu \eta^3 (1 - \eta/\eta_0) \varepsilon^2}{(1 + \beta \eta^3) k}$$

where $\eta = \frac{k}{\varepsilon} |S_{ij}|$. [3]

4.4.2 Law of Wall

The *Law of Wall* is the forceful name for finding that, with certain assumptions, the mean velocity u in constant-property turbulent flow near to a smooth impermeable solid surface of negligible curvature can be correlated in terms of the shear stress at the surface τ_w , the distance from the surface y , and the fluid properties density ρ and molecular viscosity μ . Quantities such as the layer thickness δ or the duct diameter, and the edge velocity u_e or other overall mean velocity scale are supposed not to matter; effects of the upstream history of the flow, and even of local stream-wise (x -wise) pressure gradient and x -wise or y -wise shear stress gradients are also neglected. [10]

The Reynolds averaged Navier-Stokes equation states that:

$$\frac{\partial}{\partial t} \rho \mathbf{v} + \nabla \cdot \rho \overline{\mathbf{v} \mathbf{v}} = -\nabla \bar{p} + \nabla \cdot \bar{\boldsymbol{\tau}} + \mathbf{f}_b \quad (4.20)$$

The stress tensor $\bar{\boldsymbol{\tau}}$ can be split into:

$$\bar{\boldsymbol{\tau}} = \mu \nabla \bar{\mathbf{v}} - \overline{\rho \mathbf{v}' \mathbf{v}'} \quad (4.21)$$

where the first term in the second hand side the equation 4.21 is the laminar term of the stress tensor $\bar{\boldsymbol{\tau}}$ while the second term in the second hand side of the same equation is the turbulent one.

The region around the solid surface can be split in different layers according to according to the prevalence of one of the aforementioned terms, namely:

Inner layer, or *Boundary layer*, the area in which the laminar part of the tensor prevails on the turbulent one;

Outer layer, the area in which the turbulent component of the tensor prevails on the laminar one.

So, as previously introduced and as Prandtl stated after his studies in 1930, the average velocity of a turbulent flow is:

$$u = f(\nu, \rho, \|\tau_w\|, y) \quad (4.22)$$

The following dimensionless numbers can be thus defined:

Shear velocity $u_\tau = \sqrt{\frac{\|\tau_w\|}{\rho}}$

Dimensionless velocity $u^+ = \frac{\|\mathbf{v} - \mathbf{v}_w\|}{u_\tau}$

Normalized wall distance $y^+ = \frac{d_\perp u_\tau}{\nu}$

where $\|\tau_w\|$ is the magnitude of the relative velocity parallel to the wall and d_\perp is the normal stress distance from the wall. Therefore, eq. 4.22 can be rewritten as:

$$u^+ = f(y^+) \quad (4.23)$$

which is the so called *Law of Wall*.

The *Boundary layer* can be in turn subdivided in three further sub-layers according to parameter y^+ :

Viscous sub-layer: range in which $0 < y^+ \leq 5$. The variation between y^+ and u^+ is approximately 1:1, so the speed profile can be described as $u^+ = y^+$;

Buffer sub-layer: range in which $5 < y^+ \leq 30$. It is a region whose characteristics are in-between the other two layers;

Inertial sub-layer: range in which $30 < y^+ \leq 200$. Turbulence has a small influence in this range. In this area, the *Law of Wall* has, according to Von Karman and Millikan, a logarithmic trend, i.e. $u^+ = \frac{1}{k} \ln(y^+) + B$; in the correlation $k = 0.41$ and $B = 5.25$.

Law of wall application in CFD code

A turbulent fluid approaching the wall is subjected to a quick relative speed reduction, until it goes to zero. This means that there is a high gradient, which makes the discretization process laborious; what happens in the boundary layer can not be neglected.

In this situation, two options are possible:

"Near wall model approach": to resolve the sub-layer the number of nodes near the wall is increased. Generally, in the sub-layer $y^+ < 30$ $10 \div 15$ nodes the distance of $y^+ \approx 1$ are required. This solution requires the use of a Low-Re-Model and has a high numerical cost.

"Wall function approach": The first node is set outside the inertial sub-layer, i.e. $20 < y^+ < 200$, the High-Re-Model is used to solve the discretization problem. The computational cost is thus drastically reduced; the main disadvantage is that this methodology is validated and justified for near-equilibrium condition boundary layers. This approach is the one used in this thesis project.

4.5 Ignition modelling

A spark plug discharge consists of three phases: breakdown, arc, and glow. The *Fiat FIRE 1.4 16V Turbo CNG* engine ignition has been modelled as an two spherical energy sources, i.e.

Breakdown, which occurs earlier and is of a shorter duration;

Arc/glow, which takes place after the breakdown and is of a longer duration.

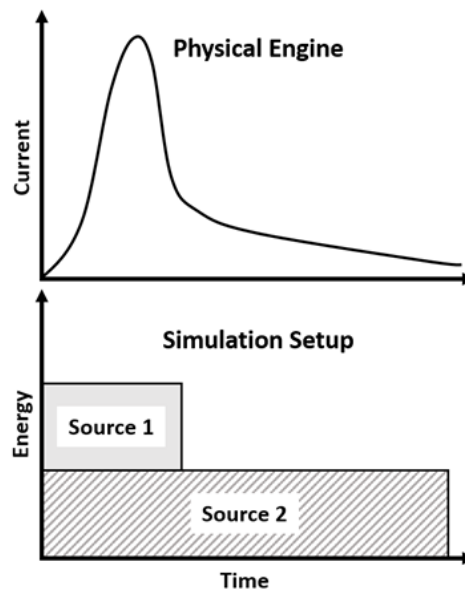
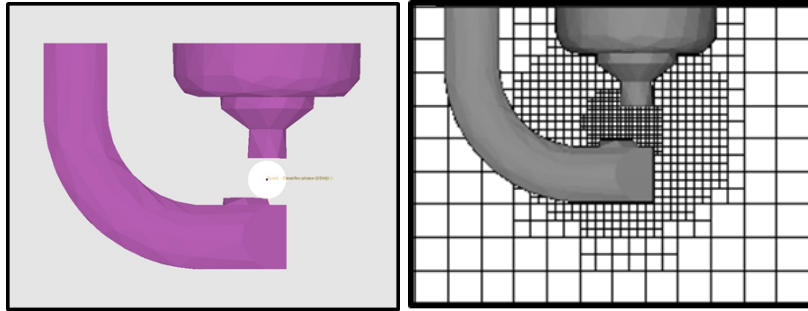


Figure 4.3: Ignition modelling



(a) Ignition modelling: geometry

(b) Additional embedding

Figure 4.4: Modelling Engine Spark with Energy Sources

4.6 Mesh settings

In this thesis project three different meshes have been considered and implemented in CONVERGE, i.e. "*Coarse*", "*Fine*" and "*Finest*", each one characterized by specific base mesh, fixed embeddings and adaptive mesh refinement (AMR) settings.

4.6.1 "Coarse" mesh settings

The "*Coarse*" mesh settings is characterized by a *base grid* of $dx = 0.004m$, $dy = 0.004m$, $dz = 0.004m$.

Fixed embedding settings

For what matters the *Fixed embedding* settings implemented in CONVERGE, specifications are shown in table 4.1.

The minimum mesh size of the spark area is 0.125mm, while for the head and piston, the minimum mesh size is 1mm.

Table 4.1: COARSE mesh settings: Fixed embedding settings specifications

Head	<i>Type:</i>	Boundary
	<i>Mode:</i>	Permanent
	<i>Scale:</i>	2 (2 layers)
Liner	<i>Type:</i>	Boundary
	<i>Mode:</i>	Permanent
	<i>Scale:</i>	2 (2 layers)
Piston	<i>Type:</i>	Boundary
	<i>Mode:</i>	Permanent
	<i>Scale:</i>	2 (2 layers)
Intake valve angle	<i>Type:</i>	Boundary
	<i>Mode:</i>	Cyclic (340-600 deg)
	<i>Scale:</i>	3 (2 layers)
Intake valve top	<i>Type:</i>	Boundary
	<i>Mode:</i>	Cyclic (340-600 deg)
	<i>Scale:</i>	3 (2 layers)
Intake valve bottom	<i>Type:</i>	Boundary
	<i>Mode:</i>	Permanent
	<i>Scale:</i>	3 (2 layers)
Exhaust valve angle	<i>Type:</i>	Boundary
	<i>Mode:</i>	Cyclic (130-380 deg)
	<i>Scale:</i>	2 (2 layers)
Exhaust valve top	<i>Type:</i>	Boundary
	<i>Mode:</i>	Cyclic (130-380 deg)
	<i>Scale:</i>	3 (2 layers)
Exhaust valve bottom	<i>Type:</i>	Boundary
	<i>Mode:</i>	Permanent
	<i>Scale:</i>	3 (2 layers)
Spark 1	<i>Type:</i>	Sphere (r=0.005m)
	<i>Mode:</i>	Cyclic (690-750 deg)
	<i>Scale:</i>	4
Spark 2	<i>Type:</i>	Sphere (r=0.003m)
	<i>Mode:</i>	Cyclic (690-730 deg)
	<i>Scale:</i>	5

AMR settings

For what concerns the Adaptive mesh refinement settings, specifications are reported on the following table. The minimum mesh size is 0.5mm. Specifications of the AMR settings are reported in table 4.2.

	<i>Type:</i>	Boundary
Intake port top	<i>Mode:</i>	Cyclic (340-600 deg)
	<i>Scale:</i>	2 (2 layers)
	<i>Type:</i>	Boundary
Intake port bottom	<i>Mode:</i>	Cyclic (340-600 deg)
	<i>Scale:</i>	2 (2 layers)
	<i>Type:</i>	Boundary
Exhaust port	<i>Mode:</i>	Cyclic (130-380 deg)
	<i>Scale:</i>	2 (2 layers)
	<i>Type:</i>	Cylinder (r1=r2=0.04m)
Cylinder embed	<i>Mode:</i>	Permanent
	<i>Scale:</i>	2

Table 4.2: COARSE mesh settings: AMR settings specifications

	<i>Mode:</i>	Permanent
Cylinder	<i>Velocity max. embedding level:</i>	3
	<i>Velocity sub-grid criterion:</i>	1
	<i>Temperature max. embedding level:</i>	3
	<i>Temperature sub-grid criterion:</i>	2.5
	<i>Mode:</i>	Permanent
Intake system	<i>Velocity max. embedding level:</i>	3
	<i>Velocity sub-grid criterion:</i>	1
		<i>Mode:</i>
Exhaust system	<i>Velocity max. embedding level:</i>	2
	<i>Velocity sub-grid criterion:</i>	1
	<i>Temperature max. embedding level:</i>	2
	<i>Temperature sub-grid criterion:</i>	2.5

4.6.2 "Fine" mesh settings

The "*Fine*" mesh settings is also characterized by a *base grid* of $dx = 0.004m$, $dy = 0.004m$, $dz = 0.004m$.

Fixed embeddings settings

Fixed embeddings settings are the same of the "*Coarse*" mesh, reported in table 4.1. The minimum mesh size of the spark area is 0.125mm, while for the head and piston, the minimum mesh size is 1mm.

AMR settings

The minimum mesh size is 0.25mm.

Specifications of the AMR settings are reported in table 4.3.

Table 4.3: FINE mesh settings: AMR settings specifications

Cylinder	<i>Mode:</i>	Permanent
	<i>Velocity max. embedding level:</i>	4
	<i>Velocity sub-grid criterion:</i>	1
	<i>Temperature max. embedding level:</i>	4
	<i>Temperature sub-grid criterion:</i>	2.5
Intake system	<i>Mode:</i>	Permanent
	<i>Velocity max. embedding level:</i>	3
	<i>Velocity sub-grid criterion:</i>	1
Exhaust system	<i>Mode:</i>	Cyclic (130-380 deg)
	<i>Velocity max. embedding level:</i>	2
	<i>Velocity sub-grid criterion:</i>	1
	<i>Temperature max. embedding level:</i>	2
	<i>Temperature sub-grid criterion:</i>	2.5

4.6.3 "Finest" mesh settings

The "*Finest*" mesh is also characterized by a *base grid* of $dx = 0.004m$, $dy = 0.004m$, $dz = 0.004m$, but has finer *Fixed embedding* and *AMR* settings with respect to the other two.

Fixed embeddings settings

The minimum mesh size of the spark area is 0.125mm, while for the head and piston, the minimum mesh size is 0.5mm. Specifications of the fixed embeddings settings are reported in table 4.4.

Table 4.4: FINEST mesh settings: Fixed embeddings settings specifications

Head	<i>Type:</i>	Boundary
	<i>Mode:</i>	Permanent
	<i>Scale:</i>	3 (2 layers)
Liner	<i>Type:</i>	Boundary
	<i>Mode:</i>	Permanent
	<i>Scale:</i>	2 (2 layers)
Piston	<i>Type:</i>	Boundary
	<i>Mode:</i>	Permanent
	<i>Scale:</i>	3 (2 layers)
Intake valve angle	<i>Type:</i>	Boundary
	<i>Mode:</i>	Cyclic (340-600 deg)
	<i>Scale:</i>	3 (2 layers)
Intake valve top	<i>Type:</i>	Boundary
	<i>Mode:</i>	Cyclic (340-600 deg)
	<i>Scale:</i>	3 (2 layers)
Intake valve bottom	<i>Type:</i>	Boundary
	<i>Mode:</i>	Permanent
	<i>Scale:</i>	3 (2 layers)
Exhaust valve angle	<i>Type:</i>	Boundary
	<i>Mode:</i>	Cyclic (130-380 deg)
	<i>Scale:</i>	2 (2 layers)
Exhaust valve top	<i>Type:</i>	Boundary
	<i>Mode:</i>	Cyclic (130-380 deg)
	<i>Scale:</i>	3 (2 layers)
Exhaust valve bottom	<i>Type:</i>	Boundary
	<i>Mode:</i>	Permanent
	<i>Scale:</i>	3 (2 layers)
Spark 1	<i>Type:</i>	Sphere (r=0.005m)
	<i>Mode:</i>	Cyclic (690-750 deg)
	<i>Scale:</i>	4
Spark 2	<i>Type:</i>	Sphere (r=0.003m)
	<i>Mode:</i>	Cyclic (690-730 deg)
	<i>Scale:</i>	5
Intake port top	<i>Type:</i>	Boundary
	<i>Mode:</i>	Cyclic (340-600 deg)
	<i>Scale:</i>	2 (2 layers)

	<i>Type:</i>	Boundary
Intake port bottom	<i>Mode:</i>	Cyclic (340-600 deg)
	<i>Scale:</i>	2 (2 layers)
	<i>Type:</i>	Boundary
Exhaust port	<i>Mode:</i>	Cyclic (130-380 deg)
	<i>Scale:</i>	2 (2 layers)
	<i>Type:</i>	Cylinder (r1=r2=0.04m)
Cylinder embed	<i>Mode:</i>	Permanent
	<i>Scale:</i>	2

AMR settings

The minimum mesh size is 0.25mm.

Specifications of the *Adaptive mesh refinement* settings are reported in table 4.5.

Table 4.5: FINEST mesh settings: AMR settings specifications

	<i>Mode:</i>	Permanent
Cylinder	<i>Velocity max. embedding level:</i>	4
	<i>Velocity sub-grid criterion:</i>	1
	<i>Temperature max. embedding level:</i>	4
	<i>Temperature sub-grid criterion:</i>	2.5
	<i>Mode:</i>	Permanent
Intake system	<i>Velocity max. embedding level:</i>	3
	<i>Velocity sub-grid criterion:</i>	1
	<i>Mode:</i>	Cyclic (130-380 deg)
Exhaust system	<i>Velocity max. embedding level:</i>	2
	<i>Velocity sub-grid criterion:</i>	1
	<i>Temperature max. embedding level:</i>	2
	<i>Temperature sub-grid criterion:</i>	2.5

Combustion modelling

5.1 Introduction

Combustion is one of the most important processes in engineering, which involves turbulent fluid flow, heat transfer, chemical kinetics, radiative heat transfer and other complicated physical and chemical processes.[1]

Webster's Dictionary provides a useful starting point for a definition of combustion as "*rapid oxidation generating heat, or both light and heat; also, slow oxidation accompanied by relatively little heat and no light*". Restricting this definition to include only the rapid oxidation portion, since it is the aspect on which this thesis project mainly focuses on, it is possible to say that this statement emphasizes the intrinsic importance of chemical reactions to combustion. It also underlines why combustion is so very important: it transforms energy stored in chemical bonds to heat that can be utilized in a variety of ways.[11]

A typical engineering application is that regarding internal combustion engines. It is important to be able to predict the flow, temperatures, resulting species concentrations and emissions from various combustion systems for the design and improvement of combustion equipment. CFD lends itself very well to modelling combustion. Combustion processes are governed by basic transport equations for fluid flow and heat transfer with additional models for combustion chemistry, radiative heat transfer and very important sub/processes.

There are many types of combustion processes, such as gaseous fuel combustion, liquid fuel combustion, spray combustion, solid fuel combustion, pulverised fuel combustion. Combustion beginning, progression and completion depend on the characteristics and the speed of the chemical reactions, on mass and energy transport phenomena which are involved in the reaction zone, and on the heat exchange with the environment.

In this thesis project the attention is focused on the gaseous premixed combustion combustion, as the engine studied is natural gas-spark ignition-ICE, so fuel and oxidant are both in the gas phase, mixed prior the combustion.

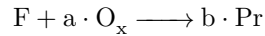
For this kind on engine, combustion is activated by a spark. As the process proceeds, energy is released, leading the gases temperature to increase, while the piston first reduces the volume where oxidation reactions take place, and then it increases it once crossed the TDC. The pressure profile in cylinder in time (and so the mechanical work on the shaft) depends upon the combination of the energy released by the chemical reactions, the variation of the volume due to the piston and the heat flux through the external environment. The process can be distinguished in three phases: a first phase, during which the flame develops and a first portion of fuel burns by the effect of the spark, and so the pressure in cylinder grows above the value imposed by the compression law; a second phase, called "*turbulent combustion phase*", characterised by a sudden propagation of the flame front, turbulent, through most of the combustion chamber, whose volume does not change that much because the piston just moves around the TDC; the last one is the "*combustion completion phase*", in which the flame front reaches the furthest zones of the chamber.

5.2 Chemical kinetics and its application to combustion

Understanding the chemical processes is essential to study combustion. In many combustion processes, chemical reaction rates control the rate of combustion and, usually in all the combustion processes, chemical rates determine pollutant formation and destruction. Also, ignition and flame extinction are intimately related to chemical processes. [11]

Chemical kinetics, also known as *reaction kinetics*, is the study of rates of chemical processes and mechanisms of chemical reactions as well, effect of various variables, including from re-arrangement of atoms, formation of intermediates, etc. It is a huge field that encompasses many aspects of physical chemistry.[14]

The overall reaction of a mole of fuel F with a moles of an oxidizer O_x to form b moles of combustion products Pr can be expressed by the *global reaction mechanism*, i.e.



The *rate* at which the fuel is consumed, w_F , is defined as the change in its molar concentration $[X_F]$ in time, and the relation between the rate and concentrations can often be expressed mathematically in the form of an equation called *rate law*, having the form:

$$w_F = \frac{d[X_F]}{dt} = k_G(T)[X_F]^n[X_{O_x}]^m \quad (5.1)$$

where exponents n and m are constants and relate to the order of the reaction: n is the order with respect to the fuel F , and m is the order with respect to oxidizer O_x . The overall order is $(m + n)$.

Constant $k_G(T)$ is characteristic of the reaction and is called *global rate constant*. It is strongly influenced on temperature, in particular it varies with temperature T according to the *Arrhenius equation*:

$$k_G(T) = A \cdot e^{-\frac{E_a}{RT}} \quad (5.2)$$

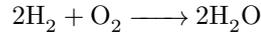
R is the gas constant. E_a is called the activation energy, whose typical values are between 10 and 200 [kJ/mol]. A is called *frequency factor*, or *pre-exponential factor*; it is not strictly constant but depends, according to the *Collision theory*, upon $T^{1/2}$. Although tabulation of experimental values for rate coefficients in *Arrhenius form* is common, current practice frequently uses the three parameter functional form:

$$k_G(T) = A \cdot T^b \cdot e^{-\frac{E_a}{RT}} \quad (5.3)$$

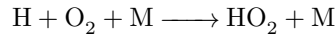
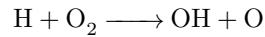
where A, b and E_a are the three empirical parameters.

The use of global reactions to express the chemistry in a specific problem is frequently a "black box" approach, which is for sure useful and intuitive but, on the other hand, it does not provide a basis to understand what is actually happening in the chemistry of the system. Oxidation reactions generally take place in more steps and are "*chain-type*", where intermediate bonds and intermediate species are formed, which are called "*elementary reactions*"; they involve stable intermediate species and radicals (e.g. H, O, OH, HO₂, C₂). These radicals are unstable and highly reactive because they contain unpaired electrons. The actual sequence of the several transformations providing the oxidation of the fuel used in the engine is really complex (intermediate chemical

reactions could be more than hundreds). The collection of elementary reactions necessary to describe an overall reaction is called *reaction mechanism*. An example of global reaction can be that of hydrogen combustion:



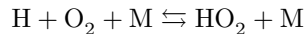
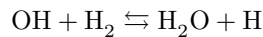
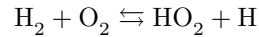
while an example of elementary reactions leading to the same result can be:



This is actually just a partial mechanism, in which it is possible to notice that when oxygen and hydrogen molecules collide and react, they do not form water but, instead, yield the intermediate species HO_2 and a hydrogen atom, which are both radicals. To form HO_2 from H_2 and O_2 , only one bond is broken and one is formed.

Reaction mechanisms may involve few steps (i.e. elementary reactions) or as many as several hundred; they are object of on-going research.

The series of reaction presented is actually a set of forward and reverse reactions, so it would be more correct to rewrite it as:



each line of the partial mechanism is characterized by coefficients k_{fi} and k_{ri} , which are respectively the *forward* and *reverse* coefficients of the i -th reaction. The net rate of production of a species is the sum of all the individual elementary rates producing that species minus the sum of all the rates destroying it. For each species participating to the mechanism it is possible to its *production rate*, which is the rate at which the each reaction product is produced. For the i th-species, it is defined as

$$w_i = \frac{d[X_i]}{dt} = f_i([X_1](t), [X_2](t), \dots, [X_n](t)) \quad (5.4)$$

which is a system of first-order ODE that describes the evolution of the chemical system starting from given initial conditions, and couples any necessary statements of mass, momentum, energy conservation and state equations.

Knowing how to express the rates of elementary reactions, it is possible to express mathematically the net rates of production or destruction for any participating species in a series of elementary reactions.

Mechanisms might involve lots of elementary reactions and species; therefore, it is convenient to use a compact notation to represent the mechanism and the individual species production rates; so, for the mechanism, one can write:

$$\sum_{j=1}^N \nu'_{ji} X_j \rightleftharpoons \sum_{j=1}^N \nu''_{ji} X_j \quad (5.5)$$

for $i = 1, 2, \dots, L$.

Constants ν'_{ji} and ν''_{ji} are the stoichiometric coefficients for the reactants and products, respectively, for species j and reaction i ; L is the total number of reactions. The net production rate of species j is given by:

$$\dot{\omega}_j = \sum_{i=1}^L \nu_{ji} q_i \quad (5.6)$$

for $j = 1, 2, \dots, N$. N is the total number of species and

$$\nu_{ji} = (\nu''_{ji} - \nu'_{ji}) \quad (5.7)$$

while q_i is the rate-of-progress variable for the i -th reaction, and is expressed as:

$$q_i = k_{fi} \prod_{j=1}^N [X_j]^{\nu'_{ji}} - k_{ri} \prod_{j=1}^N [X_j]^{\nu''_{ji}} \quad (5.8)$$

The software CHEMKIN is a widely used general-purpose package for solving chemical kinetics problems.

5.3 Combustion models in CONVERGE

CONVERGE contains a detailed chemistry solver and simplified combustion models, including models for general combustion, premixed combustion, diesel combustion, non-premixed turbulence combustion, and simplified general chemistry. CONVERGE also includes several emissions models.

The *SAGE detailed chemistry solver* is the most predictive and accurate way to model combustion and models accurately ignition and laminar flame propagation.

The *Simplified combustion models* are generally less computationally expensive and predictive than SAGE, and may provide acceptable results for specific applications.

5.3.1 Simplified Combustion Models in CONVERGE

Simplified Combustion Modelling can be subdivided into *Non-premixed turbulent combustion models* and *Premixed turbulent combustion models*. Among the formers, the main models are:

- Characteristic Time Combustion (CTC);
- Shell Ignition;
- Chemical Equilibrium (CEQ), which is computationally inexpensive compared to SAGE, but whose main disadvantage is the instantaneous combustion due to equilibrium chemistry;
- Representative Interactive Flamelet (RIF);
- Extended Coherent Flame Model with the 3Z mixing model (ECFM3Z).

The main Premixed turbulent combustion models are:

- Chemical Equilibrium (CEQ);
- G-Equation;
- Extended Coherent Flame Model (ECFM), which explicitly accounts for turbulence effects on ignition and flame propagation, and ISSIM (spark model) simulates electrical circuit, but has the disadvantage that it requires the laminar flame speeds and is less predictive than SAGE;
- Flamelet Generated Manifold (FGM) (not recommended for IC engines)

Details about these combustion models will not be dealt with in this thesis project. Just some basic information about the ECFM model are given in the next paragraph.

ECFM model

Extended Coherent Flame Model (ECFM) is a premixed combustion model, is an extension of the Coherent Flame Model proposed by Marble and Broadwell (1977). It can be particularly accurate for spark-ignited engines, contains an optional spark model and uses the fuel/air equivalence ratio, the composition, and the temperature near the flame to determine the flame surface density. The transported flame surface density is used to describe the burned/unburned stratification.

5.4 SAGE Detailed Chemical Kinetics Solver

The SAGE detailed chemistry solver (Senecal et al., 2003) is the combustion model used in this work thesis. It uses local conditions to calculate reaction rates based on principles of chemical kinetics. Given an accurate mechanism, SAGE (in addition to AMR) can be used for modelling many combustion regimes (ignition, premixed, mixing-controlled). This model is the one adopted in this thesis project. SAGE solver

- Reads in a reaction mechanism in CHEMKIN format (the combustion of different fuels can be modelled by changing the mechanism, e.g., there are mechanisms for iso-octane, gasoline, n-heptane, natural gas, etc.) and solves ODEs to find the reaction rates;
- Couples with the transport solver via source terms in the species transport equations;
- Parallelizes independently of the flow solver;
- Each time-step, calculates the new species mass fractions immediately and the reaction rates for each elementary reaction prior to solving the transport equations. The change in the species mass fractions is treated as a source;
- Uses CGS units for all calculations.

A simulation with SAGE must contain:

- A reaction mechanism file (e.g., contained in a file called `mech.dat`);
- A species-specific thermodynamic properties file (e.g., contained in a file called `therm.dat`);
- Molecular transport properties in a file called `gas.dat` or, if mixture-averaged diffusion is considered, in a file called `transport.dat`.

Keeping in mind all the theory about Chemical kinetics previously reported, further theory details about SAGE is here reported. In SAGE, the *forward rate coefficient* for the i -th reaction is expressed by the *Arrhenius form* as

$$k_{fi}(T) = A_i \cdot T^b \cdot e^{-\frac{E_{a,i}}{RT}} \quad (5.9)$$

The *reverse rate coefficient* can be user-specified or calculated from the equilibrium coefficient, which is determined from properties in the thermodynamic data file (e.g., `therm.dat`), as

$$k_{ri}(T) = \frac{k_{fi}}{K_{ci}} \quad (5.10)$$

The equilibrium coefficient K_{ci} is determined from the thermodynamic properties and is given by

$$k_{K_{ci}} = K_{pi} \frac{p_{atm}^{\sum_{j=1}^N \nu_{ij}}}{RT} \quad (5.11)$$

where p_{atm} is the atmospheric pressure. The equilibrium constant K_{pi} is obtained by:

$$K_{pi} = \exp\left(\frac{\Delta S_i^0}{R} - \frac{\Delta H_i^0}{RT}\right) \quad (5.12)$$

where S and H respectively represent entropy and enthalpy, and Δ refers to the change that occurs in passing completely from reactants to products in the i -th reaction, namely:

$$\frac{\Delta S_i^0}{R} = \sum_j^N \nu_{ji} \frac{S_j^0}{R} \quad (5.13)$$

$$\frac{\Delta H_i^0}{RT} = \sum_j^N \nu_{ji} \frac{H_j^0}{RT} \quad (5.14)$$

With the above information, the continuity and the energy conservation equations can be solved for a given computational cell. These are in the form:

$$\frac{d[X_j]}{dt} = \dot{\omega}_j \quad (5.15)$$

$$\frac{dT}{dt} = \frac{V \frac{dp}{dt} - \sum_j^N (\bar{h}_j \dot{\omega}_j)}{\sum_j^N ([X_j] \bar{c}_{p,j})} \quad (5.16)$$

where V is the volume, T is the temperature, p is the pressure, and \bar{h}_j and $\bar{c}_{p,j}$ are respectively the molar specific enthalpy and molar constant-pressure specific heat of species j . The above equations are solved at each computational time step and the species are updated appropriately. It is important to note that the temperature obtained from Equation 5.16 is used to update only the rate coefficients as SAGE is solving the system of rate equations and is not used to update the CONVERGE cell temperature. The cell temperature is updated after the detailed chemistry calculation has converged using the computed species concentrations.

In order to expedite the detailed chemistry calculations, kinetics are not solved in cells that fall below a minimum cell temperature (T_{cut}) and a minimum mole fraction (HC_{min}). The minimum mole fraction is the total mole fraction of CO, H₂, and the hydrocarbon species. The minimum mole fraction includes more than just the hydrocarbon species to allow carbon monoxide chemistry to take place in computational cells that do not include hydrocarbon species.

5.4.1 Mechanisms used

In literature it is possible to find lots of reaction mechanisms to model natural gas combustion, such as *GRI-mech 3.0*, *Aramco-mech 2.0*, *USC-mech II*, *NUI-Galaway mech*, *Princeton-mech*, etc.

The mechanisms considered in this thesis project are:

- GRI-Mech 3.0;
- USC-Mech II;
- Aramco-Mech 2.0.

Figures 5.1, 5.2, and 5.3 report parts of the *GRI-Mech 3.0* kinetic mechanism files, so one can notice how a mechanism is composed. The format is the same also for the other mechanisms.

```

! GRI-Mech Version 3.0 7/30/99 CHEMKIN-II format
! See README30 file at anonymous FTP site unix.sri.com, directory gri;
! WorldWideWeb home page http://www.me.berkeley.edu/gri_mech/ or
! through http://www.gri.org , under 'Basic Research',
! for additional information, contacts, and disclaimer
ELEMENTS
O H C N AR
END
SPECIES
H2 H O O2 OH H2O H02 H2O2
C CH CH2 CH2(S) CH3 CH4 CO CO2
HCO CH2O CH2OH CH3O CH3OH C2H C2H2 C2H3
C2H4 C2H5 C2H6 HCCO CH2CO HCCOH N NH
NH2 NH3 NNH NO N02 N2O HNO CN
HCN H2CN HCNN HCNO HOCN HNCO NCO N2
AR C3H7 C3H8 CH2CHO CH3CHO
END
!THERMO
! Insert GRI-Mech thermodynamics here or use in default file
!END
REACTIONS
2O+M<=>O2+M 1.200E+17 -1.000 .00
H2/ 2.40/ H2O/15.40/ CH4/ 2.00/ CO/ 1.75/ CO2/ 3.60/ C2H6/ 3.00/ AR/ .83/
O+H+M<=>OH+M 5.000E+17 -1.000 .00
H2/2.00/ H2O/6.00/ CH4/2.00/ CO/1.50/ CO2/2.00/ C2H6/3.00/ AR/ .70/
O+H2<=>H+OH 3.870E+04 2.700 6260.00
O+H02<=>OH+O2 2.000E+13 .000 .00
O+H2O2<=>OH+H02 9.630E+06 2.000 4000.00
O+CH<=>H+CO 5.700E+13 .000 .00
O+CH2<=>H+HCO 8.000E+13 .000 .00
O+CH2(S)<=>H2+CO 1.500E+13 .000 .00
O+CH2(S)<=>H+HCO 1.500E+13 .000 .00
O+CH3<=>H+CH2O 5.060E+13 .000 .00
O+CH4<=>OH+CH3 1.020E+09 1.500 8600.00
O+CO(+M)<=>CO2(+M) 1.800E+10 .000 2385.00
LOW/ 6.020E+14 .000 3000.00/
H2/2.00/ O2/6.00/ H2O/6.00/ CH4/2.00/ CO/1.50/ CO2/3.50/ C2H6/3.00/ AR/ .50/
O+HCO<=>OH+CO 3.000E+13 .000 .00
O+HCO<=>H+CO2 3.000E+13 .000 .00
O+CH2O<=>OH+HCO 3.900E+13 .000 3540.00
O+CH2OH<=>OH+CH2O 1.000E+13 .000 .00
O+CH3O<=>OH+CH2O 1.000E+13 .000 .00
O+CH3OH<=>OH+CH2OH 3.880E+05 2.500 3100.00
O+CH3OH<=>OH+CH3O 1.300E+05 2.500 5000.00
O+C2H<=>CH+CO 5.000E+13 .000 .00
O+C2H2<=>H+HCCO 1.350E+07 2.000 1900.00
O+C2H2<=>OH+C2H 4.600E+19 -1.410 28950.00
O+C2H2<=>CO+CH2 6.940E+06 2.000 1900.00

```

Figure 5.1: *GRI-Mech 3.0*: mech.dat file (partial)

```

THERMO
 300.000 1000.000 5000.000
! GRI-Mech Version 3.0 Thermodynamics released 7/30/99
! NASA Polynomial format for CHEMKIN-II
! see README file for disclaimer
O          L 1/900  1          G  200.000  3500.000  1000.000  1
 2.56942078E+00-8.59741137E-05 4.19484589E-08-1.00177799E-11 1.22833691E-15  2
 2.92175791E+04 4.78433864E+00 3.16826710E+00-3.27931884E-03 6.64306396E-06  3
-6.12806624E-09 2.11265971E-12 2.91222592E+04 2.05193346E+00  4
O2         TPI5890  2          G  200.000  3500.000  1000.000  1
 3.28253784E+00 1.48308754E-03-7.57966669E-07 2.09470555E-10-2.16717794E-14  2
-1.08845772E+03 5.45323129E+00 3.78245636E+00-2.99673416E-03 9.84730201E-06  3
-9.68129509E-09 3.24372837E-12-1.06394356E+03 3.65767573E+00  4
H          L 7/88H  1          G  200.000  3500.000  1000.000  1
 2.50000001E+00-2.30842973E-11 1.61561948E-14-4.73515235E-18 4.98197357E-22  2
 2.54736599E+04-4.46682914E-01 2.50000000E+00 7.05332819E-13-1.99591964E-15  3
 2.30081632E-18-9.27732332E-22 2.54736599E+04-4.46682853E-01  4
H2         TPI578H  2          G  200.000  3500.000  1000.000  1
 3.33727920E+00-4.94024731E-05 4.99456778E-07-1.79566394E-10 2.00255376E-14  2
-9.50158922E+02-3.20502331E+00 2.34433112E+00 7.98052075E-03-1.94781510E-05  3
 2.01572094E-08-7.37611761E-12-9.17935173E+02 6.83010238E-01  4
OH         RUS 780  1H  1          G  200.000  3500.000  1000.000  1
 3.09288767E+00 5.48429716E-04 1.26505228E-07-8.79461556E-11 1.17412376E-14  2
 3.85865700E+03 4.47669610E+00 3.99201543E+00-2.40131752E-03 4.61793841E-06  3
-3.88113333E-09 1.36411470E-12 3.61508056E+03-1.03925458E-01  4
H2O        L 8/89H  20  1          G  200.000  3500.000  1000.000  1
 3.03399249E+00 2.17691804E-03-1.64072518E-07-9.70419870E-11 1.68200992E-14  2
-3.00042971E+04 4.96677010E+00 4.19864056E+00-2.03643410E-03 6.52040211E-06  3
-5.48797062E-09 1.77197817E-12-3.02937267E+04-8.49032208E-01  4
HO2        L 5/89H  10  2          G  200.000  3500.000  1000.000  1
 4.01721090E+00 2.23982013E-03-6.33658150E-07 1.14246370E-10-1.07908535E-14  2
 1.11856713E+02 3.78510215E+00 4.30179801E+00-4.74912051E-03 2.11582891E-05  3
-2.42763894E-08 9.29225124E-12 2.94808040E+02 3.71666245E+00  4
H2O2       L 7/88H  20  2          G  200.000  3500.000  1000.000  1
 4.16500285E+00 4.90831694E-03-1.90139225E-06 3.71185986E-10-2.87908305E-14  2
-1.78617877E+04 2.91615662E+00 4.27611269E+00-5.42822417E-04 1.67335701E-05  3
-2.15770813E-08 8.62454363E-12-1.77025821E+04 3.43505074E+00  4
C          L11/88C  1          G  200.000  3500.000  1000.000  1
 2.49266888E+00 4.79889284E-05-7.24335020E-08 3.74291029E-11-4.87277893E-15  2
 8.54512953E+04 4.80150373E+00 2.55423955E+00-3.21537724E-04 7.33792245E-07  3
-7.32234889E-10 2.66521446E-13 8.54438832E+04 4.53130848E+00  4
CH         TPI579C  1H  1          G  200.000  3500.000  1000.000  1
 2.87846473E+00 9.70913681E-04 1.44445655E-07-1.30687849E-10 1.76079383E-14  2
 7.10124364E+04 5.48497999E+00 3.48981665E+00 3.23835541E-04-1.68899065E-06  3
 3.16217327E-09-1.40609067E-12 7.07972934E+04 2.08401108E+00  4
CH2        L S/93C  1H  2          G  200.000  3500.000  1000.000  1
 2.87410113E+00 3.65639292E-03-1.40894597E-06 2.60179549E-10-1.87727567E-14  2
 4.62636040E+04 6.17119324E+00 3.76267867E+00 9.68872143E-04 2.79489841E-06  3
 3.95001155E-09 1.68741710E-12 4.60040401E+04 1.56252185E+00  4

```

Figure 5.2: *GRI-Mech 3.0*: therm.dat file (partial)

GRI-Mech 3.0

The *GRI-Mech 3.0* is an optimized mechanism designed to model natural gas combustion, including NO formation and reburn chemistry.

This mechanism has been developed sponsored by the *Gas Research Institute* (GRI) and carried out at *The University of California* at Berkeley, *Stanford University*, *The University of Texas at Austin*, and *SRI International*.

It is essentially a compilation of **325 elementary chemical reactions** and associated rate coefficient expressions and thermochemical parameters for the **53 species** involved in them.

USC Mech II

The *USC Mech II* is H₂/CO/C1-C4 kinetic model, applicable to a wide variety of combustion scenarios, incorporates the recent thermodynamics, kinetic, and species transport updates relevant to high-temperature oxidation of hydrogen, carbon monoxide, and C1-C4 hydrocarbons.

It has been developed by Hai Wang, Xiaoqing You, Ameya V. Joshi, Scott G. Davis,

AR	0	136.500	3.330	0.000	0.000	0.000	
C	0	71.400	3.298	0.000	0.000	0.000	!
C2	1	97.530	3.621	0.000	1.760	4.000	*
C20	1	232.400	3.828	0.000	0.000	1.000	!
CN2	1	232.400	3.828	0.000	0.000	1.000	! OIS
C2H	1	209.000	4.100	0.000	0.000	2.500	
C2H2	1	209.000	4.100	0.000	0.000	2.500	
C2H20H	2	224.700	4.162	0.000	0.000	1.000	!
C2H3	2	209.000	4.100	0.000	0.000	1.000	!
C2H4	2	280.800	3.971	0.000	0.000	1.500	*
C2H5	2	252.300	4.302	0.000	0.000	1.500	
C2H6	2	252.300	4.302	0.000	0.000	1.500	
C2N	1	232.400	3.828	0.000	0.000	1.000	!
C2N2	1	349.000	4.361	0.000	0.000	1.000	! OIS
C3H2	2	209.000	4.100	0.000	0.000	1.000	!
C3H4	1	252.000	4.760	0.000	0.000	1.000	*
C3H6	2	266.800	4.982	0.000	0.000	1.000	
C3H7	2	266.800	4.982	0.000	0.000	1.000	
C4H6	2	357.000	5.180	0.000	0.000	1.000	
I*C3H7	2	266.800	4.982	0.000	0.000	1.000	
N*C3H7	2	266.800	4.982	0.000	0.000	1.000	
C3H8	2	266.800	4.982	0.000	0.000	1.000	
C4H	1	357.000	5.180	0.000	0.000	1.000	
C4H2	1	357.000	5.180	0.000	0.000	1.000	
C4H20H	2	224.700	4.162	0.000	0.000	1.000	!
C4H8	2	357.000	5.176	0.000	0.000	1.000	*
C4H9	2	357.000	5.176	0.000	0.000	1.000	
I*C4H9	2	357.000	5.176	0.000	0.000	1.000	
C5H2	1	357.000	5.180	0.000	0.000	1.000	
C5H3	1	357.000	5.180	0.000	0.000	1.000	
C6H2	1	357.000	5.180	0.000	0.000	1.000	
C6H5	2	412.300	5.349	0.000	0.000	1.000	!
C6H50	2	450.000	5.500	0.000	0.000	1.000	! JAM
C5H50H	2	450.000	5.500	0.000	0.000	1.000	! JAM
C6H6	2	412.300	5.349	0.000	0.000	1.000	! SVE
C6H7	2	412.300	5.349	0.000	0.000	1.000	! JAM
CH	1	80.000	2.750	0.000	0.000	0.000	
CH2	1	144.000	3.800	0.000	0.000	0.000	
CH2(s)	1	144.000	3.800	0.000	0.000	0.000	
CH2*	1	144.000	3.800	0.000	0.000	0.000	
CH2CHCCH	2	357.000	5.180	0.000	0.000	1.000	!
CH2CHCCH2	2	357.000	5.180	0.000	0.000	1.000	!
CH2CHCH2	2	260.000	4.850	0.000	0.000	1.000	!
CH2CHCHCH	2	357.000	5.180	0.000	0.000	1.000	!
CH2CHCHCH2	2	357.000	5.180	0.000	0.000	1.000	!
CH2CO	2	436.000	3.970	0.000	0.000	2.000	
CH2O	2	498.000	3.590	0.000	0.000	2.000	
CH2OH	2	417.000	3.690	1.700	0.000	2.000	
CH3	1	144.000	3.800	0.000	0.000	0.000	

Figure 5.3: *GRI-Mech 3.0*: transport.dat file (partial)

Alexander Laskin, Fokion Egolfopoulos and Chung K. Law, *USC Viterbi-Southern University of California*.

The mechanism collects **111 species** and **784 elementary chemical reactions**.

AramcoMech 2.0

The *AramcoMech 2.0* is an optimized detailed chemical reaction mechanism, capable to represent the kinetic and thermochemical properties of a large number of C1–C4 based hydrocarbon and oxygenated fuels over a wide range of experimental conditions.

It is proposed by the *Combustion Chemistry Centre* at NUI Galway and has been funded by *Saudi Aramco*.

This mechanism contains **2716 elementary chemical reactions** and associated rate coefficient expressions and thermochemical parameters for the **493 species** involved in them.

The main characteristics of the mechanisms used are summarized in table 5.1.

Table 5.1: Mechanisms specifications

Mechanism	Elements no.	Species no.	Reactions no.
<i>GRI-Mech 3.0</i>	5	53	325
<i>USC-Mech II</i>	5	111	784
<i>AramcoMech 2.0</i>	6	493	2716

5.4.2 Mechanisms validation and comparison

In order to check the goodness of the reaction mechanisms considered in this thesis project, a thorough validation with experimental data found in literature has been carried out. These data have been compared with results obtained through Zero-Dimensional and One-Dimensional Simulations in CONVERGE by using the different mechanisms. The validation parameters are:

- Ignition delay [s];
- Laminar flame speed [m/s].

whose concepts are essential to be known before going any further.

Ignition delay

Ignition delay is the time interval between the fuel injection and its ignition. This delay period consists of a physical delay, in which atomization, vaporization and mixing or air-fuel occur, and of a chemical delay, attributed to a pre-combustion reactions.

The ignition delay time is a readily measurable quantity that is a function of the initial temperature, pressure, and composition of the reactant mixture. For methane, it has been found that the ignition delay time can be correlated in the form:

$$t = A \cdot e^{\frac{E_a}{RT}} [\text{CH}_4]^a [\text{O}_2]^b \quad (5.17)$$

where the term E_a is, as previously, a parameter equivalent to a global activation energy and A is an empirically determined constant. The terms $[\text{CH}_4]$ and $[\text{O}_2]$ are the molar concentrations of methane and oxygen, respectively, in the combustible mixture. The empirical exponents a and b of these terms express the power dependencies of ignition delay time on fuel and oxidizer concentrations. Correlation of experimental data for methane by means of this equation shows that ignition delay time decreases for both increasing temperature and increasing pressure.

Over the years, a wide variety of experimental techniques have been used to measure ignition delay times of fuels, such as constant-volume bombs, continuous-flow test apparatus, and shock tubes.

A *shock tube* is used in ignition studies to produce a high temperature gas under well-controlled test conditions. A shock tube is a tube of cylindrical or rectangular cross-section in which a transverse diaphragm separates two masses of gas initially at rest. One mass is at high pressure and is considered the driver section of the tube. The other mass, in the driven section, is at low pressure and forms the ignitable mixture of interest. The diaphragm is burst by either mechanically piercing it or by exceeding its structural strength through over-pressurization of the driver section. This action sends a strong shock wave into the low pressure section increasing the static pressure and temperature of the mixture. The shock wave is reflected at the end boundary wall of the tube resulting in an additional increase in pressure and temperature. By tailoring pressure levels within the two sections of the tube, a variety of shock strengths can be produced leading to a wide range of test conditions. [16]

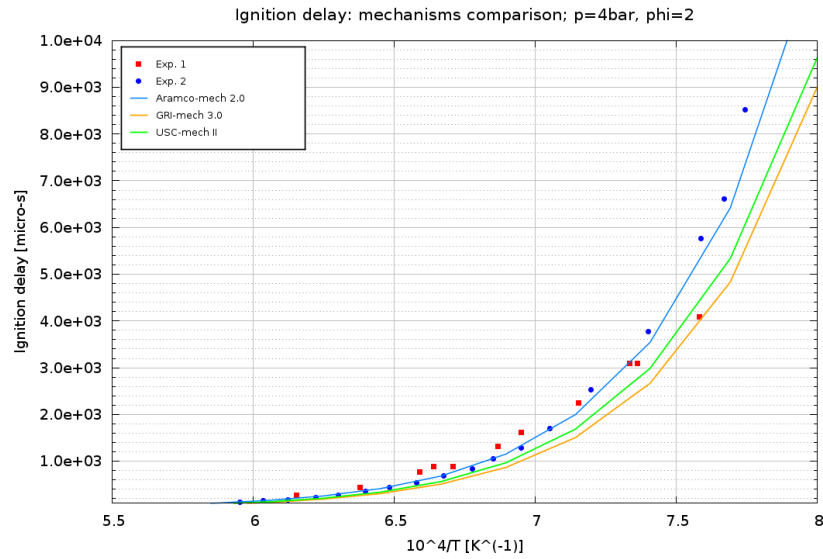


Figure 5.4: Ignition delay for $p = 0.4\text{MPa}$, $\phi = 2$

The ignition delay measurements data found in literature for pure CH_4 have been carried out by experiments in a shock tube by Xi'an Jiaotong University (China), ZHANG YingJia, HUANG ZuoHua, WEI LiangJie and NIU ShaoDong.

Figure 5.4 shows the comparison between measured ignition delays and model calculation in CONVERGE Studio2.3 in the Chemistry Module for methane using three available mechanisms, i.e. *GRI-Mech 3.0*, *AramcoMech 2.0* and *USC-Mech II*. All the mechanisms provide accurate results, as they conform the experimental data.

Ignition delay simulations have been carried out also at particular engine conditions (i.e. at spark conditions), in order to see how the different mechanisms behave at those situations and to make some comparisons. For these simulations, o.p. 2000 [rpm] x 3.6 [bar] x lambda=1 has been considered. Results are shown in figures 5.5 and 5.6.

In figure 5.5 one can notice that the mechanisms behave quite differently, but, at $T = 700\text{K}$, which is more or less the temperature reached in the chamber at crank angle=694 deg, they present almost the same ignition delay value; the *GRI-Mech 3.0* turns out to be the mechanism which provides the "shortest" ignition delay, but the difference with respect to the others is quite negligible.

In figure 5.6 it is possible to see that the mechanisms behave quite differently after $T = 800\text{K}$; nevertheless, at $T = 800\text{K}$, which is more or less the temperature reached in the chamber at crank angle=710 deg, they present almost the same ignition delay value; the *Aramco-Mech2.0* turns out to be the mechanism which provides the "shortest" ignition delay, but the difference with respect to the others is really small.

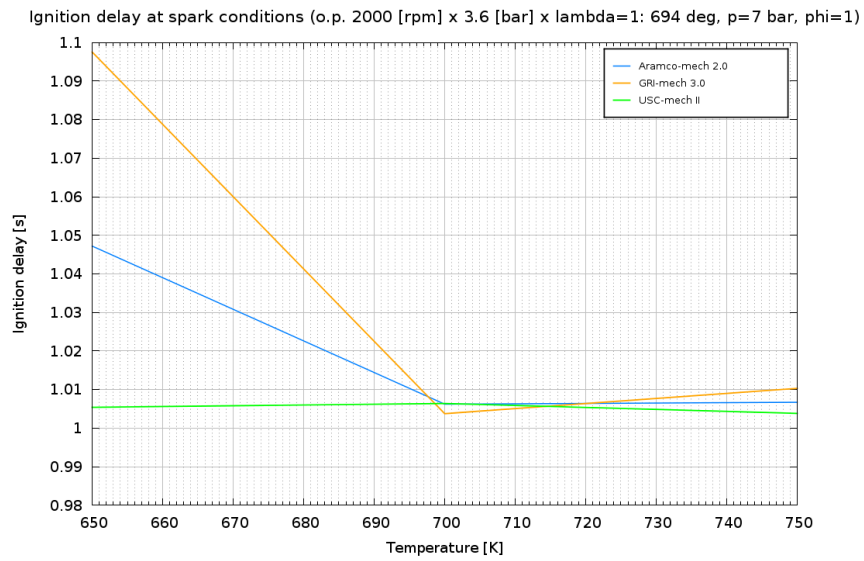


Figure 5.5: Ignition delay at spark conditions for o.p. 2000 [rpm] x 3.6 [bar] x lambda=1: 694 deg crank angle, $p = 7$ bar, $\phi = 1$ [-]

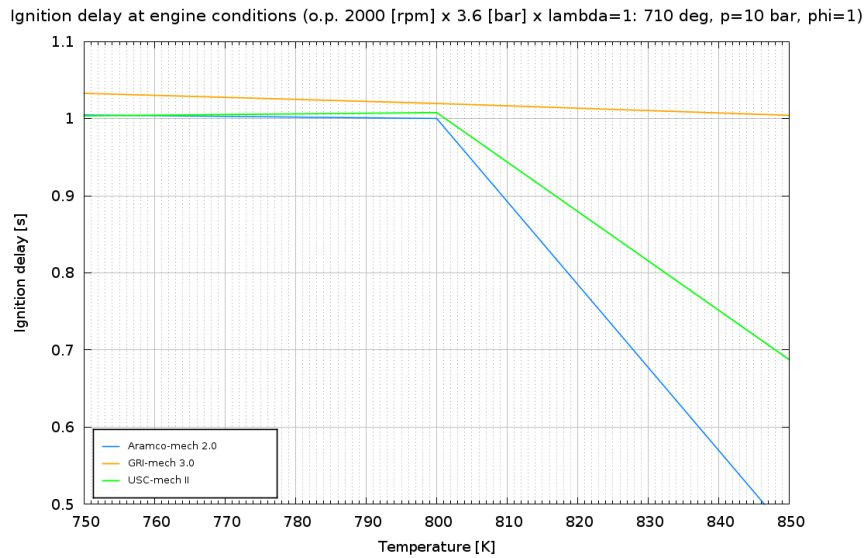


Figure 5.6: Ignition delay at engine conditions for o.p. 2000 [rpm] x 3.6 [bar] x lambda=1: 710 deg crank angle, $p = 10$ bar, $\phi = 1$ [-]

Laminar flame speed

The velocity at which the flame front moves with respect to the fresh charge is called *combustion laminar speed*, w_{cl} , and depends on the nature of the fuel, on the equivalence ratio ϕ and its temperature and pressure. The value of w_{cl} is determined by how fast mass and energy transport phenomena take place in the flame front, causing the initial heating of the mixture and the sufficient amount of active particles for the start of the oxidation reactions, and on the velocity at which these reactions proceed inside the flame front w_r .

The motion conditions of the fresh charge inside the cylinder of an engine are, actually, mostly turbulent and therefore the combustion process takes place quite differently with respect to those with laminar flames. In these situations, larger eddies twist the flame front and, as a consequence, its superficial extension increases substantially, while smaller eddies intensify the transport phenomena. The *combustion turbulent speed*, w_{ct} , therefore, beyond composition, temperature and pressure of the mixture, depends on the motions conditions.

Flame speed simulations have been performed for pure methane in air in CONVERGE Studio2.3 in the Chemistry Module-One-Dimensional, for different pressure conditions. Validation cases are reported in table 5.2. Figures 5.7, 5.8, 5.9, 5.10, 5.11, 5.12

Table 5.2: Mechanisms validation cases for laminar flame speed

Pressure [bar]	ϕ value(s) [-]	Temperature [K]
1	0.7÷1.3	298
5	0.7÷1.3	400, 500, 600
20	0.7÷1.2	400, 500

show the comparison between the simulation results obtained in CONVERGE with the three different mechanisms used with the experimental data found in literature.

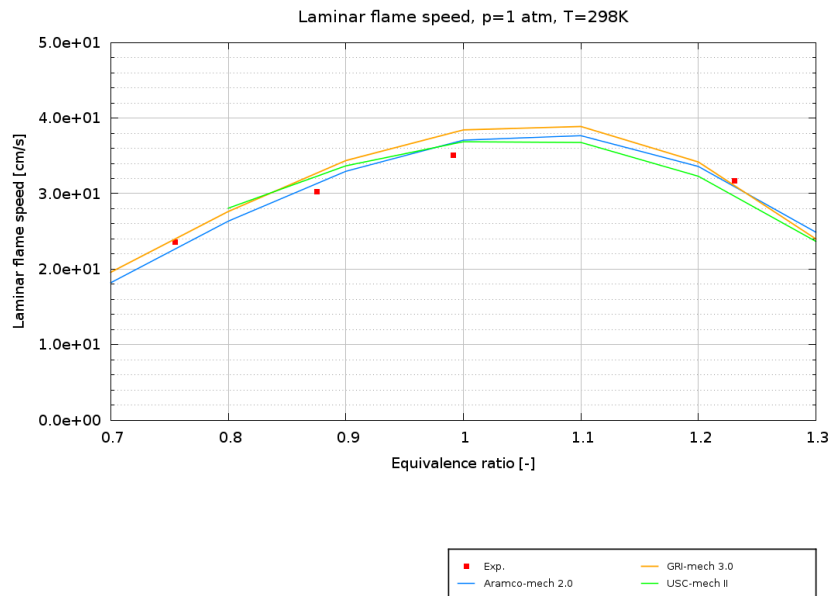


Figure 5.7: Laminar flame speed for pure CH_4 , $p = 1\text{bar}$, $T = 298\text{K}$

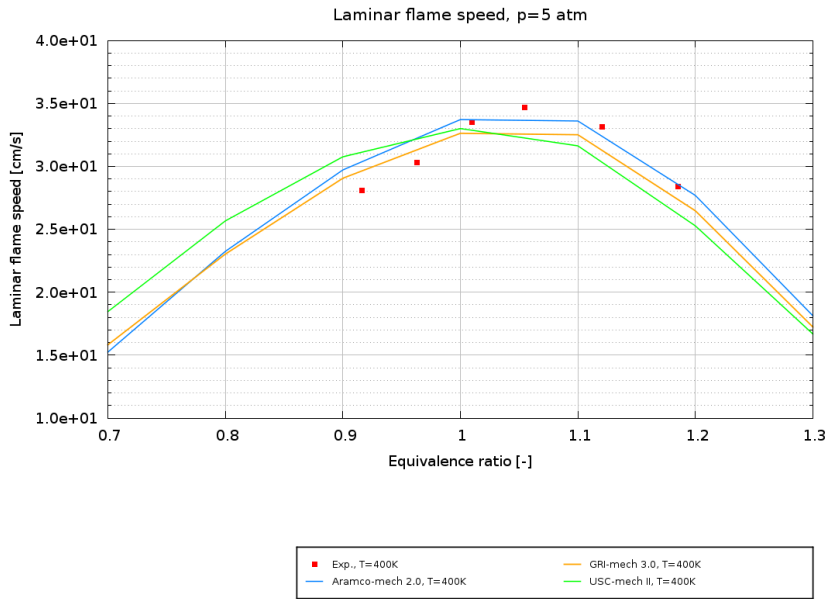


Figure 5.8: Laminar flame speed for pure CH_4 , $p = 5\text{bar}$, $T = 400\text{K}$

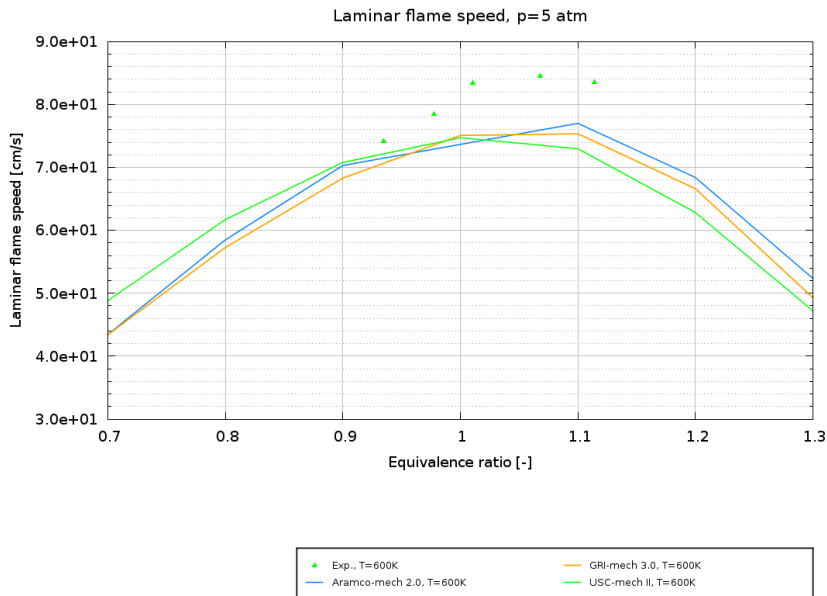


Figure 5.9: Laminar flame speed for pure CH_4 , $p = 5\text{bar}$, $T = 500\text{K}$

In case $p = 1\text{bar}$, $T = 298\text{K}$ (fig. 5.7) the One-Dimensional simulation results follow the experimental data in a very satisfactory manner, as well as in case $p = 5\text{bar}$, $T = 400\text{K}$ (fig. 5.8).

Then, for the same pressure conditions, at higher temperatures (fig. 5.9 and fig. 5.10) experimental data and simulation results become a little more different, but still reasonably accurate.

In case $p = 20\text{bar}$ (Figures. 5.11 and 5.12) the One-Dimensional simulation results are a little underestimated with respect to the the experimental data, but they can

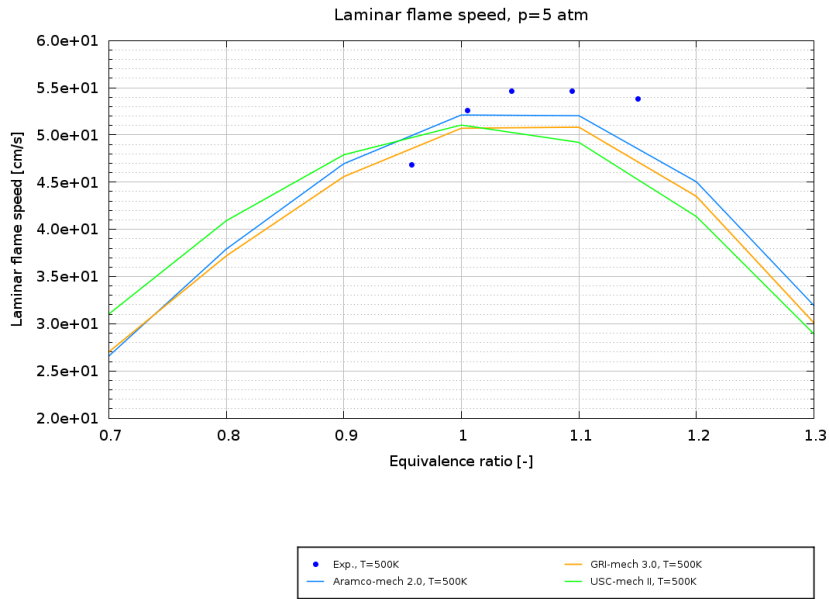


Figure 5.10: Laminar flame speed for pure CH_4 , $p = 5\text{bar}$, $T = 600\text{K}$

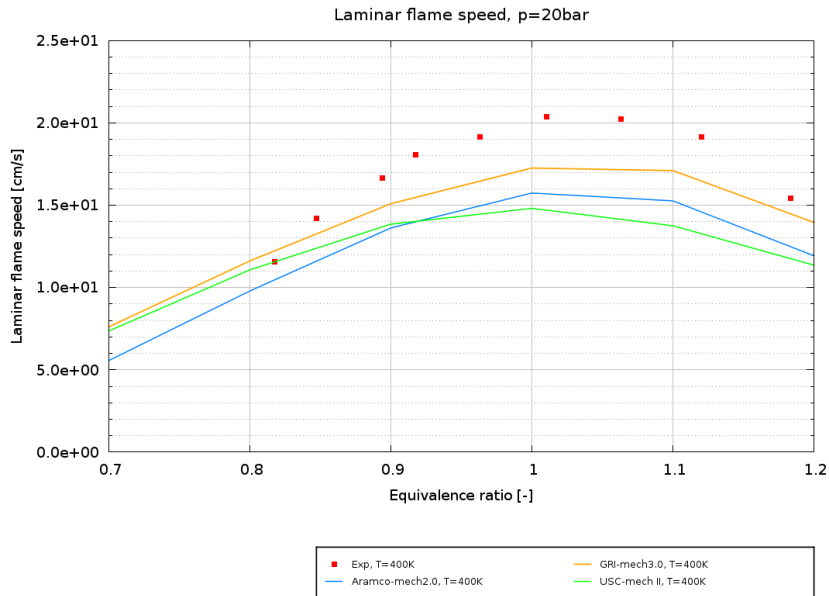


Figure 5.11: Laminar flame speed for pure CH_4 , $p = 20\text{bar}$, $T = 400\text{K}$

be still considered good.

Laminar flame speed simulations have been carried out also at particular engine conditions (i.e. at spark conditions, at peak pressure conditions, and at an engine condition at a crank angle inbetween these two), in order to see how the different mechanisms behave at those situations and to make some comparisons. For these simulations, o.p. 2000 [rpm] x 3.6 [bar] x lambda=1 has been considered. Results are shown in figures 5.13, 5.14 and 5.15.

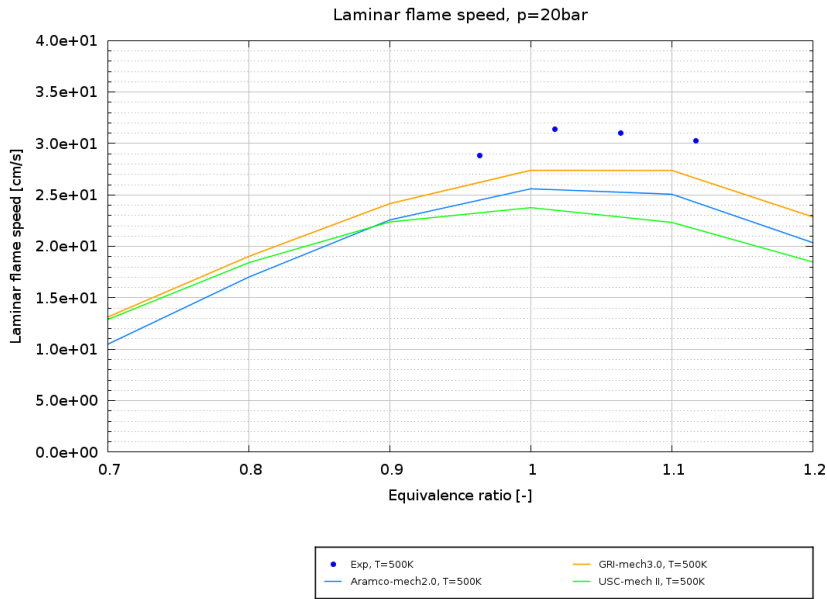


Figure 5.12: Laminar flame speed for pure CH_4 , $p = 20\text{bar}$, $T = 500\text{K}$

In figure 5.13 one can notice that the mechanisms have the same trend and, at $\phi = 1$, which is the engine equivalence ratio, they present a very similar laminar flame speed value; the *Aramco-Mech2.0* turns out to be the mechanism which provides the highest laminar flame speed, but the difference with respect to the others is not that big.

In figure 5.14 it is possible to see that the mechanisms behave quite differently after $\phi = 1$, but the trend is still reasonably coherent. For $\phi = 1$ the *Aramco-Mech2.0* is the mechanism which provides the highest laminar flame speed, but the difference with respect to the others is quite small.

In figure 5.15, the situation is very similar to that of the other two cases.

Laminar flame speed at spark conditions (o.p. 2000 [rpm] x 3.6 [bar] x lambda=1: 694 deg, p=7 bar, T=700 K)

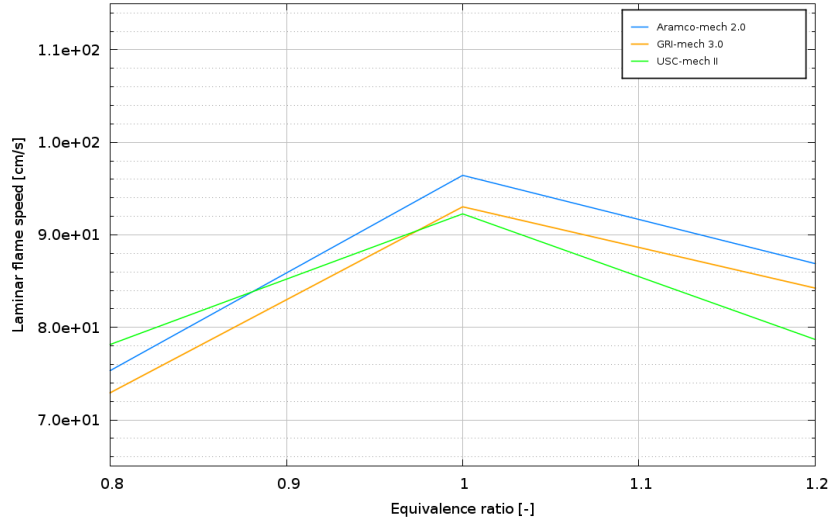


Figure 5.13: Laminar flame speed at spark conditions for o.p. 2000 [rpm] x 3.6 [bar] x lambda=1: 694 deg crank angle, $p = 7$ bar, $T = 700$ K

Laminar flame speed at engine conditions (o.p. 2000 [rpm] x 3.6 [bar] x lambda=1: 710 deg, p=10 bar, T=800 K)

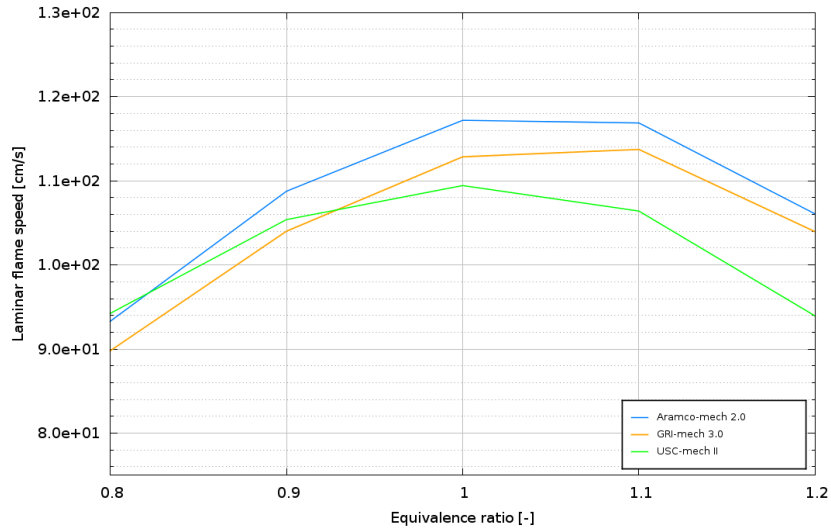


Figure 5.14: Laminar flame speed at engine conditions for o.p. 2000 [rpm] x 3.6 [bar] x lambda=1: 694 deg crank angle, $p = 10$ bar, $T = 800$ K

Laminar flame speed at engine conditions (o.p. 2000 [rpm] x 3.6 [bar] x lambda=1: 710 deg, p=10 bar, T=800 K)

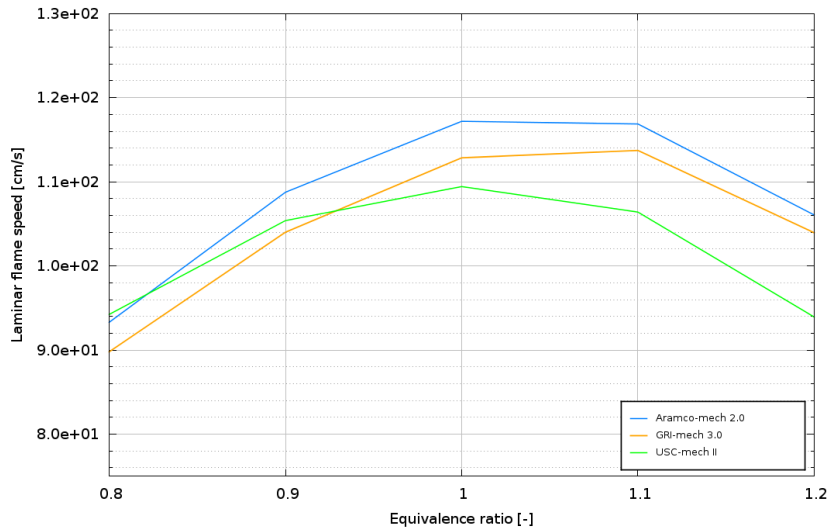


Figure 5.15: Laminar flame speed at peak pressure conditions for o.p. 2000 [rpm] x 3.6 [bar] x lambda=1: 734 deg crank angle, $p = 25$ bar, $T = 1900$ K

5.4.3 Mechanism reduction

Detailed mechanisms incorporate hundreds of chemical species and thousands of reactions, and so they turn out to be too computationally expensive to use in most simulations in which the complementary physical processes (such as heat and mass transfer or gas motion) are also embodied in the simulations. The computational time taken to obtain a numerical solution is typically $\propto N^2$ (N is the number of species) or $\propto n$ (n is the number of reactions).

To make the mechanism computationally efficient, the number of species and reactions must be reduced, in a way that maintains solution accuracy.

In CONVERGE, mechanism reduction can be carried out in two ways, namely

Dynamic reduction, or DMR, which reduces the mechanism *during* the SAGE simulation;

Skeletal mechanism reduction, which reduces the mechanism *prior* to executing a SAGE simulation, by running 0D auto-ignition cases in the Chemistry module.

Dynamic Mechanism Reduction (DMR)

This tool reduces the mechanism according to target weight and error propagation tolerance values that the user has to specify. Since it automatically removes species based on local thermo-chemical conditions, some species important to the simulation, such as soot precursors for emission modelling, might be lost.

The mechanisms that have been reduced through this approach are the *GRI-Mech 3.0* and the *USC-Mech II*.

For the *GRI-Mech 3.0* the species that have been specified as those that must not be removed are: O, O₂, H, H₂, OH, H₂O, H₂O₂, HNO, N, NNH, N₂O, NH, NH₃, NO, NO₂, N₂, CH₄, C₂H₂, CO, CH₂O, CO₂, Ar.

The C-0 species of the detailed mechanisms have been saved because they are important for ignition delay. The species C_2H_2 and CH_2O are important for low temperature ignition delay.

For the *USC-Mech II* the species that have been specified as those that must not be removed are: O, O_2 , H, H_2 , OH, H_2O , H_2O_2 , N_2 , CH_4 , C_2H_2 , CO, CH_2O , CO_2 , Ar. The C-0 species of the detailed mechanisms have been saved since they are important for ignition delay, but, differently from the *GRI-Mech 3.0*, species HNO, N, NNH, N_2O , NH, NH_2 , NH_3 , NO, NO_2 , N_2 are not present among the available species of the *USC-Mech II*. The species C_2H_2 and CH_2O are important for low temperature ignition delay.

Skeletal mechanism reduction

CONVERGE uses a basic skeletal mechanism reduction in which all species assumed unimportant, i.e. species with negligible impact over the conditions of interest, and their associated reactions are removed from the original detailed mechanism. The skeletal mechanism reduction is based on ignition delay error. The reduction process used in this thesis project follows the Directed Relation Graph approach with Error Propagation and Sensitivity Analysis (DRGEP-SA).

Lu and Law (2005) developed an automatic mechanism reduction procedure based on the theory of directed relation graph (DRG). Considering the simplified example in fig. 5.16, each vertex in a DRG represents a species in the detailed mechanism.

An edge from vertex A to vertex B exists only if the removal of species B would

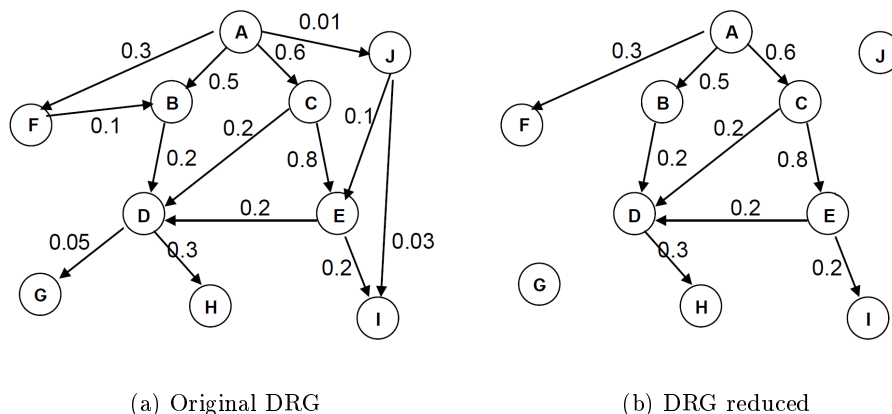


Figure 5.16: Simplified example of directed relation graph (DRG)

directly induce significant error to the production rate of species A. This effect is measured by the normalized contribution, r_{AB} , defined as:

$$r_{AB} = \frac{\sum_{i=1}^N |\nu_{A,i} \omega_i \delta_{Bi}|}{\sum_{i=1}^N |\nu_{A,i} \omega_i|} \quad (5.18)$$

where $\delta_{Bi} = 1$ if the i -th reaction involves species B, otherwise is 0, $\nu_{A,i}$ is the stoichiometric coefficient of species A in reaction i and ω_i is the net rate of a reversible reaction i . The net rate of a reversible reaction is the difference between the rates of the forward and the backward reactions.

The DRG starts as a set of species specified in `mech.dat`, where each species is represented by a stand-alone vertex. Then the DRG uses a user-defined threshold, ε , for the normalized contribution, $0 < \varepsilon < 1$. The DRG uses this threshold to determine which species are retained in the reduced mechanism. The DRG is developed by an

iterative procedure by maintaining connections and the corresponding species for which $r_{AB} > \varepsilon$.

In fig. 5.16 it is possible to see what happens if ε is set = 0.15: species G and J from the detailed mechanism depicted in fig. 5.16a get removed to reduce the mechanism to the mechanism shown in fig. 5.16b.

For what matters the Error Propagation and Sensitivity Analysis (DRGEP-SA), its algorithm (Raju et al., 2012) consists of two phases:

DRGEP, based on a different parameter to operate the species selection. Instead of using the r_{AB} values used in the DRG method, this approach considers the R_{AB} values. To define these, it is necessary to fix a set of *primary dependent species* for species A, consisting of those appearing explicitly in reactions involving A. If species B is not in the primary dependent set of A, then $r_{AB} = 0$. However, species C interacting with species A through species B is necessary for A only if it is necessary for B and B is necessary for A. This indirect coupling is quantified by a path-dependent coefficient, $r_{AB,i}$. This is the product of the normalized contributions along path i between species A and B. The influence of species B on species A is characterized by coefficient R_{AB} , which is the maximum of the path-dependent coefficients:

$$r_{AB,i} = \prod_{XY \in i} r_{XY} \quad (5.19)$$

$$R_{AB} = \max r_{AB,i} \quad (5.20)$$

Sensitivity Analysis (SA), which is performed to further reduce the size of the mechanism, after the optimal mechanism is obtained from the DRGEP step. The overall interaction coefficients of the species in the skeletal mechanism are arranged in ascending order and a fixed fraction of the species from the top of the list is chosen for sensitivity analysis. This list of species is the *limbo species*. The error induced by each of the species is calculated by removing this species from the DRGEP-generated skeletal mechanism. The error in the ignition delay is then calculated for the resulting skeletal mechanism and is an indication of the sensitivity of the species to the prediction of ignition delay time. Now the species are arranged in increasing order with respect to this error. Then, the optimal skeletal mechanism is determined from the sensitivity analysis, which is acted by removing the species identified from the top of the list one by one from the DRGEP generated mechanism until the error generated is less than the user-defined tolerance for ignition delay. Thus the optimal skeletal mechanism is finally obtained.

The mechanism that has been reduced through this approach is the *GRI-Mech 3.0*, since, as will be shown in the next chapter, is the one that gave the best results in most of the engine simulation, so good results after the reduction are still expected. Skeletal mechanism validation for ignition delay and laminar flame speed has also been carried out, in order to check the goodness of the reduction done.

Table 5.3: GRI-mech 3.0: Summary about skeletal reduction

	<i>GRI-Mech 3.0</i>	<i>Reduced GRI-Mech 3.0</i>
Number of available elements:	5	5
Number of available species:	53	35
Number of available reactions:	325	196

More in detail, for the original *GRI-Mech 3.0*:

Available elements: O, H, C, N, AR;

Available species: H₂, H, O, O₂, OH, H₂O, HO₂, H₂O₂, C, CH, CH₂, CH₂(S), CH₃, CH₄, CO, CO₂, HCO, CH₂O, CH₂OH, CH₃O, CH₃OH, C₂H, C₂H₂, C₂H₃, C₂H₄, C₂H₅, C₂H₆, HCCO, CH₂CO, HCCOH, N, NH, NH₂, NH₃, NNH, NO, NO₂, N₂O, HNO, CN, HCN, H₂CN, HCNN, HCNO, HOCN, HNCO, NCO, N₂, AR, C₃H₇, C₃H₈, CH₂CHO, CH₃CHO.

While, for the *Reduced GRI-Mech 3.0*:

Available elements: O, H, C, N, AR;

Available species: H₂, H, O, O₂, OH, H₂O, HO₂, H₂O₂, C, CH, CH₂, CH₂(S), CH₃, CH₄, CO, CO₂, HCO, CH₂O, CH₂OH, CH₃O, C₂H₆, N, NH, NH₂, NH₃, NNH, NO, NO₂, N₂O, HNO, HCN, HCNO, HNCO, NCO, N₂.

Also in this case the species that have been specified as those that must not be removed are the C-0 species of the detailed mechanisms have been saved because they are important for ignition delay, and the species CH₂O, which is important for low temperature ignition delay.

Reduced GRI-Mech 3.0 validation: Ignition delay

Figure 5.17 shows that the *GRI-Mech 3.0* did not lose accuracy after the skeletal reduction, as the simulation results provided by the *Reduced GRI-Mech 3.0* follow the experimental data and are not very different to those provided by the detailed *GRI-Mech 3.0*.

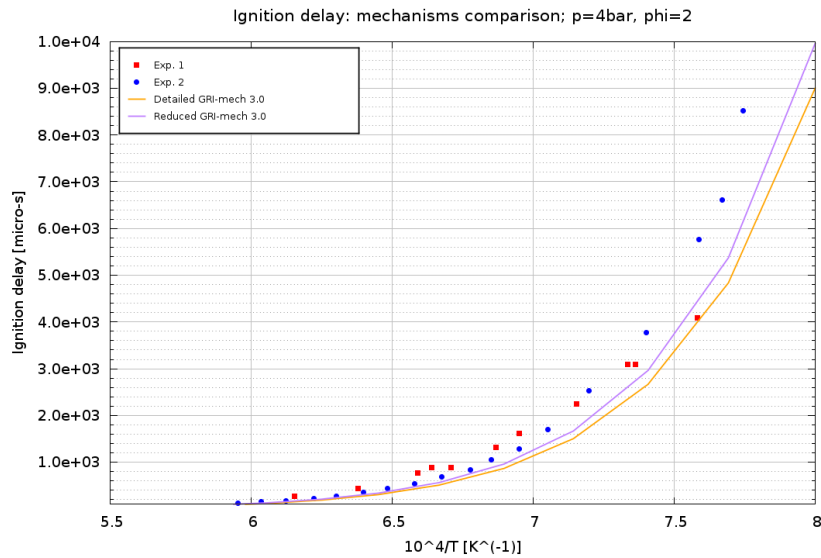


Figure 5.17: Detailed GRI-Mech 3.0 vs Reduced GRI-Mech 3.0: Ignition delay for $p = 0.4\text{MPa}$, $\phi = 2$

Also in case of *Reduced GRI-Mech 3.0*, ignition delay (Zero-Dimensional) simulations at engine conditions have been carried out, in order to check that the skeletal reduction is suitable also for the applications that will be shown in next chapter. Figure 5.18 shows that the *Reduced GRI-Mech 3.0* is different from the detailed *GRI-Mech 3.0*, but reasonably. For $T = 700\text{K}$ the two mechanisms do not provide too different

results.

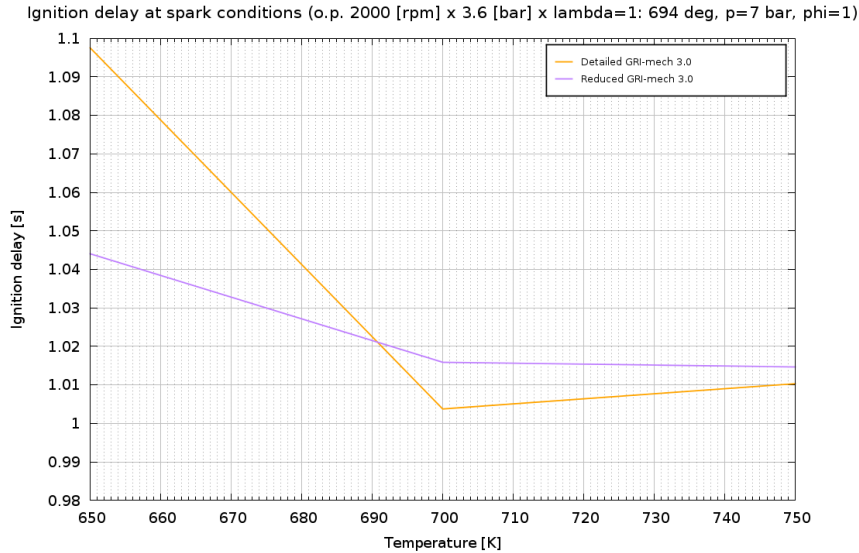


Figure 5.18: Detailed GRI-Mech 3.0 vs Reduced GRI-Mech 3.0: Ignition delay at spark conditions for o.p. 2000 [rpm] x 3.6 [bar] x lambda=1: 694 deg crank angle, $p = 7$ bar, $\phi = 1$ [-]

Reduced GRI-Mech 3.0 validation: Laminar flame speed

To check whether the skeletal reduction is not too different from the detailed one and suitable also for the engine applications, laminar flame speed (One-Dimensional) simulations with *Reduced GRI-Mech 3.0* at engine conditions have been carried out. Figures 5.19, 5.20, 5.21, 5.22, 5.23, 5.24 show that the *Reduced GRI-Mech 3.0* and the detailed *GRI-Mech 3.0* have a similar trend, with small differences. *Reduced GRI-Mech 3.0* results are sufficiently conform to the experimental data.

For $p = 20$ bar the *Reduced GRI-Mech 3.0* provides laminar flame speeds a little overestimated with regards to the experimental data and the simulation results provided by the detailed *GRI-Mech 3.0*.

Also for laminar flame speed, One-Dimensional simulations with *Reduced GRI-Mech 3.0* at engine conditions have been carried out.

Figure 5.25 shows that results provided by *Reduced GRI-Mech 3.0*, after $\phi = 1$, become more different from those of the detailed *GRI-Mech 3.0*, but reasonably. For $\phi = 1$ the two mechanisms provide very similar results.

Figure 5.26 shows the results of the two mechanisms turn out to be very similar.

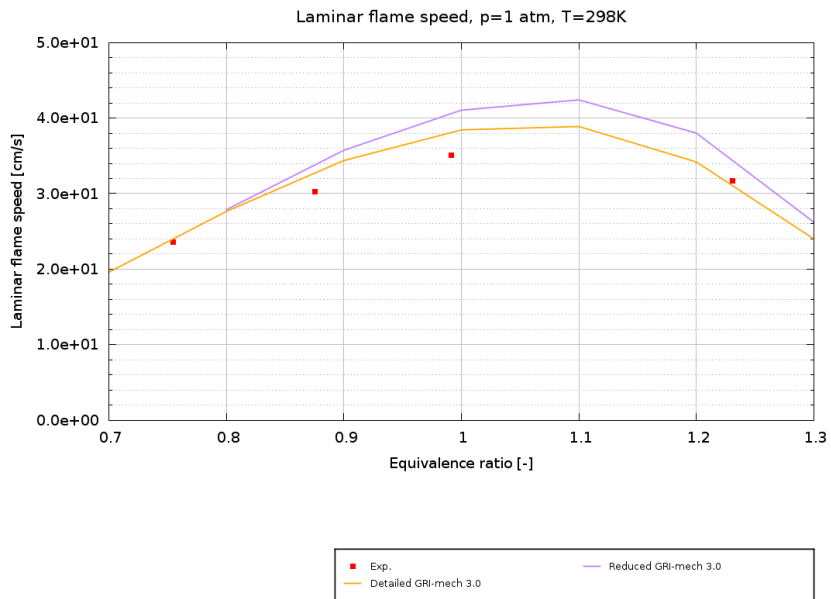


Figure 5.19: Detailed GRI-Mech 3.0 vs Reduced GRI-Mech 3.0: Laminar flame speed for pure CH_4 , $p = 1$ bar, $T = 298$ K

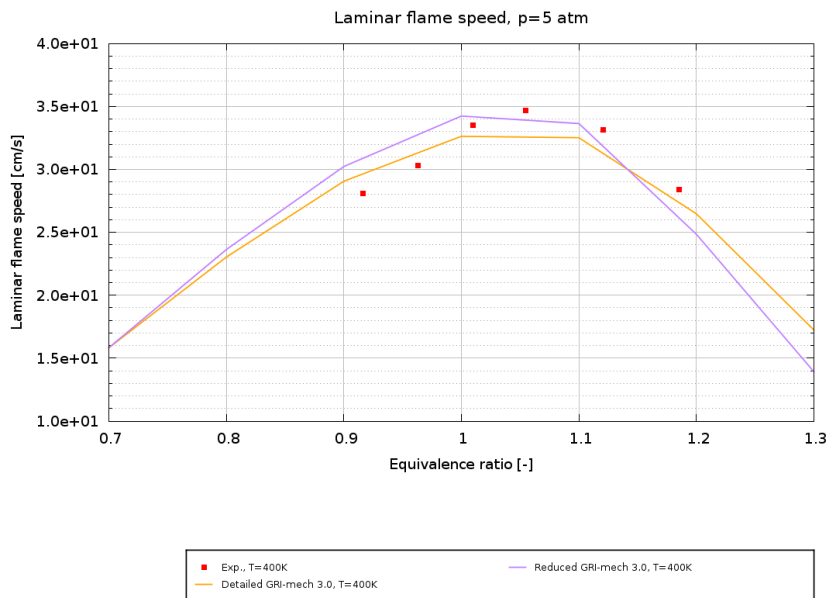


Figure 5.20: Detailed GRI-Mech 3.0 vs Reduced GRI-Mech 3.0: Laminar flame speed for pure CH_4 , $p = 5$ bar, $T = 400$ K

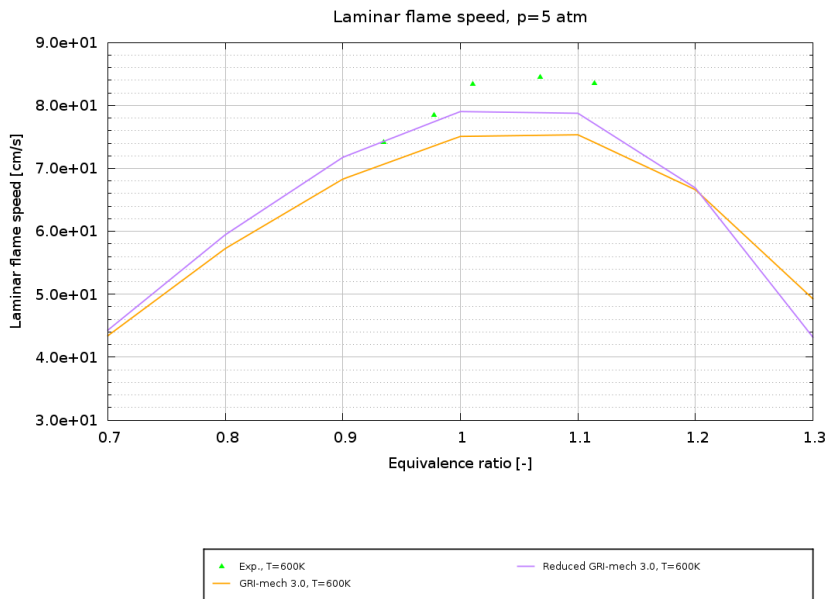


Figure 5.21: Detailed GRI-Mech 3.0 vs Reduced GRI-Mech 3.0: Laminar flame speed for pure CH_4 , $p = 5\text{bar}$, $T = 500K$

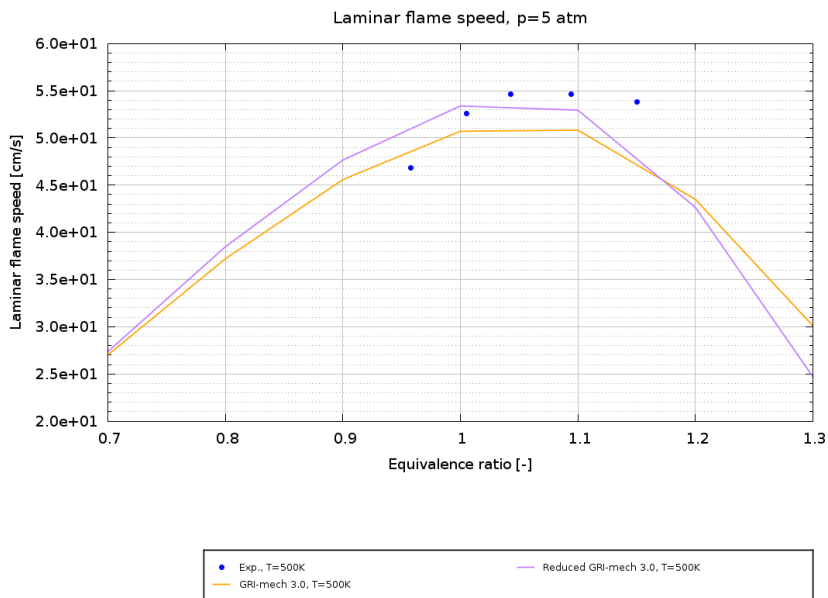


Figure 5.22: Detailed GRI-Mech 3.0 vs Reduced GRI-Mech 3.0: Laminar flame speed for pure CH_4 , $p = 5\text{bar}$, $T = 600K$

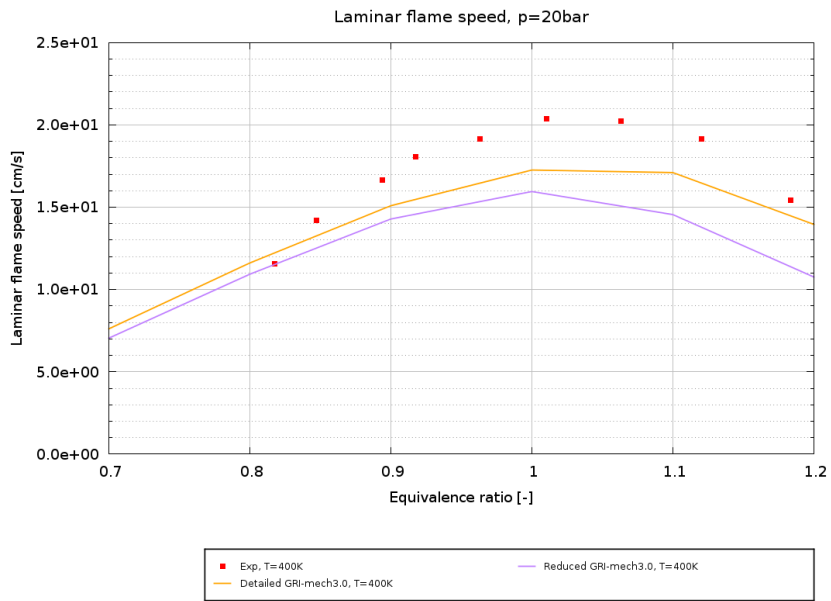


Figure 5.23: Detailed GRI-Mech 3.0 vs Reduced GRI-Mech 3.0: Laminar flame speed for pure CH_4 , $p = 20\text{bar}$, $T = 400\text{K}$

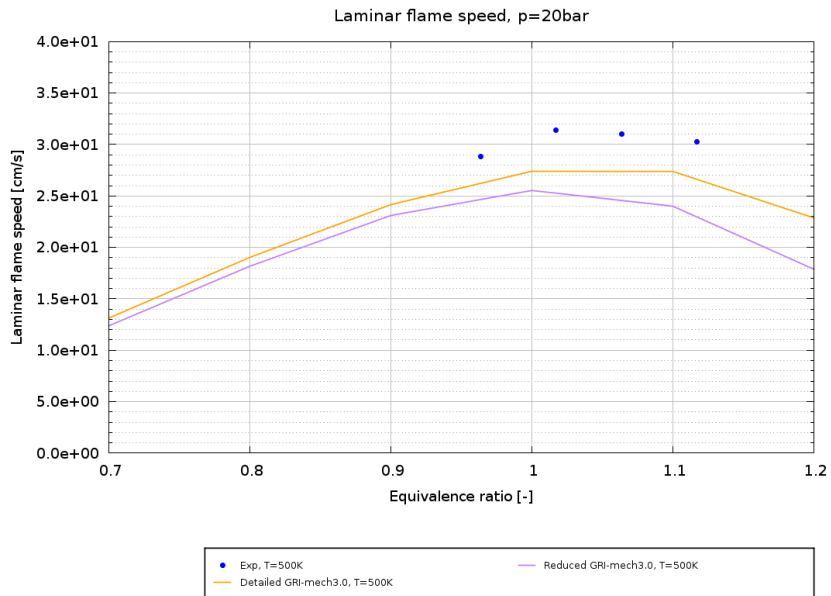


Figure 5.24: Detailed GRI-Mech 3.0 vs Reduced GRI-Mech 3.0: Laminar flame speed for pure CH_4 , $p = 20\text{bar}$, $T = 500\text{K}$

Laminar flame speed at spark conditions (o.p. 2000 [rpm] x 3.6 [bar] x lambda=1: 694 deg, p=7 bar, T=700 K)

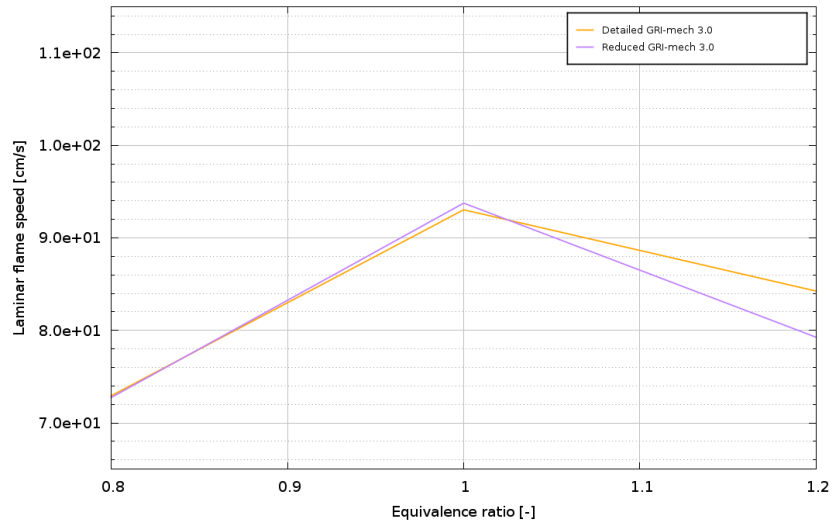


Figure 5.25: Detailed GRI-Mech 3.0 vs Reduced GRI-Mech 3.0: Laminar flame speed at spark conditions for o.p. 2000 [rpm] x 3.6 [bar] x lambda=1: 694 deg crank angle, $p = 7$ bar, $T = 700$ K

Laminar flame speed at peak pressure cond. (o.p. 2000 [rpm] x 3.6 [bar] x lambda=1: 734 deg, p=25 bar, T=1900 K)

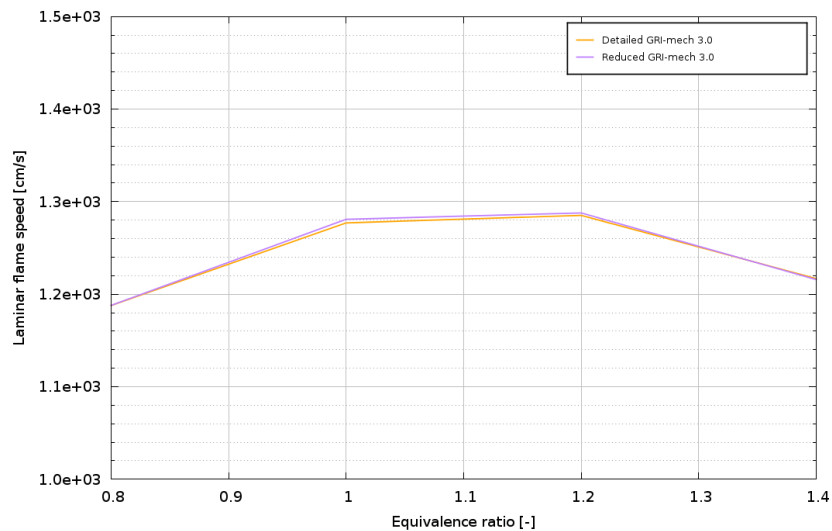


Figure 5.26: Detailed GRI-Mech 3.0 vs Reduced GRI-Mech 3.0: Laminar flame speed at peak pressure conditions for o.p. 2000 [rpm] x 3.6 [bar] x lambda=1: 734 deg crank angle, $p = 25$ bar, $T = 1900$ K

Results and conclusions

6.1 Introduction

In this chapter, the results regarding the engine simulations carried out in CONVERGE will be shown, as well as their comparison with experimental data, and the validation of the model by changing some parameters, for both the fuel models developed, for the the several kinetic mechanisms used.

In particular, the model validation has been carried out by comparing:

Pressure in cylinder 1, i.e. p for model "closest cycle" and experimental "closest cycle", which are, as previously introduced, the model and the experimental cycle whose pressure profile is the closest to the experimental ensemble average;

Heat release rate in cylinder 1, i.e. HRR , for model "closest cycle" and experimental "closest cycle", whose calculation has been dealt with in chapter "NG-Engine: experimental data". It takes into account also the trapped mass in the chamber. The calculation procedure of this variable for both simulated and experimental is consistent;

Integrated heat release in cylinder 1, i.e. IHR , for model "closest cycle" and experimental "closest cycle", whose computation procedure has been dealt with in chapter "NG-Engine: experimental data". It takes into account also the trapped mass in the chamber. The calculation procedure of this variable for both simulated and experimental is consistent.

6.2 O.P. 2000[rpm] x 3.6[bar] x lambda=1

For what matters the engine operating point 2000[rpm] x 3.6 [bar] x lambda=1, the simulations in CONVERGE have been carried out for the two fuels, i.e. *Pure CH₄* and *Actual Fuel Composition*, for all the three mesh settings, i.e. *Coarse*, *Fine* and *Finest*, and for all the kinetic mechanisms, i.e. *GRI-Mech 3.0*, *USC-Mech II*, *AramcoMech 2.0*, introduced in the previous chapters, ad well as the Skeletal Reduction of mechanism *GRI-Mech 3.0*, i.e. *Reduced GRI-Mech 3.0*, and the and Dynamic reduction of mechanisms *GRI-Mech 3.0* and *USC-Mech II*, namely *GRI-Mech 3.0 (DMR)* *USC-Mech II (DMR)*.

Table 6.1 summarizes the cases that have been run.

Table 6.1: O.P. 2000[rpm] x 3.6 [bar] x lambda=1: simulations cases run

Combustion model	Fuel	Mechanism	Mesh settings
SAGE	Pure CH ₄	<i>GRI-Mech 3.0</i>	Coarse
			Fine
			Finest
		<i>USC-Mech II</i>	Coarse
			Fine
			Finest
		<i>AramcoMech 2.0</i>	Coarse
			Fine
			Finest
		<i>Reduced GRI-Mech 3.0</i>	Coarse
			Fine
			Finest
		<i>GRI-Mech 3.0 (DMR)</i>	Fine
		<i>USC-Mech II (DMR)</i>	Fine
	Actual fuel	<i>GRI-Mech 3.0</i>	Coarse
			Fine
			Finest
		<i>USC-Mech II</i>	Coarse
			Fine
		<i>AramcoMech 2.0</i>	Coarse
			Fine
<i>Reduced GRI-Mech 3.0</i>		Coarse	
		Fine	
<i>GRI-Mech 3.0 (DMR)</i>		Fine	

6.2.1 Pure CH₄

At first, CONVERGE engine simulations have been run for the *Coarse* mesh settings and compared with the experimental data. Results have been quite satisfying, but, in order to get an even higher affinity with the experimental data available, the *Finest* mesh settings cases have been run. As it will be shown, the results obtained with this mesh settings have not been satisfying; the reasons of this have been investigated, and will be shown in the paragraphs below. Therefore, the *Fine* mesh settings have been set and run.

Notice that the pressure profiles obtained have been divided and overlapped.

Coarse mesh settings

Figure 6.1 shows a comparison between the results obtained with the simulation SAGE-*GRI-Mech 3.0* and the experimental data in the matter of the Pressure in cylinder 1. The image is focused on the range between 650÷800 crank angle degree. With the exception of the first cycle, which is usually not take into account in the analysis of the simulations results, the mechanism provides good results with this

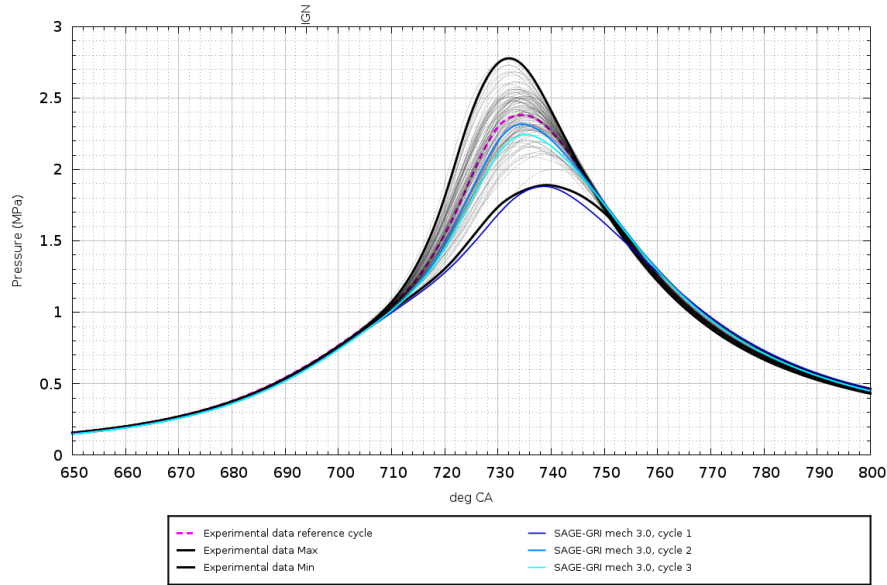


Figure 6.1: Pressure in cylinder 1: SAGE-*GRI-Mech 3.0* and experimental data, Coarse mesh settings, Pure CH₄

mesh settings: the pressure profiles of the cycles lie inside the range described by the experimental pressure profiles characterized by the maximum and the minimum peaks, and both are very close to the experimental reference cycle, especially the second simulation cycle.

The pressure at the *SA*, i.e. the value of pressure in cylinder 1 corresponding to 694 crank angle degree, is about 0.6 MPa, for both experimental data and simulation result.

The simulation crank angle degree corresponding to the peak pressure in cylinder 1, i.e. θ_{peak} is about 733 deg (considering the model cycle whose pressure profile is the closest to the experimental ensemble average), while the experimental one (considering the experimental reference cycle) happens to be about 734 deg.

The simulation peak pressure value, i.e. p_{peak} is about 2.3 MPa (always taking into account the model cycle whose pressure profile is the closest to the experimental ensemble average) while the experimental one (considering the experimental reference cycle) is about 2.4 MPa.

The runtime of this simulation has been 34.67 hours per cycle, using 3 nodes corresponding to 12 cores.

Figures 6.2 and 6.3 respectively show the Heat release rate and the Integrated Heat release plot for both simulation results obtained with SAGE-*GRI-Mech 3.0* and experimental data.

The simulation cycle that has been considered for the HR calculations is the one whose pressure profile is the closest to the experimental ensemble average; this will be the same approach for all the other cases.

The images, as well the calculations of the *HRR* and *IHR*, are focused on the range in which the system is closed.

Both the figures show that the *HRR* and *IHR* of the model are similar to the experimental ones, but with little differences in the range corresponding to crank angle 740÷790.

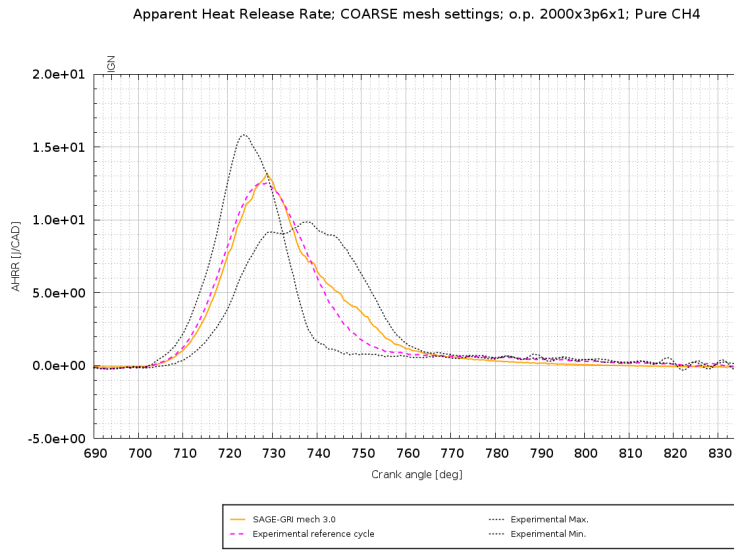


Figure 6.2: Heat release rate (HRR): SAGE-*GRI-Mech 3.0* and experimental data, Coarse mesh settings, Pure CH₄

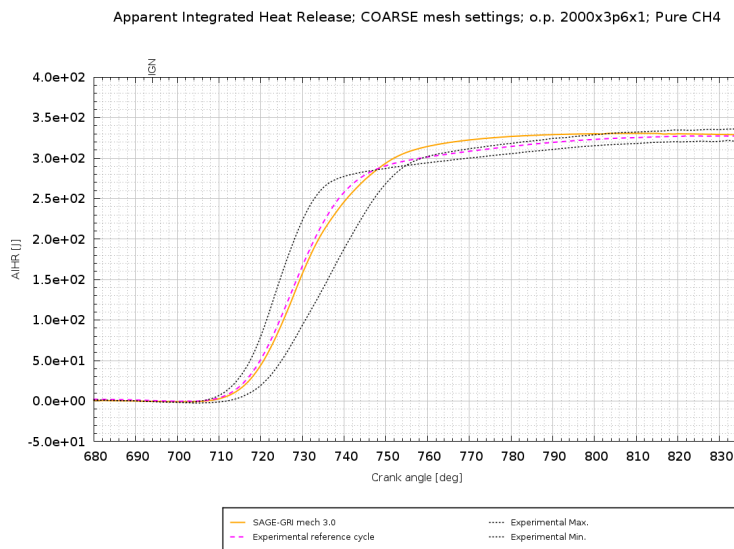


Figure 6.3: Integrated Heat release (IHR): SAGE-*GRI-Mech 3.0* and experimental data, Coarse mesh settings, Pure CH₄

Figure 6.4 shows the comparison between the results obtained with the simulation SAGE-*USC-Mech II* and the experimental data in the matter of the Pressure in cylinder 1. The image is focused on the range between 650÷800 crank angle degree. With the exception of the second simulation cycle, all the pressure profiles of the cycles lie outside the range described by the experimental pressure profiles characterized by the maximum and the minimum peaks. The second simulation cycle is characterized by a pressure profile which is the closest to the experimental reference cycle, but still quite far. Therefore, the mechanism does not perform particularly good with this mesh settings.

The pressure at the SA, i.e. the value of pressure in cylinder 1 corresponding to 694 crank angle degree, is about 0.6 MPa, for both experimental data and simulation result.

SAGE-USC mech II and exp. data comparison; COARSE mesh settings; o.p. 2000x3p6x1; Pure CH₄

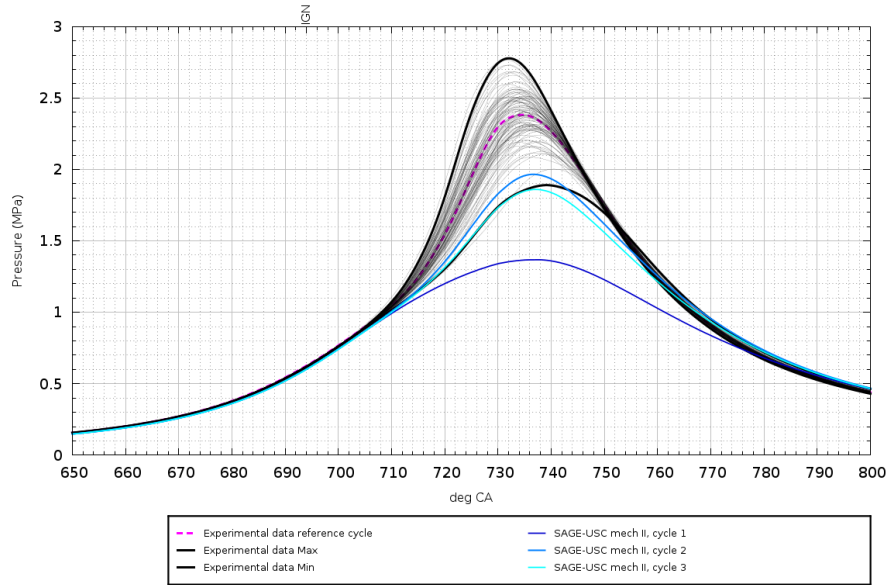


Figure 6.4: Pressure in cylinder 1: SAGE-USC-Mech II and experimental data, Coarse mesh settings, Pure CH₄

The simulation crank angle degree corresponding to the peak pressure in cylinder 1, i.e. θ_{peak} is about 736 deg (considering the model cycle whose pressure profile is the closest to the experimental ensemble average), while the experimental one (considering the experimental reference cycle) happens to be about 734 deg.

The simulation peak pressure value, i.e. p_{peak} is about 1.96 MPa (always taking into account the model cycle whose pressure profile is the closest to the experimental ensemble average) while the experimental one (considering the experimental reference cycle) is about 2.4 MPa.

The runtime of this simulation has been 50.55 hours per cycle, using 3 nodes corresponding to 12 cores.

Figures 6.5 and 6.6 respectively show the Heat release rate and the Integrated Heat release plot for both simulation results obtained with SAGE-USC-Mech II and experimental data.

The images, as well the calculations of the HRR and IHR , are focused on the range in which the system is closed.

As it can be noticed, there is a quite remarkable difference between experimental and model HRR and IHR ; in fact, the pressure profile of the model cycle considered for the HR calculation (fig 6.4) is quite far from the experimental reference cycle.

Figure 6.7 shows the comparison between the results obtained with the simulation SAGE-AramcoMech 2.0 and the experimental data in the matter of the Pressure in cylinder 1. The image is focused on the range between 650÷800 crank angle degree. All the pressure profiles of the simulation cycles lie outside the range described by the experimental pressure profiles characterized by the maximum and the minimum peaks. Therefore, the mechanism does not perform particularly good with this mesh settings.

The pressure at the SA, i.e. the value of pressure in cylinder 1 corresponding to 694 crank angle degree, is about 0.6 MPa, for both experimental data and simulation result.

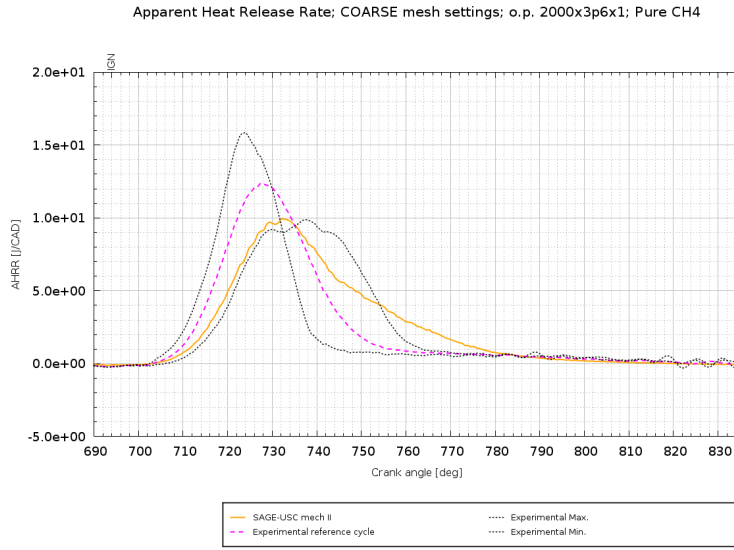


Figure 6.5: Heat release rate (HRR): SAGE-USC-Mech II and experimental data, Coarse mesh settings, Pure CH₄

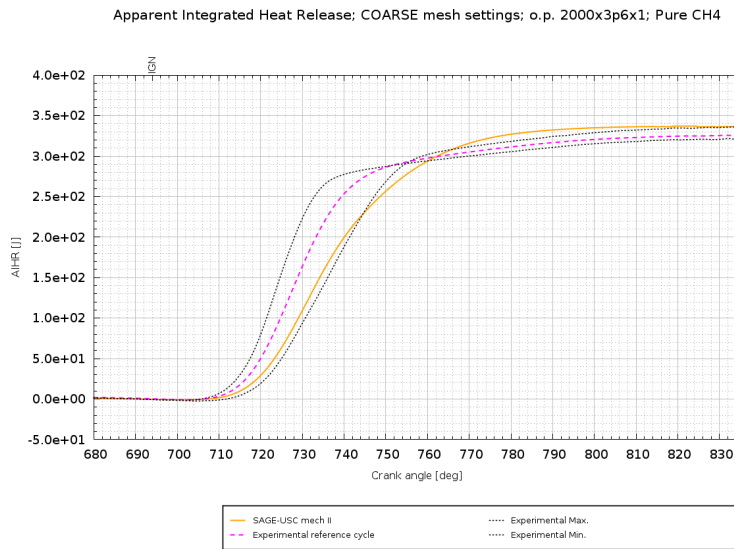


Figure 6.6: Integrated Heat release (IHR): SAGE-USC-Mech II and experimental data, Coarse mesh settings, Pure CH₄

The simulation crank angle degree corresponding to the peak pressure in cylinder 1, i.e. θ_{peak} is about 736 deg (considering the model cycle whose pressure profile is the closest to the experimental ensemble average), while the experimental one (considering the experimental reference cycle) happens to be about 734 deg.

The simulation peak pressure value, i.e. p_{peak} is about 1.8 MPa (always taking into account the model cycle whose pressure profile is the closest to the experimental ensemble average) while the experimental one (considering the experimental reference cycle) is about 2.4 MPa.

The runtime of this simulation has been 64.33 hours per cycle, using 3 nodes corresponding to 12 cores.

Figures 6.8 and 6.9 respectively show the Heat release rate and the Integrated Heat

SAGE-Aramco mech 2.0 and exp. data comparison; COARSE mesh settings; o.p. 2000x3p6x1; Pure CH₄

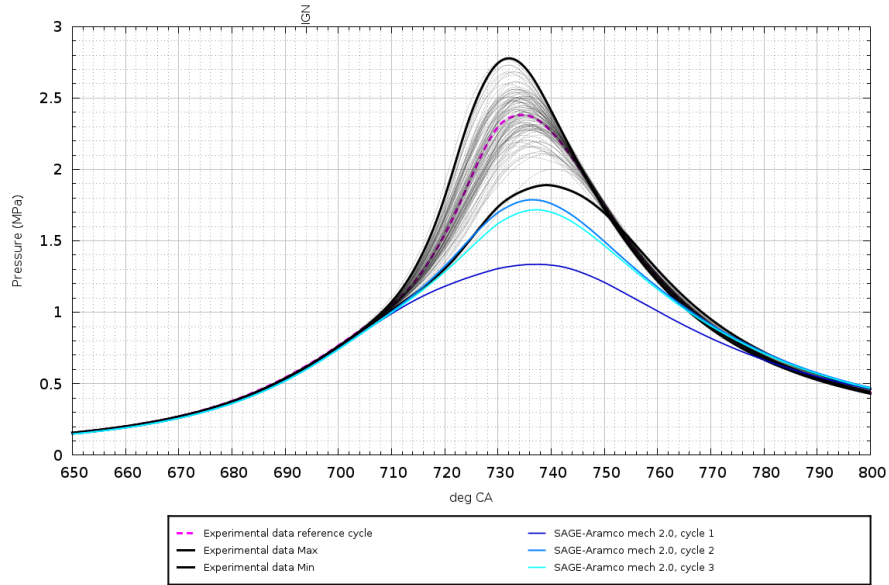


Figure 6.7: Pressure in cylinder 1: SAGE-AramcoMech2.0 and experimental data, Coarse mesh settings, Pure CH₄

Apparent Heat Release Rate; COARSE mesh settings; o.p. 2000x3p6x1; Pure CH₄

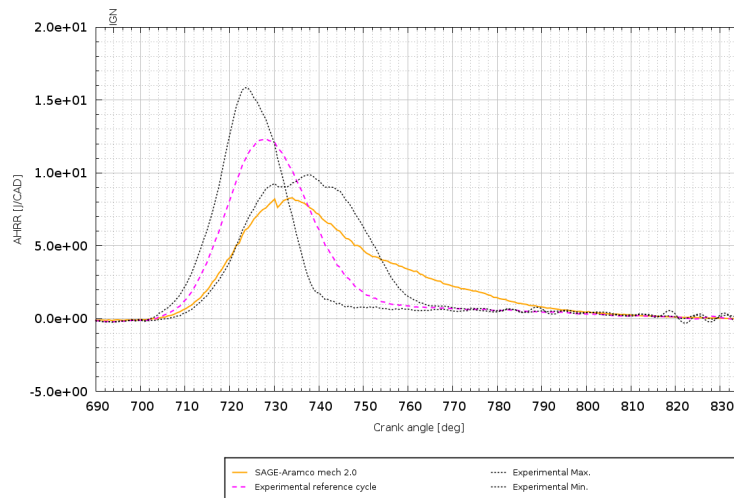


Figure 6.8: Heat release rate (HRR): SAGE-Aramco-Mech2.0 and experimental data, Coarse mesh settings, Pure CH₄

release plot for both simulation results obtained with SAGE-Aramco-Mech2.0 and experimental data.

The images, as well the calculations of the *HRR* and *IHR*, are focused on the range in which the system is closed.

Experimental and model *HRR* and *IHR* are definitely different, as the simulation results do not lie between the two experimental limit curves (i.e. the curves related to the experimental pressure profiles whose peaks are the maximum and the minimum ones). In fact, the pressure profile of the model cycle considered for the HR calculation (fig 6.7) is far from the experimental reference cycle, and out of the aforementioned

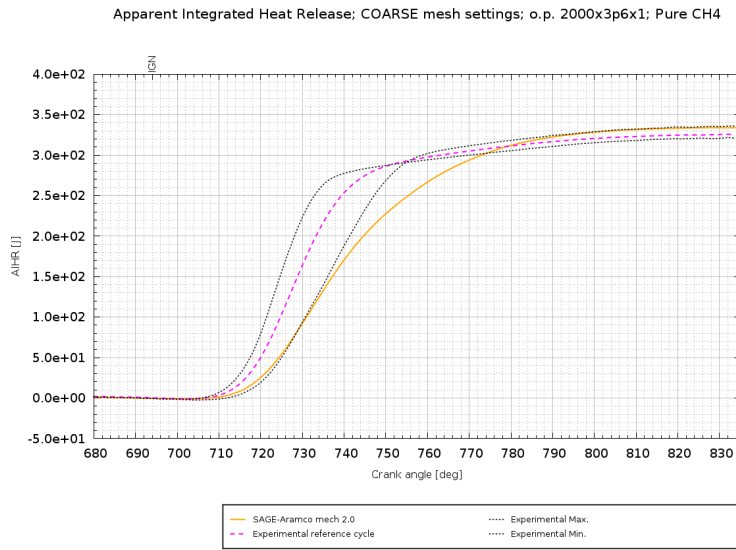


Figure 6.9: Integrated Heat release (IHR): SAGE-Aramco-Mech2.0 and experimental data, Coarse mesh settings, Pure CH₄

range.

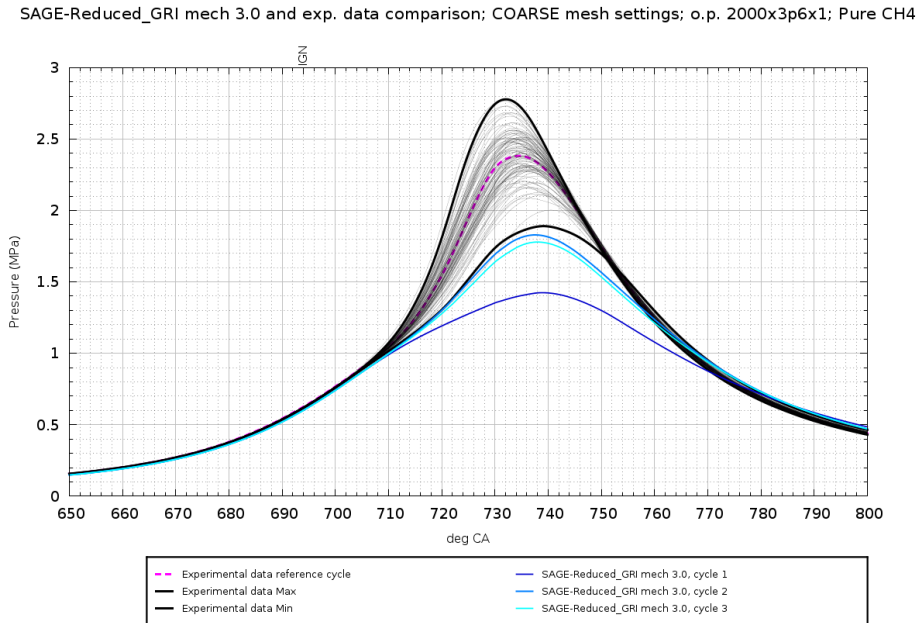


Figure 6.10: Pressure in cylinder 1: SAGE-Reduced GRI-Mech 3.0 and experimental data, Coarse mesh settings, Pure CH₄

Figure 6.10 shows the comparison between the results obtained with the simulation SAGE-Reduced GRI-Mech 3.0 and the experimental data in the matter of the Pressure in cylinder 1. The image is focused on the range between 650÷800 crank angle degree.

All the pressure profiles of the simulation cycles lie outside the range described by the experimental pressure profiles characterized by the maximum and the minimum

peaks. Therefore, the mechanism does not perform particularly good with this mesh settings.

The pressure at the *SA*, i.e. the value of pressure in cylinder 1 corresponding to 694 crank angle degree, is about 0.6 MPa, for both experimental data and simulation result.

The simulation crank angle degree corresponding to the peak pressure in cylinder 1, i.e. θ_{peak} is about 737 deg (considering the model cycle whose pressure profile is the closest to the experimental ensemble average), while the experimental one (considering the experimental reference cycle) happens to be about 734 deg.

The simulation peak pressure value, i.e. p_{peak} is about 1.8 MPa (always taking into account the model cycle whose pressure profile is the closest to the experimental ensemble average) while the experimental one (considering the experimental reference cycle) is about 2.4 MPa.

The runtime of this simulation has been 29.95 hours per cycle, using 3 nodes corresponding to 12 cores.

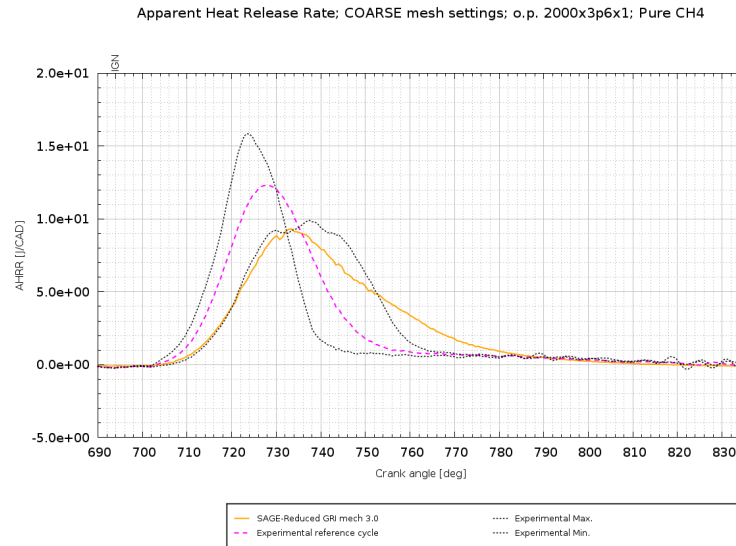


Figure 6.11: Heat release rate (HRR): *SAGE-Reduced GRI-Mech 3.0* and experimental data, Coarse mesh settings, Pure CH_4

Figures 6.11 and 6.12 respectively show the Heat release rate and the Integrated Heat release plot for both simulation results obtained with *SAGE-Reduced GRI-Mech 3.0* and experimental data.

The images, as well the calculations of the *HRR* and *IHR*, are focused on the range in which the system is closed.

The *HRR* and *IHR* of the simulation are not very conform to the experimental reference cycle ones, and they even do not lie between the two experimental limit curves. In fact, the pressure profile of the model cycle considered for the HR calculation (fig 6.10) is quite far from the experimental reference cycle.

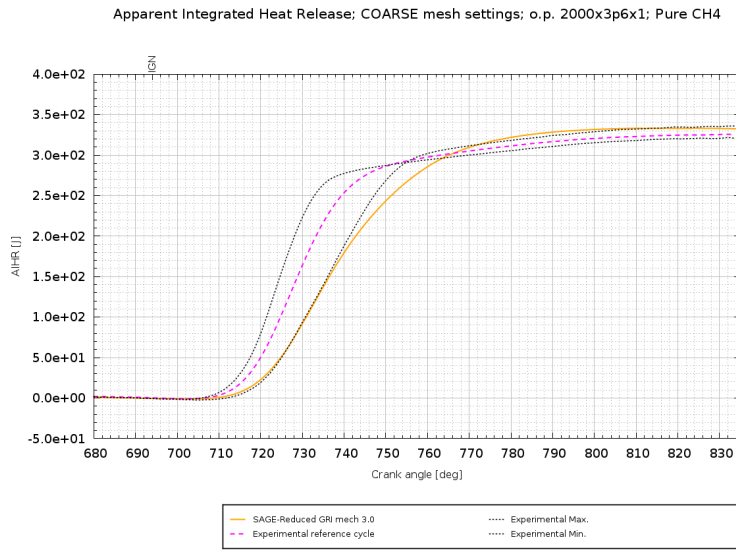


Figure 6.12: Integrated Heat release (IHR): SAGE-*Reduced GRI-Mech 3.0* and experimental data, Coarse mesh settings, Pure CH₄

Finest mesh settings

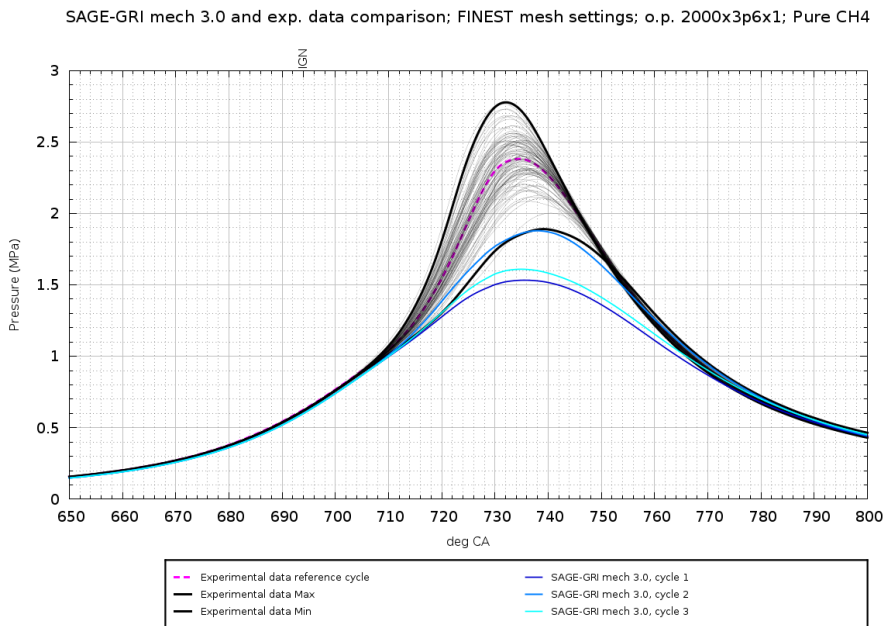


Figure 6.13: Pressure in cylinder 1: SAGE-*GRI-Mech 3.0* and experimental data, Finest mesh settings, Pure CH₄

Figure 6.13 shows a comparison between the results obtained with the simulation SAGE-*GRI-Mech 3.0* and the experimental data in the matter of the Pressure in cylinder 1. The image is focused on the range between 650÷800 crank angle degree. The mechanism does not provide good results with this mesh settings, as with the exception of the second cycle (still quite far from the experimental reference cycle), the pressure profiles of the cycles lie inside the range described by the experimental pressure profiles characterized by the maximum and the minimum peaks, and both

are very close to the experimental reference cycle.

The pressure at the *SA*, i.e. the value of pressure in cylinder 1 corresponding to 694 crank angle degree, is about 0.6 MPa, for both experimental data and simulation result.

The simulation crank angle degree corresponding to the peak pressure in cylinder 1, i.e. θ_{peak} is about 739 deg (considering the model cycle whose pressure profile is the closest to the experimental ensemble average), while the experimental one (considering the experimental reference cycle) happens to be about 734 deg.

The simulation peak pressure value, i.e. p_{peak} is about 1.9 MPa (always taking into account the model cycle whose pressure profile is the closest to the experimental ensemble average) while the experimental one (considering the experimental reference cycle) is about 2.4 MPa.

The runtime of this simulation has been 61.33 hours per cycle, using 3 nodes corresponding to 12 cores.

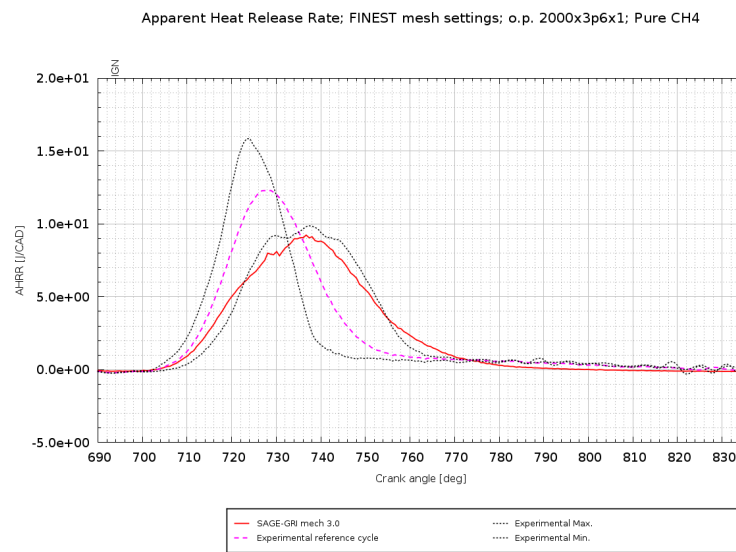


Figure 6.14: Heat release rate (HRR): SAGE-*GRI-Mech 3.0* and experimental data, Finest mesh settings, Pure CH₄

Figures 6.14 and 6.15 respectively show the Heat release rate and the Integrated Heat release plot for both simulation results obtained with SAGE-*GRI-Mech 3.0* and experimental data.

As expected from Fig. 6.13, the results are far from the experimental values of Heat release.

Figure 6.16 shows the comparison between the results obtained with the simulation SAGE-*USC-Mech II* and the experimental data in the matter of the Pressure in cylinder 1. The image is focused on the range between 650÷800 crank angle degree.

All the pressure profiles of the cycles lie outside the range described by the experimental pressure profiles characterized by the maximum and the minimum peaks. The third simulation cycle is characterized by a pressure profile which is the closest to the experimental reference cycle, but still quite far. Therefore, the mechanism does not perform particularly good with this mesh settings.

The pressure at the *SA*, i.e. the value of pressure in cylinder 1 corresponding to 694 crank angle degree, is about 0.6 MPa, for both experimental data and simulation result.

The simulation crank angle degree corresponding to the peak pressure in cylinder 1, i.e. θ_{peak} is about 732 deg (considering the model cycle whose pressure profile is the

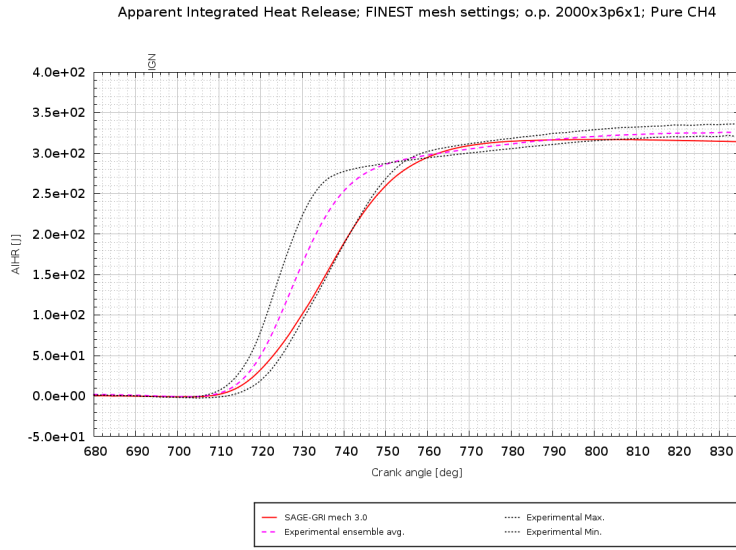


Figure 6.15: Integrated Heat release (IHR): SAGE-*GRI-Mech 3.0* and experimental data, Finest mesh settings, Pure CH₄

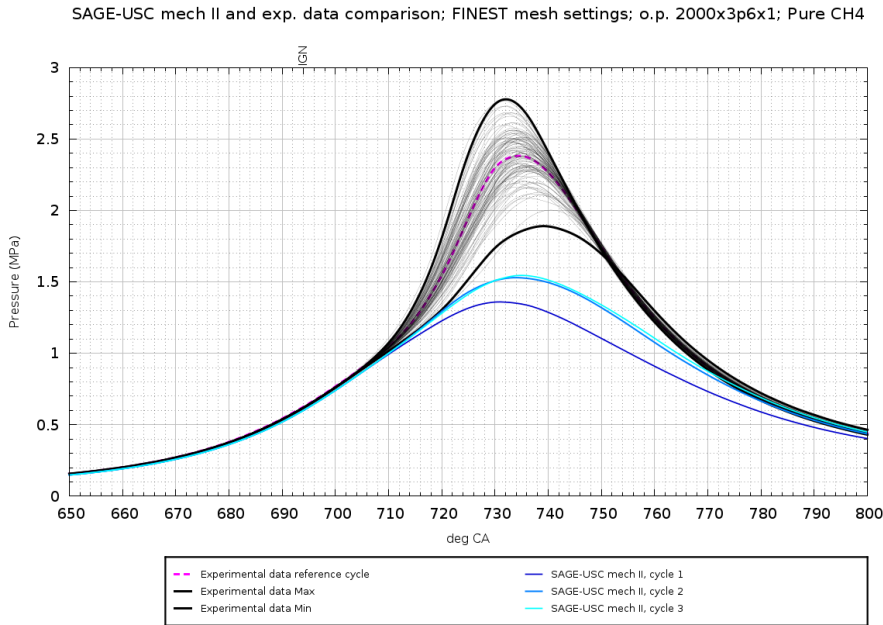


Figure 6.16: Pressure in cylinder 1: SAGE-*USC-Mech II* and experimental data, Finest mesh settings, Pure CH₄

closest to the experimental ensemble average), while the experimental one (considering the experimental reference cycle) happens to be about 734 deg.

The simulation peak pressure value, i.e. p_{peak} is about 1.55 MPa (always taking into account the third cycle) while the one of the experimental reference cycle is about 2.4 MPa.

This simulation needed a lot of restarts because of memory usage problems, and its runtime of this simulation has been 73 hours per cycle, using 5 nodes and 30 cores. A higher number of cores has been used to figure out the aforementioned problems.

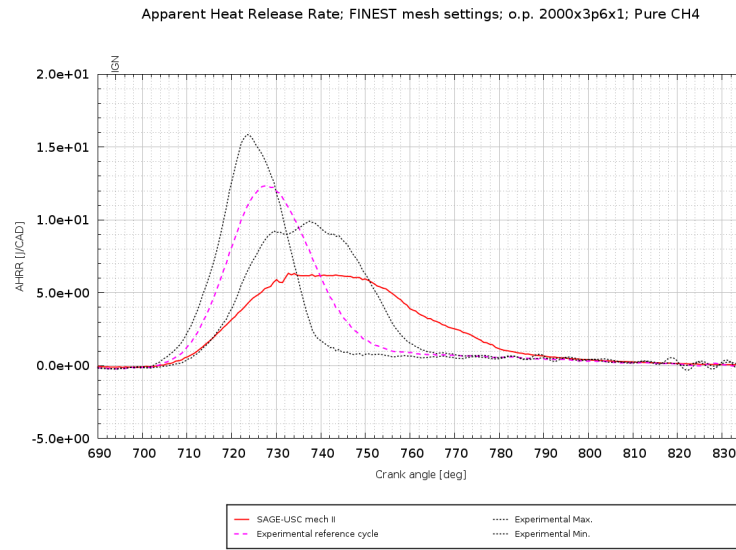


Figure 6.17: Heat release rate (HRR): SAGE-*USC-Mech II* and experimental data, Finest mesh settings, Pure CH₄

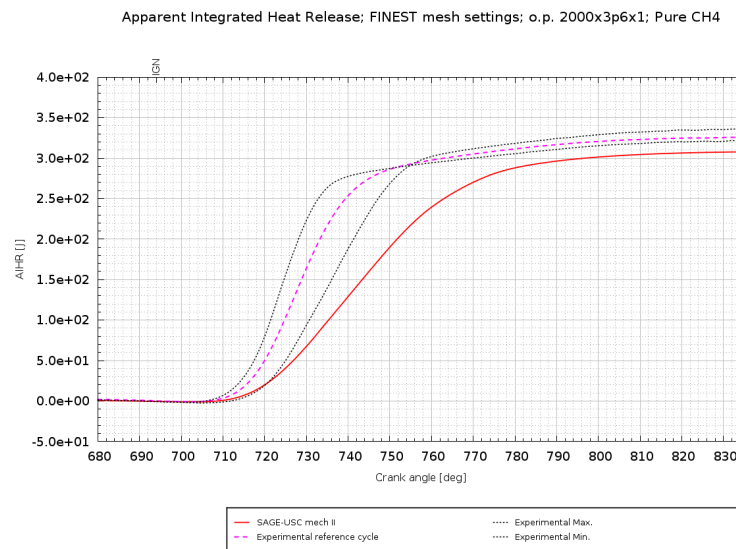


Figure 6.18: Integrated Heat release (IHR): SAGE-*USC-Mech II* and experimental data, Finest mesh settings, Pure CH₄

Figures 6.17 and 6.18 respectively show the Heat release rate and the Integrated Heat release plot for both simulation results obtained with SAGE-*USC-Mech II* and experimental data.

As expected from Fig. 6.16, the model results are far from the experimental values of Heat release.

The simulation regarding the SAGE-*AramcoMech 2.0* has been stopped after the many restarts: simulation problems are connected to memory usage, since the mechanism contains a significant number of species and reactions and the mesh settings are also particularly fine. In fact, runtime per crank angle was remarkably long, and therefore the only results got are referred to the first cycle, which is not considered for an accurate CFD analysis, as already said. For this reason the results will not be

shown here.

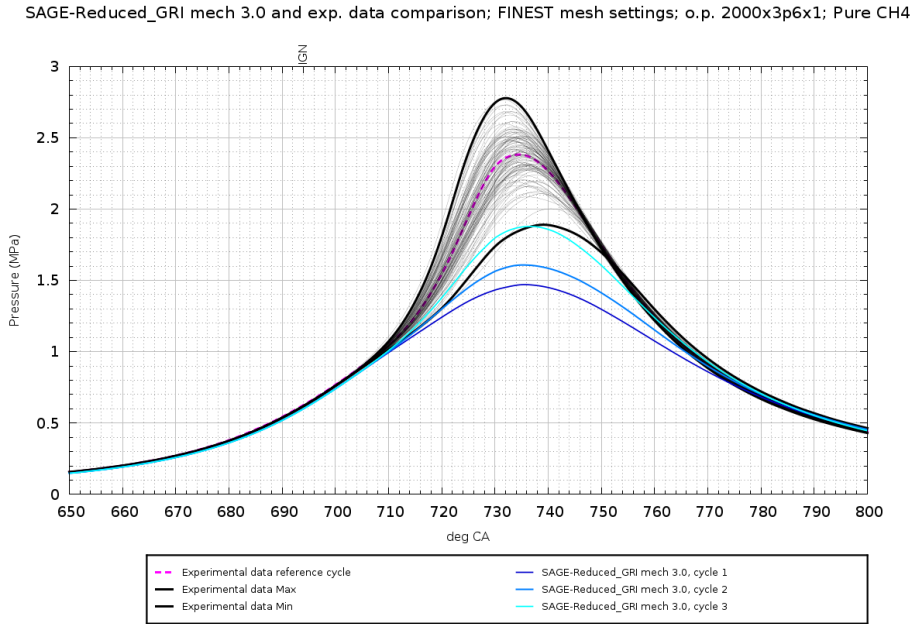


Figure 6.19: Pressure in cylinder 1: SAGE-Reduced *GRI-Mech 3.0* and experimental data, Finest mesh settings, Pure CH₄

In figure 6.19 it is shown the comparison between the results obtained with the simulation SAGE-Reduced *GRI-Mech 3.0* and the experimental data in the matter of the Pressure in cylinder 1.

Except the third, all the pressure profiles of the simulation cycles lie outside the range described by the experimental pressure profiles characterized by the maximum and the minimum peaks. Therefore, the mechanism does not perform particularly good with this mesh settings.

The pressure at the *SA*, i.e. the value of pressure in cylinder 1 corresponding to 694 crank angle degree, is about 0.6 MPa, for both experimental data and simulation result.

The simulation crank angle degree corresponding to the peak pressure in cylinder 1, i.e. θ_{peak} is about 735 deg (considering the model cycle whose pressure profile is the closest to the experimental ensemble average), while the experimental one (considering the experimental reference cycle) happens to be about 734 deg.

The simulation peak pressure value, i.e. p_{peak} is about 1.9 MPa (always taking into account the model cycle whose pressure profile is the closest to the experimental ensemble average) while the experimental one (considering the experimental reference cycle) is about 2.4 MPa.

The runtime of this simulation has been 46 hours per cycle, using 3 nodes corresponding to 12 cores.

Figures 6.20 and 6.21 respectively show the Heat release rate and the Integrated Heat release plot for both simulation results obtained with SAGE-Reduced *GRI-Mech 3.0* and experimental data.

Also in this case, the simulation results are not very similar to the experimental ones.

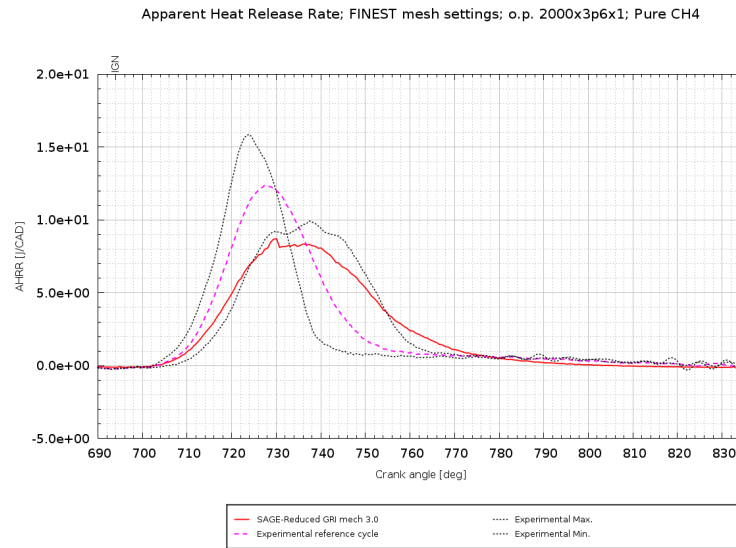


Figure 6.20: Heat release rate (HRR): SAGE-Reduced GRI-Mech 3.0 and experimental data, Finest mesh settings, Pure CH₄

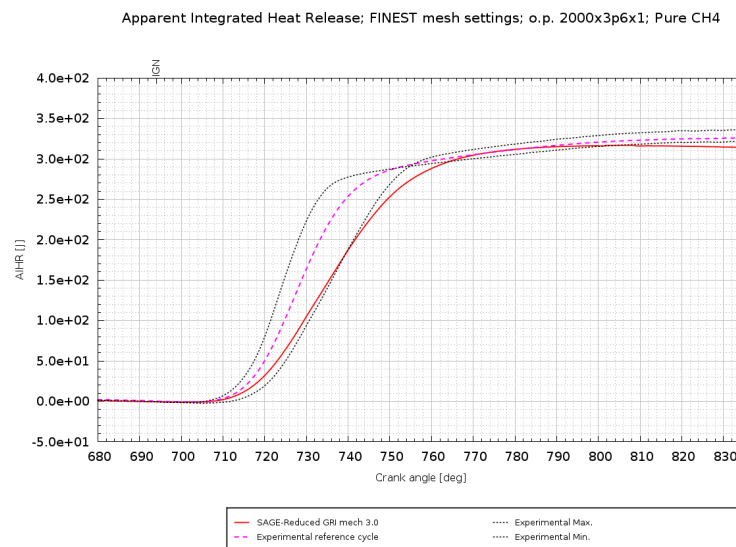


Figure 6.21: Integrated Heat release (IHR): SAGE-Reduced GRI-Mech 3.0 and experimental data, Finest mesh settings, Pure CH₄

Fine mesh settings

Figure 6.22 shows a comparison between the results obtained with the simulation SAGE-GRI-Mech 3.0 and the experimental data in the matter of the Pressure in cylinder 1.

All the simulation cycles, even the first one, are inside the range "Min÷Max". The pressure profiles of the second and the third simulation cycles perfectly match that of the experimental reference cycle; therefore there is coincidence between experimental data and simulation results for the pressure at the SA and the peak pressure values, as well as the crank angle degrees corresponding to the peak pressure in cylinder 1. It is therefore right to say that this mechanism perfectly performs with with mesh settings.

The runtime of this simulation has been 39.1 hours per cycle, using 3 nodes corre-

SAGE-GRI mech 3.0 and exp. data comparison; FINE mesh settings; o.p. 2000x3p6x1; Pure CH₄

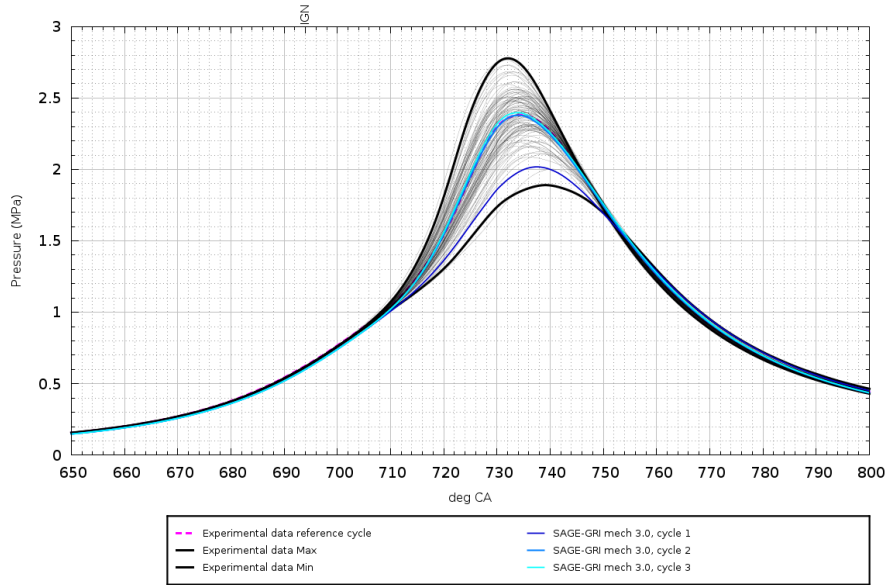


Figure 6.22: Pressure in cylinder 1: SAGE-GRI-Mech 3.0 and experimental data, Fine mesh settings, Pure CH₄

sponding to 12 cores.

Apparent Heat Release Rate; FINE mesh settings; o.p. 2000x3p6x1; Pure CH₄

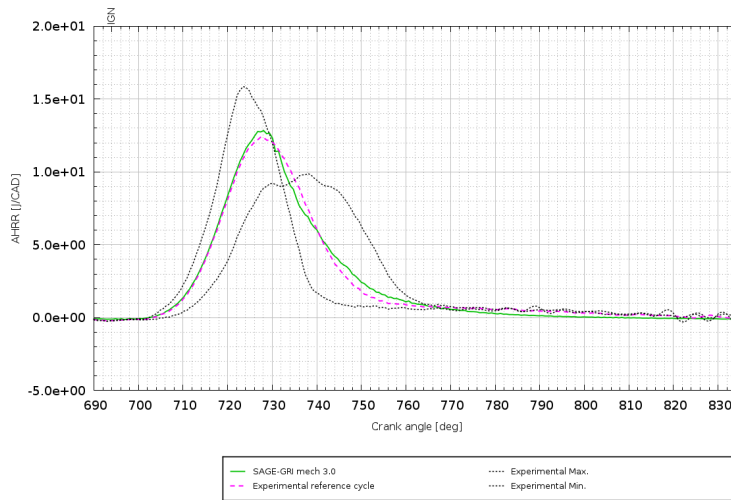


Figure 6.23: Heat release rate (HRR): SAGE-GRI-Mech 3.0 and experimental data, Fine mesh settings, Pure CH₄

Figures 6.23 and 6.24 respectively show the Heat release rate and the Integrated Heat release plot for both simulation results obtained with SAGE-GRI-Mech 3.0 and experimental data.

In both the figures it is possible to notice that the HRR and IHR of the model are match almost perfectly the experimental ones.

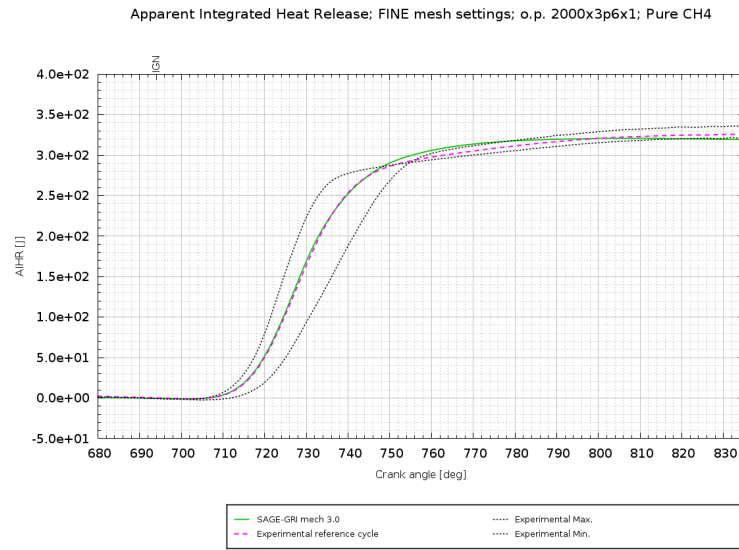


Figure 6.24: Integrated Heat release (IHR): SAGE-*GRI-Mech 3.0* and experimental data, Fine mesh settings, Pure CH₄

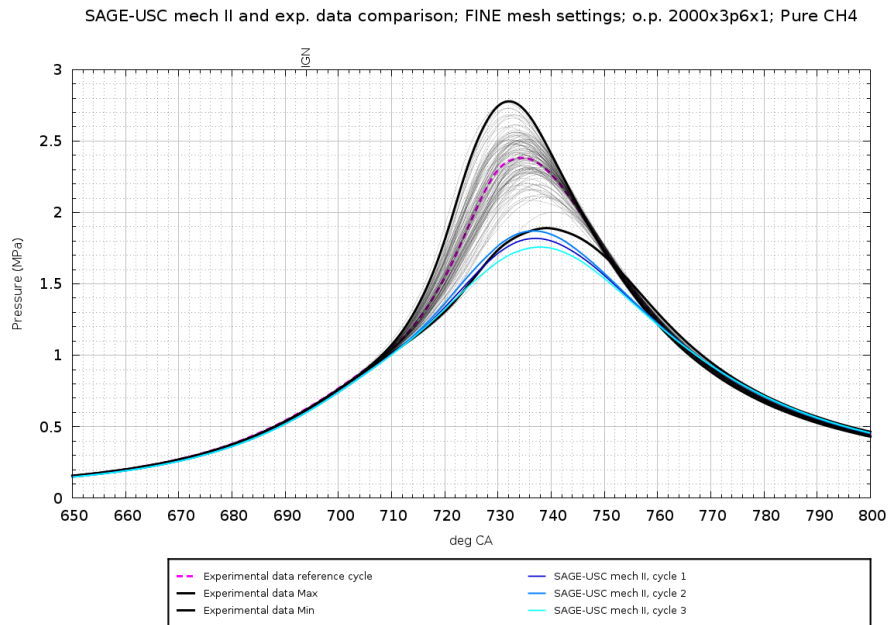


Figure 6.25: Pressure in cylinder 1: SAGE-*USC-Mech II* and experimental data, Fine mesh settings, Pure CH₄

Figure 6.25 shows the comparison between the results obtained with the simulation SAGE-*USC-Mech II* and the experimental data in the matter of the Pressure in cylinder 1.

The mechanism still provides results which are a little underestimated with regards to the experimental data, but they are more coherent. The pressure at the *SA*, i.e. the value of pressure in cylinder 1 corresponding to 694 crank angle degree, is about 0.6 MPa, for both experimental data and simulation result.

The simulation crank angle degree corresponding to the peak pressure in cylinder 1, i.e. θ_{peak} is about 735 deg, while the experimental one is about 734 deg.

The simulation peak pressure value, i.e. p_{peak} is about 1.9 MPa, while the experimental one is about 2.4 MPa.

The runtime of this simulation has been 50 hours per cycle, using 5 nodes and 20 cores.

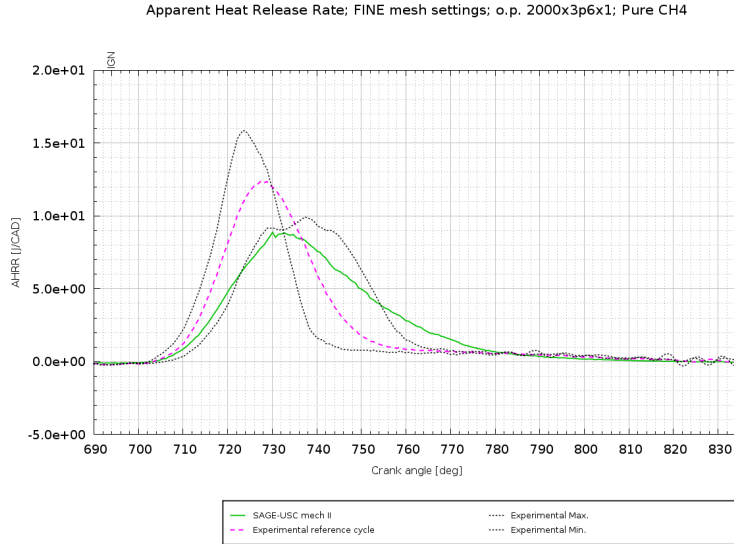


Figure 6.26: Heat release rate (HRR): SAGE-*USC-Mech II* and experimental data, Fine mesh settings, Pure CH₄

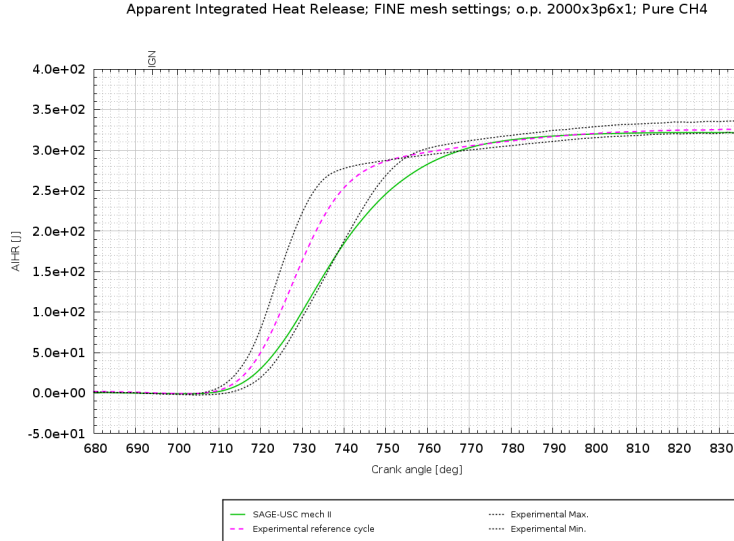


Figure 6.27: Integrated Heat release (IHR): SAGE-*USC-Mech II* and experimental data, Fine mesh settings, Pure CH₄

Figures 6.26 and 6.27 respectively show the Heat release rate and the Integrated Heat release plot for both simulation results obtained with SAGE-*USC-Mech II* and experimental data.

The *HRR* and *IHR* of the model do not match very well the experimental ones.

The CFD simulation with SAGE-*AramcoMech 2.0* has been stopped for the same reasons of the *Finest* mesh settings, and therefore, also in this case, the results will

not be shown.

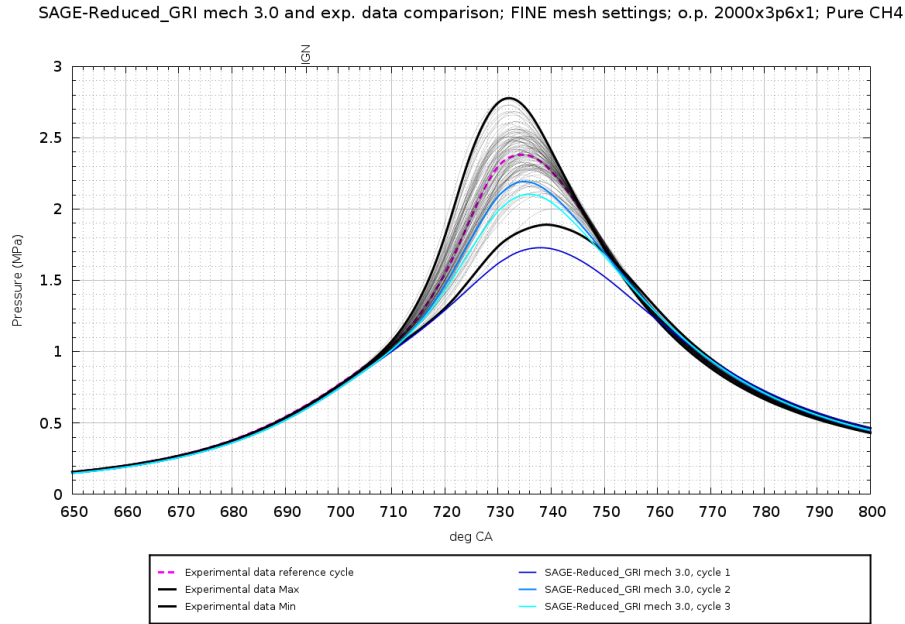


Figure 6.28: Pressure in cylinder 1: SAGE-Reduced GRI-Mech 3.0 and experimental data, Fine mesh settings, Pure CH₄

Figure 6.28 shows the comparison between the results obtained with the simulation SAGE-Reduced GRI-Mech 3.0 and the experimental data in the matter of the Pressure in cylinder 1. The image is focused on the range between 650÷800 crank angle degree.

Apart from the first, the pressure profiles of the simulation cycles lie outside the range described by the experimental pressure profiles characterized by the maximum and the minimum peaks, and are quite close to the experimental reference cycle. Therefore, the mechanism performs good with this mesh settings.

The pressure at the *SA*, i.e. the value of pressure in cylinder 1 corresponding to 694 crank angle degree, is about 0.6 MPa, for both experimental data and simulation result.

The simulation crank angle degree corresponding to the peak pressure in cylinder 1, i.e. θ_{peak} coincides with the experimental reference cycle one, which is 734 deg.

The simulation peak pressure value, i.e. p_{peak} is about 2.2 MPa while the experimental reference cycle one is about 2.4 MPa.

The runtime of this simulation has been about 32 hours per cycle, using 3 nodes corresponding to 12 cores.

Figures 6.29 and 6.30 respectively show the Heat release rate and the Integrated Heat release plot for both simulation results obtained with SAGE-Reduced GRI-Mech 3.0 and experimental data.

The figures show that the *HRR* and the *IHR* of the model are not that different with respect to the experimental ones, in agreement with the pressure profile reported figure 6.28.

The CFD simulation with SAGE-AramcoMech 2.0 has been stopped for the same reasons of the *Finest* mesh settings, and therefore, also in this case, the results will not be shown.

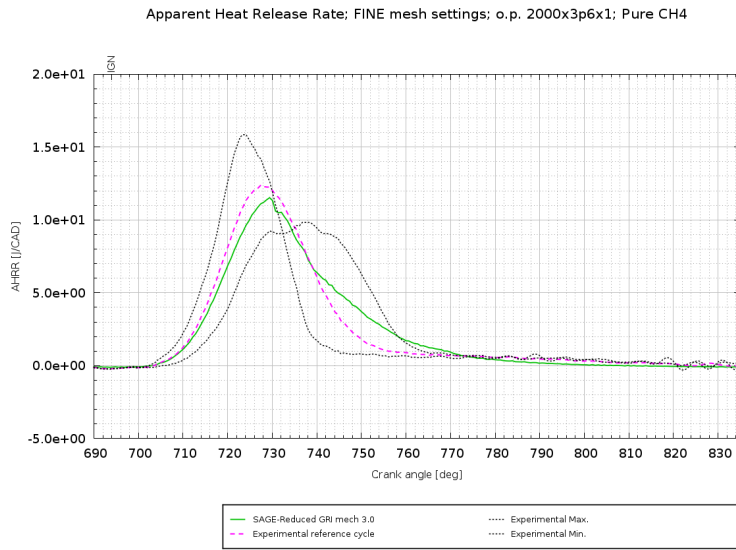


Figure 6.29: Heat release rate (HRR): SAGE-Reduced GRI-Mech 3.0 and experimental data, Fine mesh settings, Pure CH₄

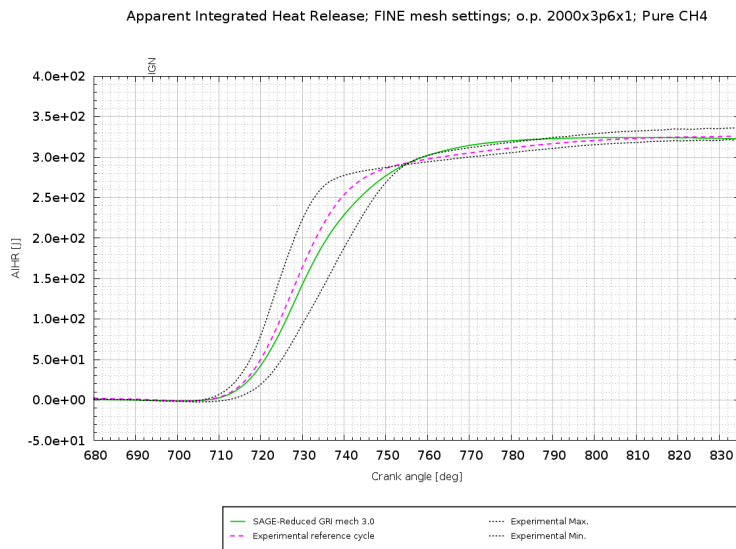


Figure 6.30: Integrated Heat release (IHR): SAGE-Reduced GRI-Mech 3.0 and experimental data, Fine mesh settings, Pure CH₄

Figure 6.31 shows a comparison between the results obtained with the simulation SAGE-GRI-Mech 3.0 with dynamic reduction (DMR) and the experimental data in the matter of the Pressure in cylinder 1.

Model pressure profiles of the different cycles are all included in the range $Min \div Max$ and, except for the first one, they are quite overestimated with respect to the experimental reference cycle.

Figures 6.32 and 6.33 respectively show the Heat release rate and the Integrated Heat release plot for both simulation results obtained with SAGE-GRI-Mech 3.0 with dynamic reduction (DMR) and experimental data.

The figures show that the HRR and the IHR of the model are not that different with respect to the experimental ones, but a little bit overestimated with regards to the

SAGE-GRI_dyn. reduction mech II and exp. data comparison; FINE mesh settings; o.p. 2000x3p6x1; Pure CH₄

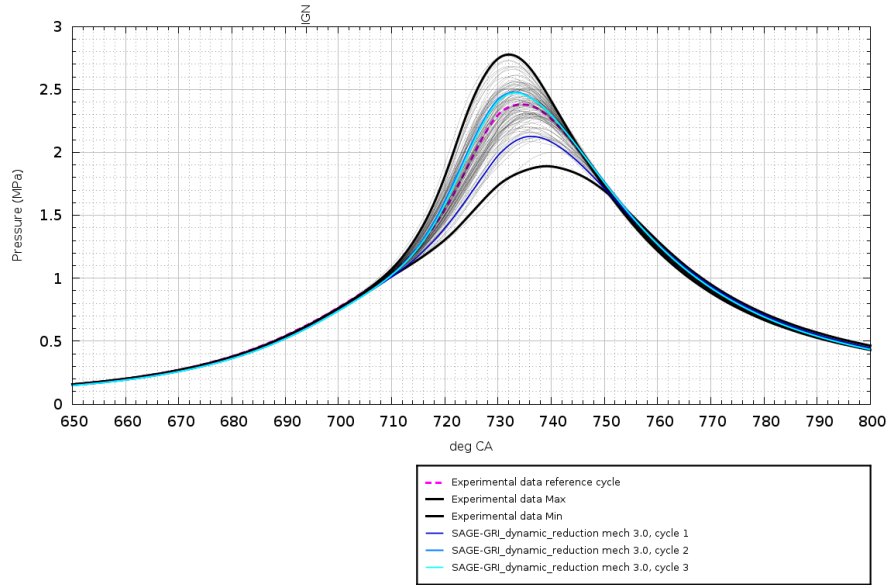


Figure 6.31: Pressure in cylinder 1: SAGE-*GRI-Mech 3.0 (DMR)* and experimental data, Fine mesh settings, Pure CH₄

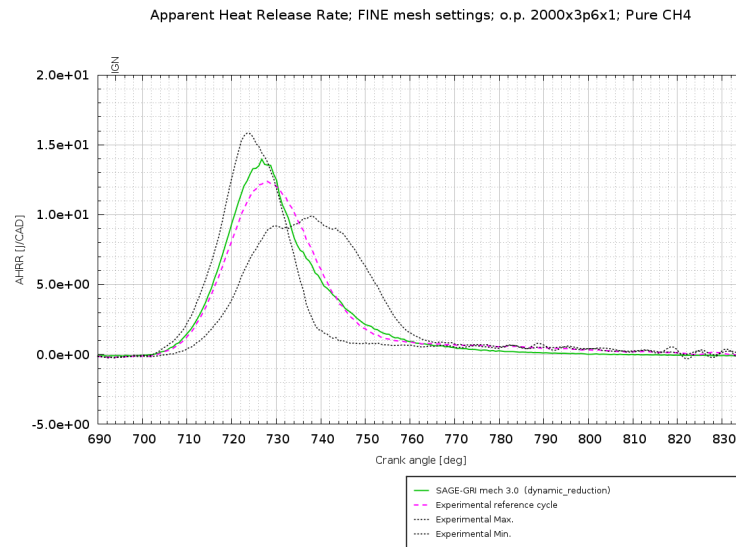


Figure 6.32: Heat release rate (HRR): SAGE-*GRI-Mech 3.0 (DMR)* and experimental data, Fine mesh settings, Pure CH₄

experimental reference cycle.

The runtime of this simulation has been 35 hours per cycle, using 3 nodes corresponding to 12 cores.

Figure 6.34 shows a comparison between the results obtained with the simulation SAGE-*USC-Mech II* with dynamic reduction (DMR) and the experimental data in the matter of the Pressure in cylinder 1.

Model pressure profile of the third cycle is inside the range $Min \div Max$ and quite close to the experimental reference cycle.

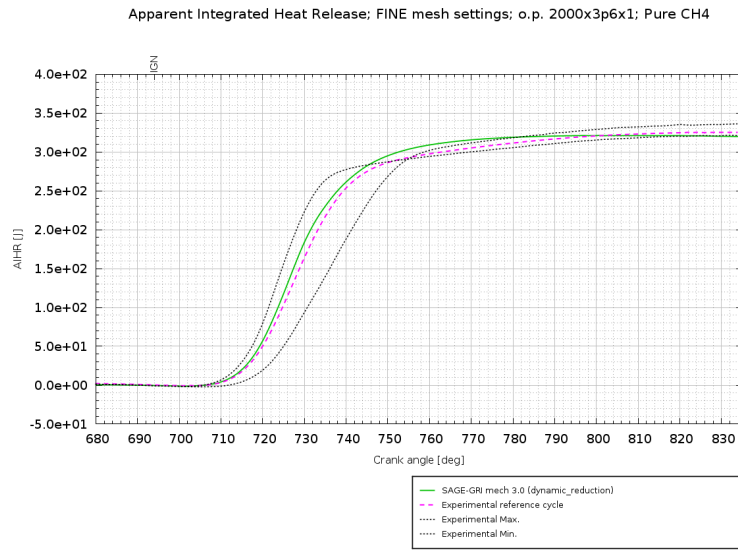


Figure 6.33: Integrated Heat release (IHR): SAGE-*GRI-Mech 3.0 (DMR)* and experimental data, Fine mesh settings, Pure CH₄

SAGE-GRI_dyn. reduction mech II and exp. data comparison; FINE mesh settings; o.p. 2000x3p6x1; Pure CH₄

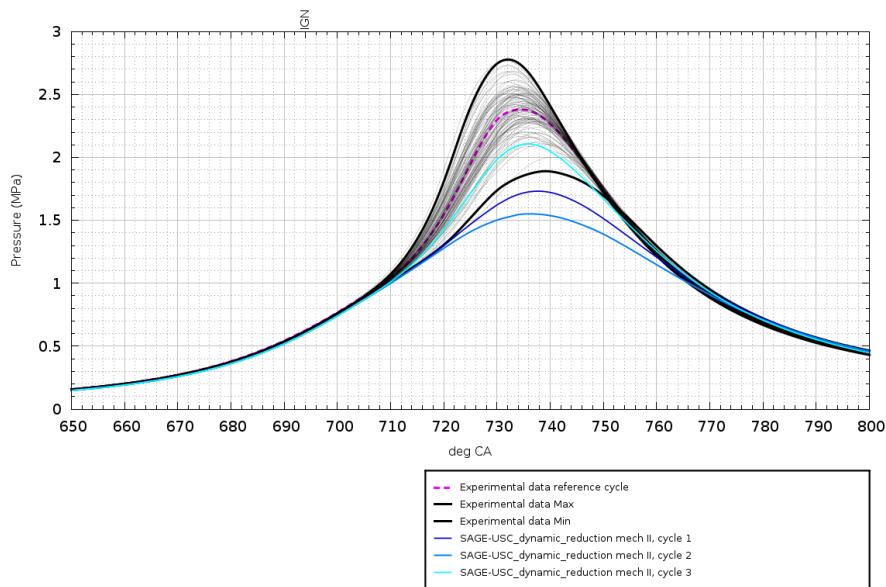


Figure 6.34: Pressure in cylinder 1: SAGE-*USC-Mech II (DMR)* and experimental data, Fine mesh settings, Pure CH₄

Figures 6.35 and 6.36 respectively show the Heat release rate and the Integrated Heat release plot for both simulation results obtained with SAGE-*USC-Mech II* with dynamic reduction (DMR) and experimental data.

The figures show that the *HRR* and the *IHR* of the model are not that different with respect to the experimental ones, but a little bit underestimated with regards to the experimental reference cycle.

The runtime of this simulation has been about 50 hours per cycle, using 5 nodes corresponding to 20 cores. Therefore there is not a reduction in the runtime, but an improvement in the results.

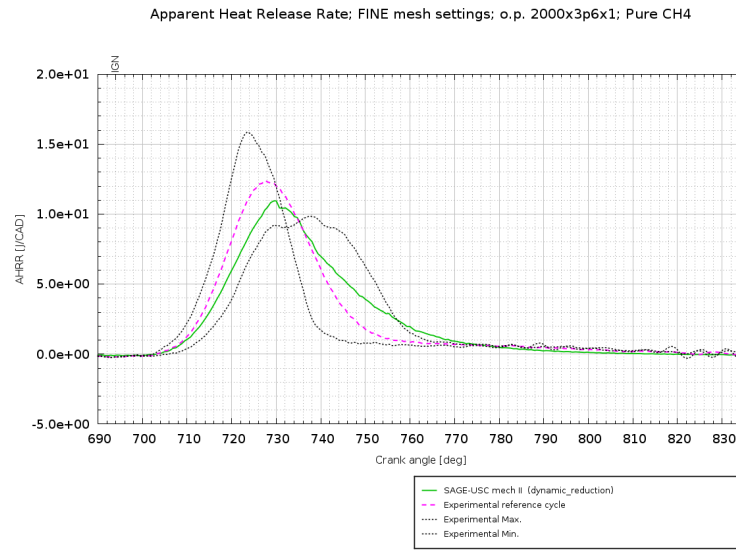


Figure 6.35: Heat release rate (HRR): SAGE-USC-Mech II (DMR) and experimental data, Fine mesh settings, Pure CH₄

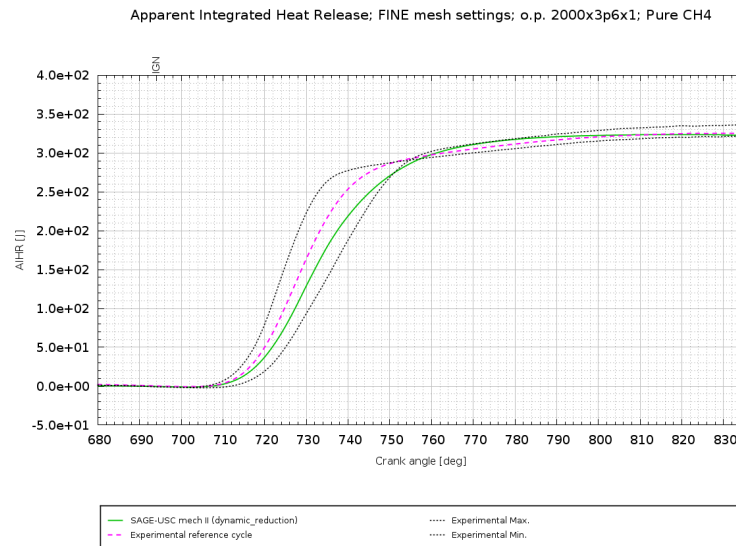


Figure 6.36: Integrated Heat release (IHR): SAGE-USC-Mech II (DMR) and experimental data, Fine mesh settings, Pure CH₄

Mechanisms comparison

Figure 6.37 shows the results obtained with SAGE model together with the different mechanisms used in case of *Coarse* mesh settings. Also in this case, the simulation cycles considered are those whose pressure curve is the closest to the experimental ensemble average, and so will be for the other plots.

The *GRI-Mech 3.0* is the mechanism that, for this mesh settings, provides the best result, while the *USC-Mech II* gives a pressure curve which is mostly inside the experimental range *Max ÷ Min*, but underestimated with respect to the experimental reference cycle. The other two mechanisms, i.e. the pressure profiles obtained with

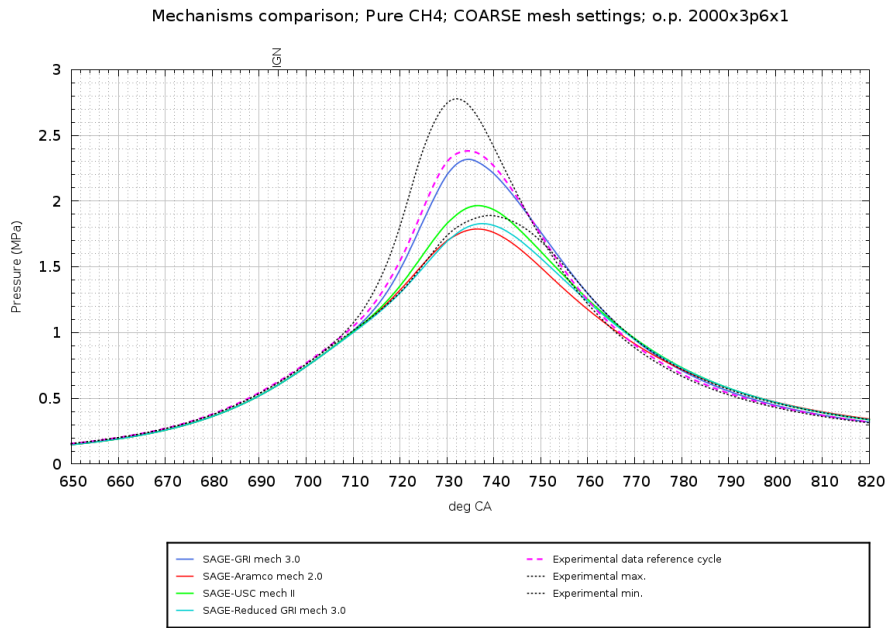


Figure 6.37: Pressure in cylinder 1: Mechanisms comparison, Coarse mesh settings, Pure CH₄

Reduced-GRI-Mech 3.0 and *Aramco-Mech2.0* are out of the aforementioned range, so these mechanisms do not perform well with this mesh settings.

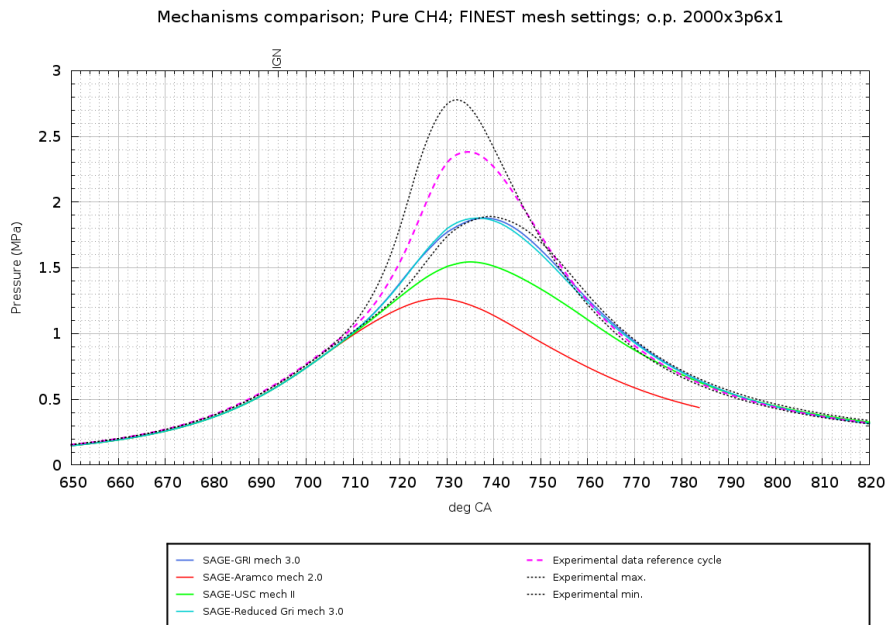


Figure 6.38: Pressure in cylinder 1: Mechanisms comparison, Finest mesh settings, Pure CH₄

Figure 6.38 shows the results obtained with SAGE model together with the different mechanisms used in case of *Finest* mesh settings.

The *GRI-Mech 3.0* and the *Reduced GRI-Mech 3.0* turn out to be the mechanisms that, for this mesh settings, provide the best results, which are, however, underestimated with respect to the experimental reference cycle.

The *USC-Mech II* and the *Aramco-Mech2.0* give pressure curves outside the experimental range $Max \div Min$.

It must be specified that the pressure curve regarding the model *SAGE-Aramco-Mech2.0* shown in the image are referred just to the first cycle.

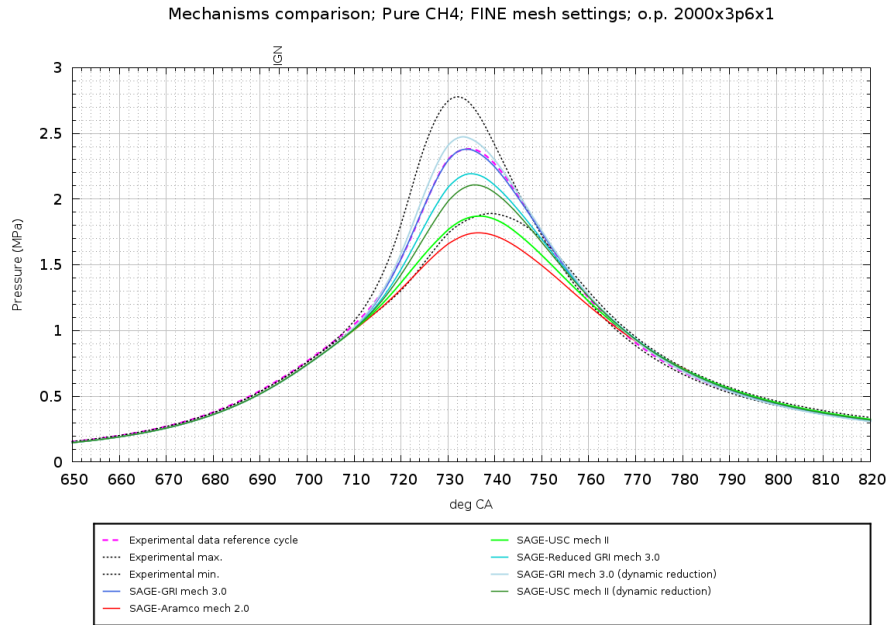


Figure 6.39: Pressure in cylinder 1: Mechanisms comparison, Fine mesh settings, Pure CH₄

Figure 6.39 shows the results obtained with SAGE model together with the different mechanisms used in case of *Fine* mesh settings.

The *GRI-Mech 3.0* turn out to be the mechanisms that, for this mesh settings, provide the best results. The *Reduced GRI-Mech 3.0* also provides good results, as well as the *GRI-Mech 3.0 (DMR)* and the *USC-Mech II (DMR)*. The *USC-Mech II* and the *Aramco-Mech2.0* give pressure curves a little bit outside the experimental range $Max \div Min$.

It must be specified that also in this case the pressure curve regarding the model *SAGE-Aramco-Mech2.0* shown in the image are referred just to the first cycle.

Mesh settings comparison

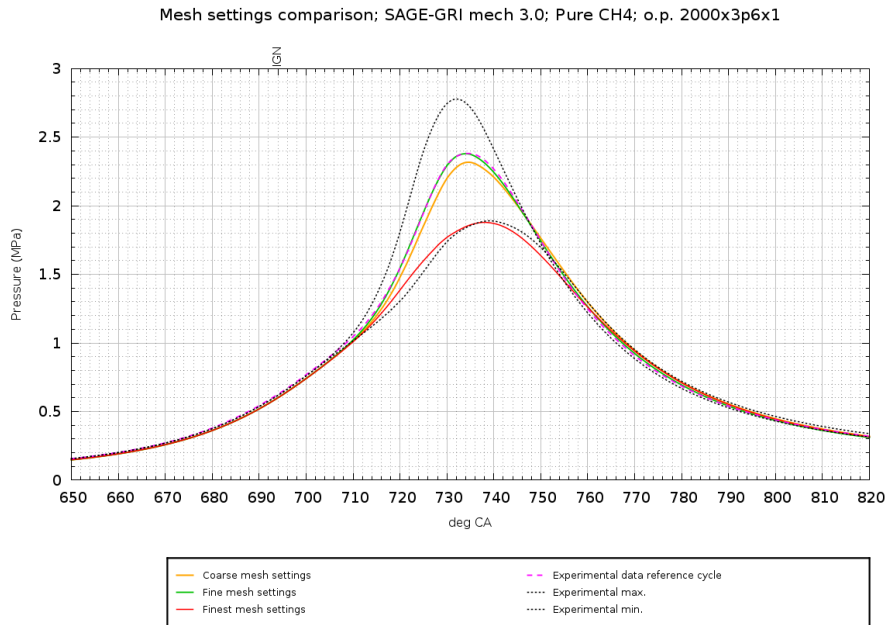


Figure 6.40: Pressure in cylinder 1: Mesh settings comparison; experimental data vs SAGE-GRI-Mech 3.0

Figure 6.40 shows the results the comparison between the experimental data with the results obtained with the SAGE-*GRI-Mech 3.0* model, for the three mesh settings adopted.

The *Fine* mesh settings is the one which provides, for the SAGE-*GRI-Mech 3.0* model, the best results, even though the *Coarse* mesh is also good. The *Finest* mesh settings is instead the worst, as the results it gives are underestimated.

In order to investigate the reason why the *Finest* mesh settings turns out to be so bad, further analysis has been carried out and other variables have been studied, such as *Number of cells*, y^+ , fluid *Temperature*, *Velocity*, and *TKE* in cylinder 1. To perform this analysis the software ANSYS-*EnSight* has also been used; it is a post-processor and visualization program, which helps to explore and explain complex systems and processes, and handles CONVERGE simulation output data, after being post-converted.

SAGE-*GRI-Mech 3.0* model is here considered.

Figure 6.41 shows a comparison between the three different mesh settings considered for the SAGE-*GRI-Mech 3.0* model.

The plot is sequential, i.e. it shows the number of cells in cylinder 1 for all the cycles that have been performed by the simulations, which are three. One can notice that the *Finest* mesh has, as expected, a very high number of cells with regards to the other two meshes. The highest number of cell is of course around the combustion time (i.e. around $694 \div 1000$ crank angle degrees for the first cycle, around $1414 \div 1720$ deg for the second cycle, about $2134 \div 2440$ deg for the third cycle).

For the *Finest* mesh the second cycle, which is the one which has been considered as the model reference cycle since it is the closest to the experimental ensemble cycle, is that in whose number of cells around combustion is the minimum with respect to the other two cycles.

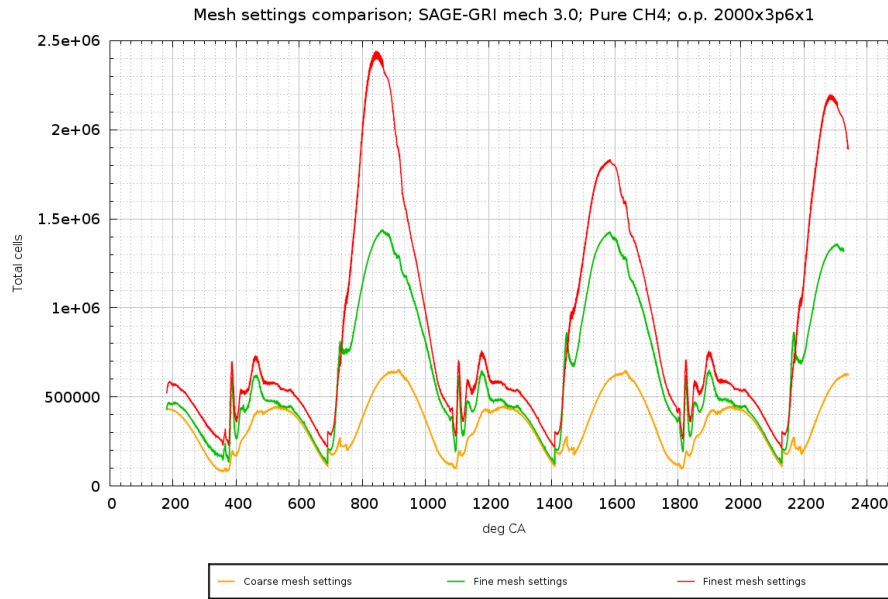
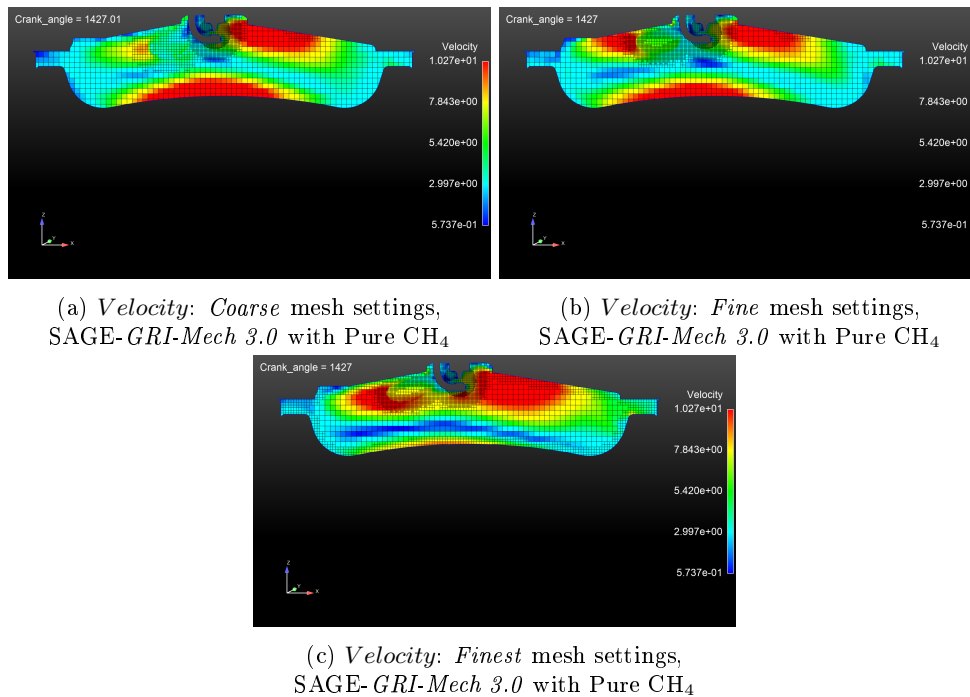


Figure 6.41: Number of cells cylinder 1: Mesh settings comparison; SAGE-GRI-Mech 3.0



(a) Velocity: Coarse mesh settings, SAGE-GRI-Mech 3.0 with Pure CH₄

(b) Velocity: Fine mesh settings, SAGE-GRI-Mech 3.0 with Pure CH₄

(c) Velocity: Finest mesh settings, SAGE-GRI-Mech 3.0 with Pure CH₄

Figure 6.42: Mesh settings comparison on Velocity, SAGE-GRI-Mech 3.0 with Pure CH₄

Figure 6.42 shows a mesh settings comparison for what matters the velocity inside the cylinder 1. The three images which compose figure 6.42 report the situation of the three different meshes at the same crank angle, i.e. 1427 crank angle degree, and are referred to the second simulation cycle (for the aforementioned reasons). The *Finest* mesh has a different behaviour with respect to the other two meshes,

which are of course different in the magnitude of the velocity, but also quite similar in the location of the higher values of that variable. In particular, one can notice that at the bottom wall the *Finest* mesh provides values of velocity which are underestimated with respect to the other two cases.

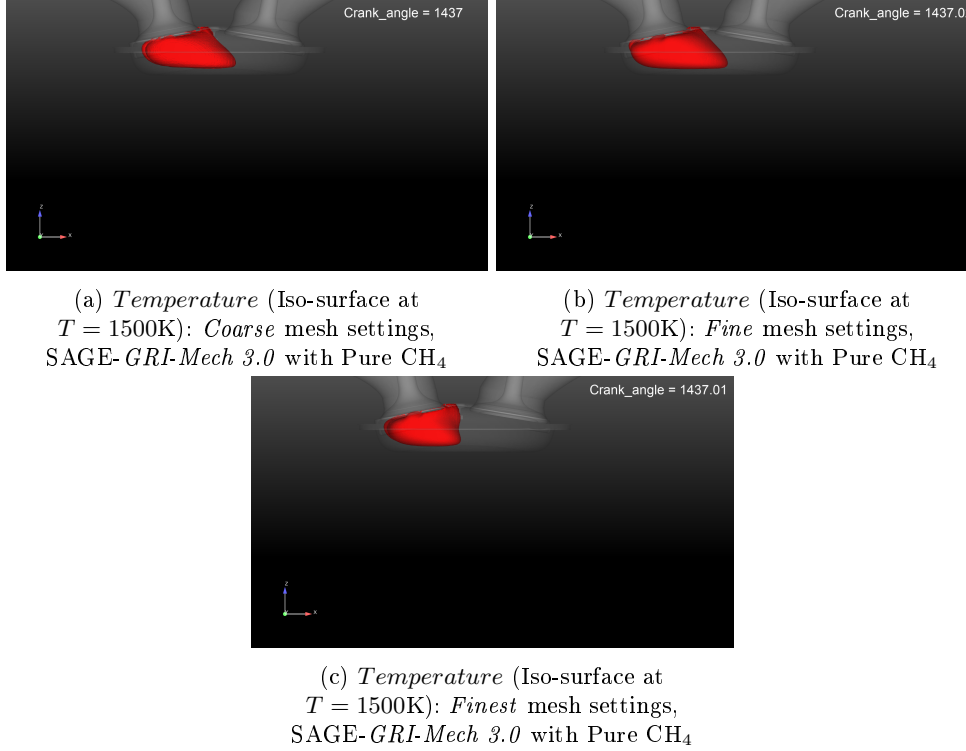


Figure 6.43: Mesh settings comparison on *Temperature* (Iso-surface at $T = 1500\text{K}$), SAGE-*GRI-Mech 3.0* with Pure CH_4

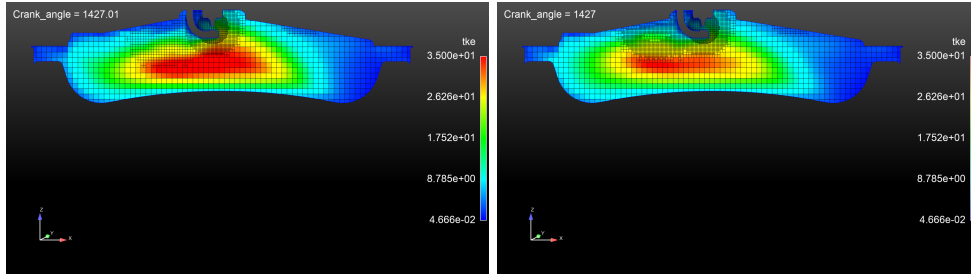
Figure 6.43 shows temperature iso-surfaces at $T = 1500\text{K}$ inside the cylinder 1 for the three different mesh settings. The crank angle considered here is 1437 deg. The images are referred to the second simulation cycle (for the aforementioned reasons). The *Finest* mesh has a different behaviour with respect to the other two meshes. In particular, the way the high temperature involves the fluid inside the cylinder has, for *Finest* mesh, a different trend with regards to the other two meshes.

Figure 6.44 shows a mesh comparison with *TKE* as variable. The three images of figure 6.44 are taken for 1427 crank angle degree, at the second simulation cycle (for the aforementioned reasons).

For the same time, i.e. for the same crank angle degree, the *Finest* mesh provides values of *TKE* which are different from the other two cases for both magnitude and trend. In particular, one can notice that in the core of the cylinder, *TKE* has lower values with respect to the other two mesh settings.

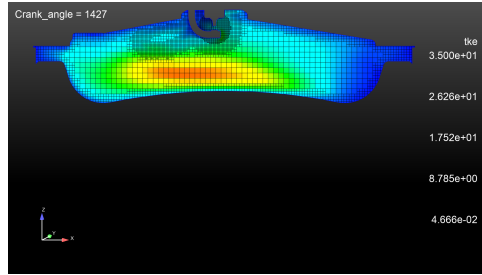
Figure 6.45 shows the same results of figure 6.44 but from a different view, i.e. from above, just beneath the spark. As it can be noticed, the *Finest* mesh provides underestimated values of *TKE*, if compared to the other two meshes.

Figure 6.46 shows the y^+ values on the surface of the cylinder, for the *Coarse* (fig. 6.46a), *Fine* (fig. 6.46b), and *Finest* (fig. 6.46c) meshes. The range of Y^+ values considered is $10 \div 250$; as discussed in the previous chapters, if the y^+ value of a cell adjacent to a wall falls outside of the range for the chosen model, i.e. $20 < y^+ < 200$



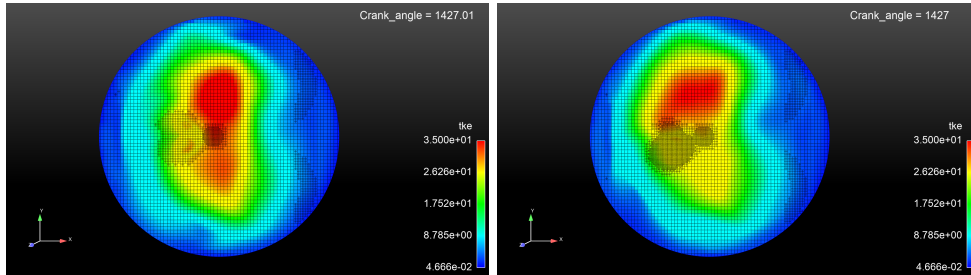
(a) *TKE*: Coarse mesh settings, SAGE-*GRI-Mech 3.0* with Pure CH₄

(b) *TKE*: Fine mesh settings, SAGE-*GRI-Mech 3.0* with Pure CH₄



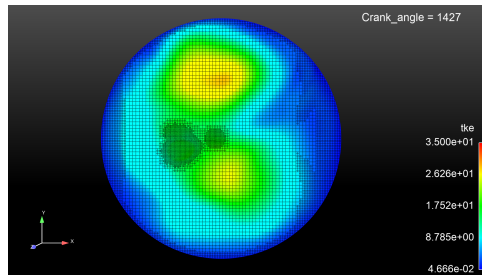
(c) *TKE*: Finest mesh settings, SAGE-*GRI-Mech 3.0* with Pure CH₄

Figure 6.44: *TKE*: Mesh settings comparison, SAGE-*GRI-Mech 3.0* with Pure CH₄



(a) *TKE* from above: Coarse mesh settings, SAGE-*GRI-Mech 3.0* with Pure CH₄

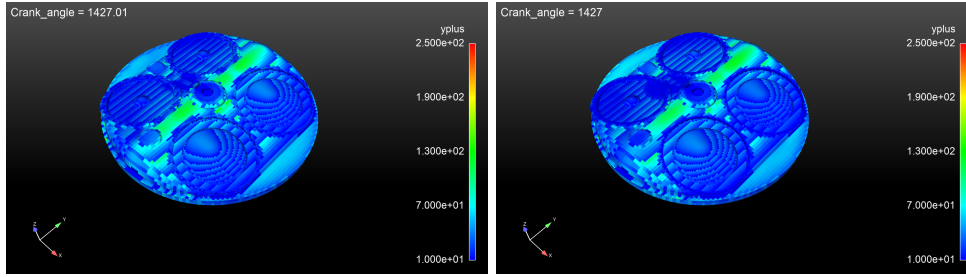
(b) *TKE* from above: Fine mesh settings, SAGE-*GRI-Mech 3.0* with Pure CH₄



(c) *TKE* from above: Finest mesh settings, SAGE-*GRI-Mech 3.0* with Pure CH₄

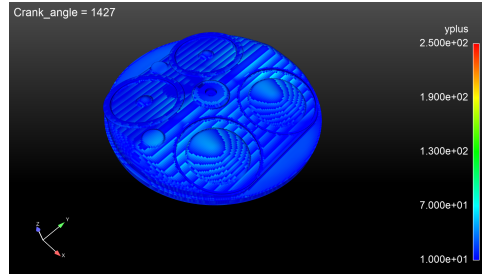
Figure 6.45: Mesh settings comparison on *TKE* from above, SAGE-*GRI-Mech 3.0* with Pure CH₄

in this application case, *Law of Wall* models will no longer produce physically realistic results. As it can be seen, the *Finest* mesh is the one characterized by the lowest values of y^+ , below the minimum value of 20, as it is confirmed also by figure 6.47. This figure shows that around the crank angles when combustion takes place, the



(a) y^+ : *Coarse* mesh settings, SAGE-*GRI-Mech 3.0* with Pure CH_4

(b) y^+ : *Fine* mesh settings, SAGE-*GRI-Mech 3.0* with Pure CH_4



(c) y^+ : *Finest* mesh settings, SAGE-*GRI-Mech 3.0* with Pure CH_4

Figure 6.46: Mesh settings comparison on y^+ , SAGE-*GRI-Mech 3.0* with Pure CH_4

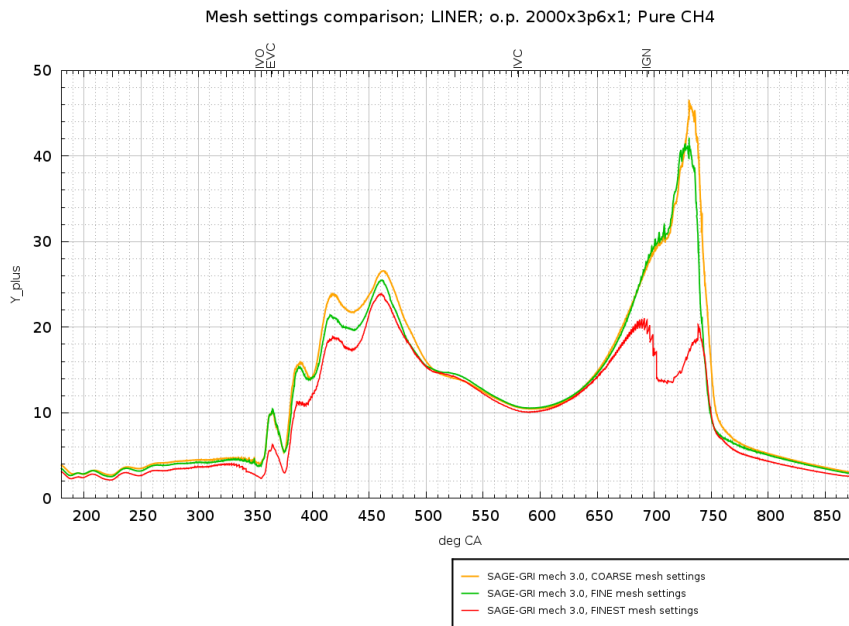


Figure 6.47: y^+ on the LINER: Mesh settings comparison; SAGE-*GRI-Mech 3.0*

Finest mesh is characterized by very low values of y^+ , below 20; this behaviour is definitely opposite to that of the other two meshes. Therefore, the reason for which this mesh settings does not provide good results could be traced back to this issue.

The mesh settings comparison with the other mechanisms, i.e. *USC-Mech II* and *Reduced GRI-Mech 3.0*, will be shown below.

The *SAGE-AramcoMech 2.0* is left out in this analysis, since the results regarding the *Fine* and *Finest* meshes are incomplete.

Figure 6.48 shows the results the comparison between the experimental data with the results obtained with the *SAGE-USC-Mech II* model, for the three mesh settings adopted.

The *Coarse* mesh settings is the one which provides, for the *SAGE-USC-Mech II* model, the best results, but still underestimated with respect to the experimental reference cycle. The *Finest* mesh settings is instead the worst, as the results it gives are underestimated.

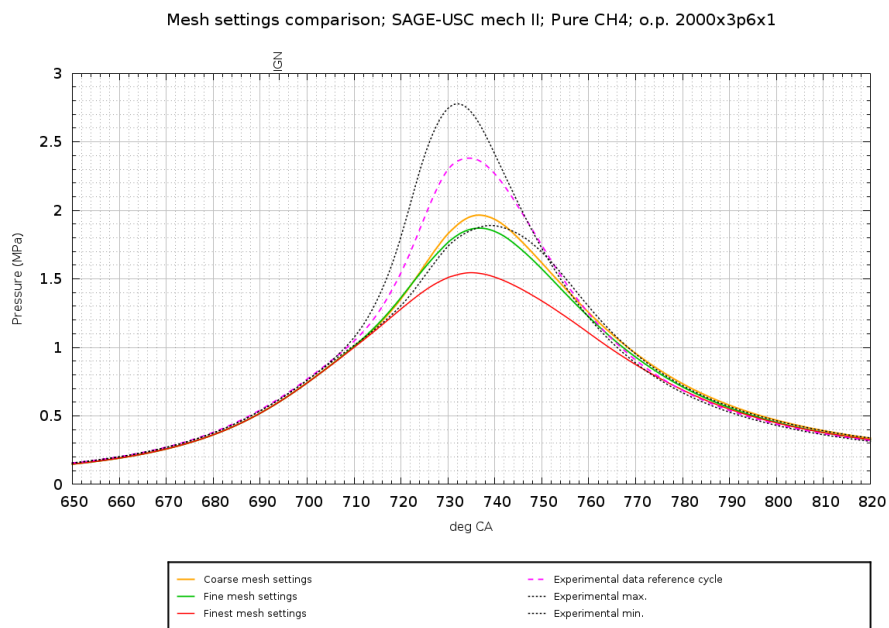


Figure 6.48: Pressure in cylinder 1: Mesh settings comparison; experimental data vs *SAGE-USC-Mech II*

Figure 6.49 shows the result obtained by the *SAGE-Reduced GRI-Mech 3.0* model with the three different meshes considered and the experimental data.

The *Fine* mesh settings is the one which provides, for this model, the best results, which are just a little underestimated with respect to the experimental reference cycle. The results obtained with the *Coarse* mesh settings are instead the worst and very similar to those got with the *Finest* mesh.

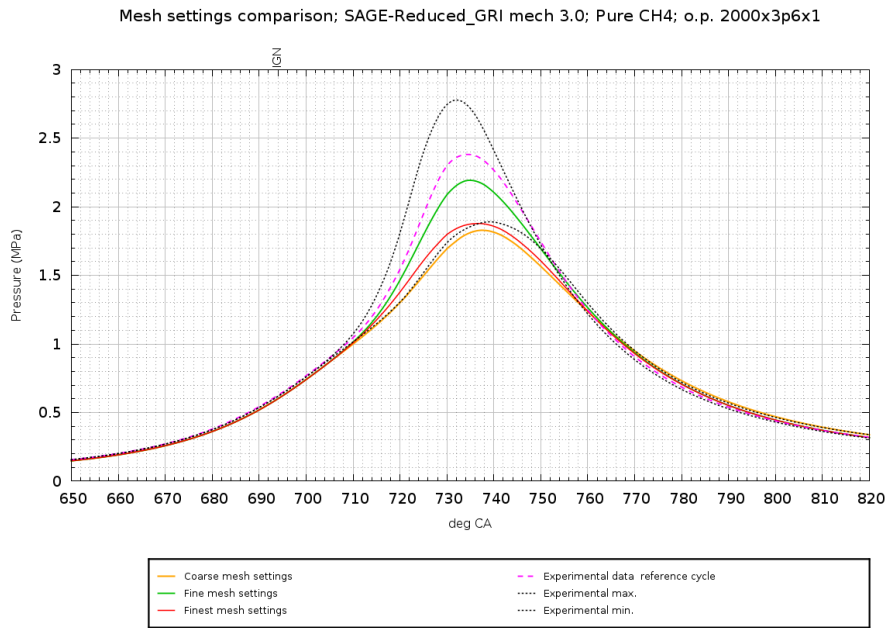


Figure 6.49: Pressure in cylinder 1: Mesh settings comparison; experimental data vs SAGE-Reduced GRI-Mech 3.0

6.2.2 Actual fuel composition

In this section, comparisons between the results obtained by using Pure CH₄ as engine fuel and those got by using the more accurate fuel composition, i.e. *Actual fuel composition* will be shown.

Coarse mesh settings

In figure 6.50 one can see the comparison between the results obtained by using Pure CH₄ and *Actual fuel composition* as fuel, for the SAGE-GRI-Mech 3.0 model with *Coarse* mesh settings.

As expected, the *Actual fuel composition* provides results characterized by a pressure profile which perfectly matches the experimental reference cycle; thus, using this kind of fuel with this mesh settings is better than using Pure CH₄.

Figure 6.51 shows the comparison between the results obtained by using Pure CH₄ and *Actual fuel composition* as fuel, for the SAGE-USC-Mech II model with *Coarse* mesh settings.

As expected, the *Actual fuel composition* gives a pressure profile which is closer to the experimental reference cycle.

Figure 6.52 shows the pressure curve obtained by using Pure CH₄ as fuel and that got by using a fuel with *Actual fuel composition*, for the SAGE-Reduced GRI-Mech 3.0 model, with *Coarse* mesh settings.

The *Actual fuel composition* provides results which are closer to the experimental reference cycle, but still quite underestimated.

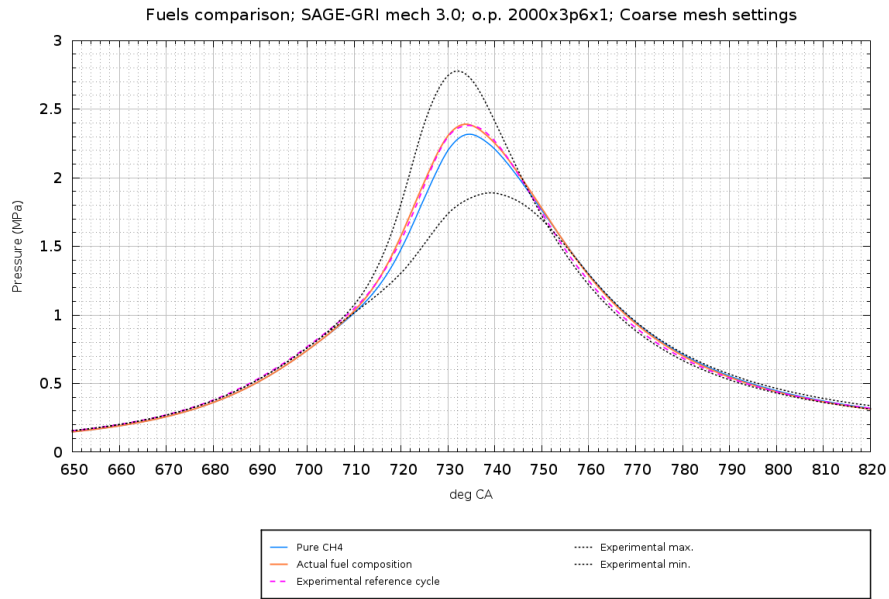


Figure 6.50: Pressure in cylinder 1: Fuels comparison; SAGE-*GRI-Mech 3.0*; *Coarse* mesh settings

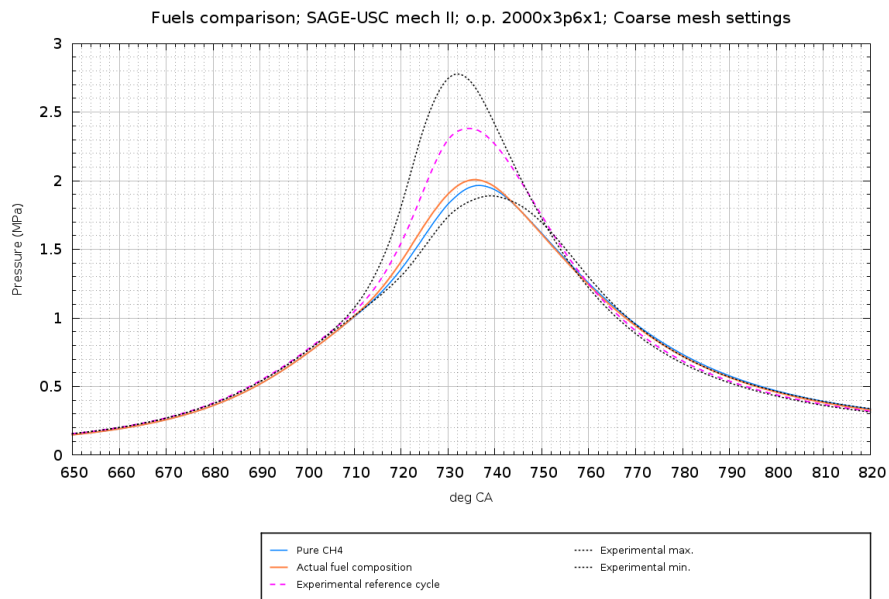


Figure 6.51: Pressure in cylinder 1: Fuels comparison; SAGE-*USC-Mech II*; *Coarse* mesh settings

Fine mesh settings

Figure 6.53 reports the comparison between the results obtained with the two different fuels, for the SAGE-*GRI-Mech 3.0* model with *Fine* mesh settings. This time, the *Actual fuel composition* provides a pressure curve which is a little bit overestimated with respect to that obtained by using Pure CH₄; the results are still

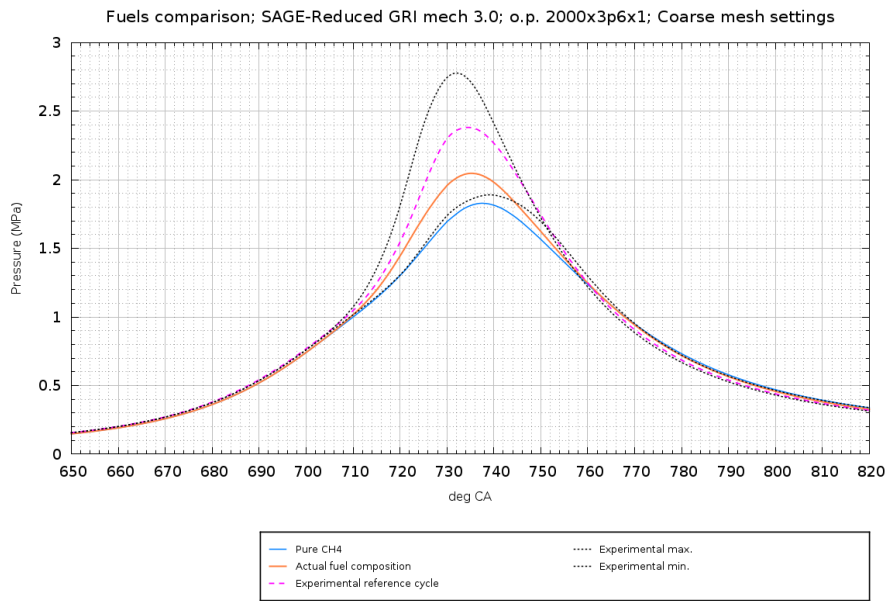


Figure 6.52: Pressure in cylinder 1: Fuels comparison; SAGE-*Reduced GRI-Mech 3.0*; *Coarse* mesh settings

very good.

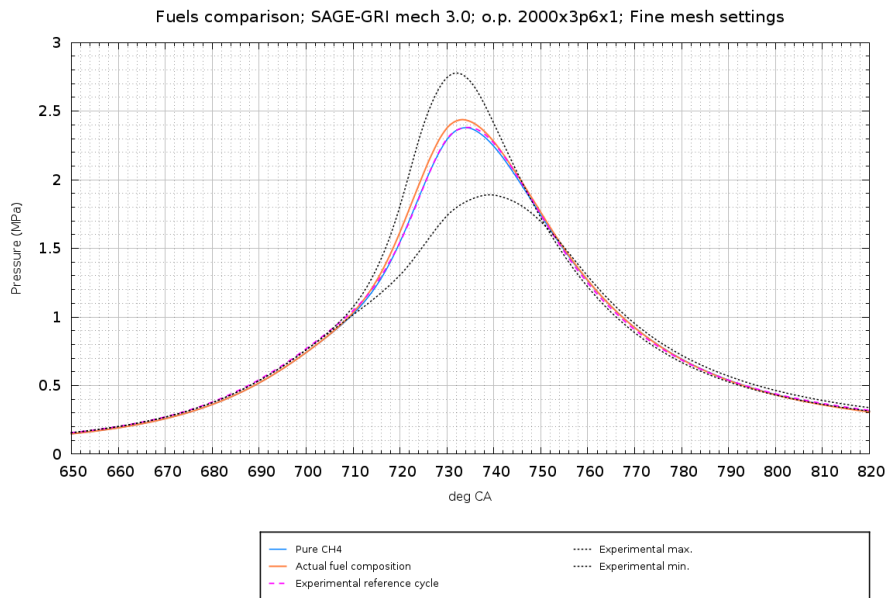


Figure 6.53: Pressure in cylinder 1: Fuels comparison; SAGE-*GRI-Mech 3.0*; *Fine* mesh settings

Figure 6.54 shows the comparison between the results obtained by using Pure CH₄ and *Actual fuel composition* as fuel, for the SAGE-*USC-Mech II* model with *Fine* mesh settings.

The *Actual fuel composition* gives a pressure profile which is closer to the experimental reference cycle. The results with this mesh settings and fuel are good, so the mechanism can be considered suitable.

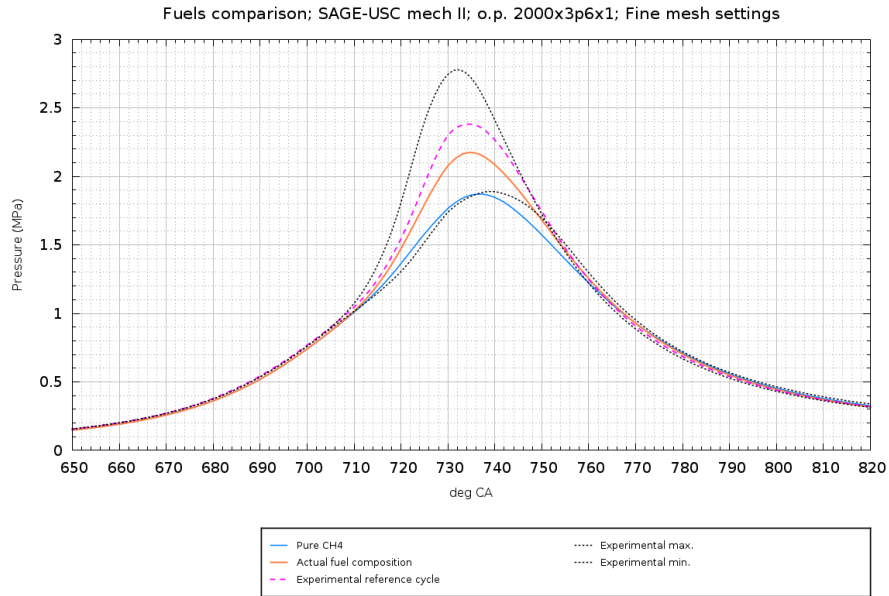


Figure 6.54: Pressure in cylinder 1: Fuels comparison; SAGE-USC-Mech II; Fine mesh settings

Figure 6.55 shows the pressure curve obtained by using Pure CH₄ as fuel and that got by using a fuel with *Actual fuel composition*, for the SAGE-Reduced GRI-Mech 3.0 model, with *Fine* mesh settings.

The *Actual fuel composition* provides results which are very close to the experimental reference cycle.

Therefore, the skeletal reduction of the mechanism, together with the *Fine* mesh and this kind of fuel, can be considered suitable for the SAGE model of the *Fiat FIRE 1.4 16V Turbo CNG* engine: this means that it is possible to obtain very good results for a very small runtime (SAGE-GRI-Mech 3.0 with *Coarse* mesh needs 23 hours/cycle, while SAGE-Reduced GRI-Mech 3.0 with *Fine* mesh needs 22 hours/cycle using for both 3 nodes and 12 cores)

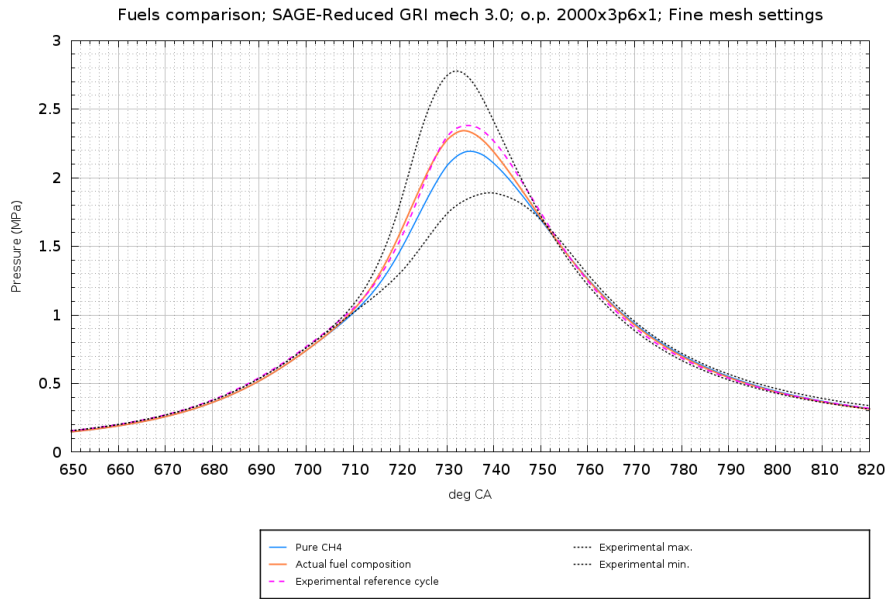


Figure 6.55: Pressure in cylinder 1: Fuels comparison; SAGE-*Reduced GRI-Mech 3.0*; *Fine* mesh settings

Finest mesh settings

Figure 6.56 shows the pressure curve obtained by using Pure CH₄ as fuel and that got by using a fuel with *Actual fuel composition*, for the SAGE-*GRI-Mech 3.0* model, with *Finest* mesh settings.

As it can be seen, the *Actual fuel composition* gives better results, but this does not help enough to provide a pressure curve which can be considered satisfactorily close to the experimental reference cycle.

For this reason, this mesh has not been used for the other mechanisms, nor for the other engine operating points.

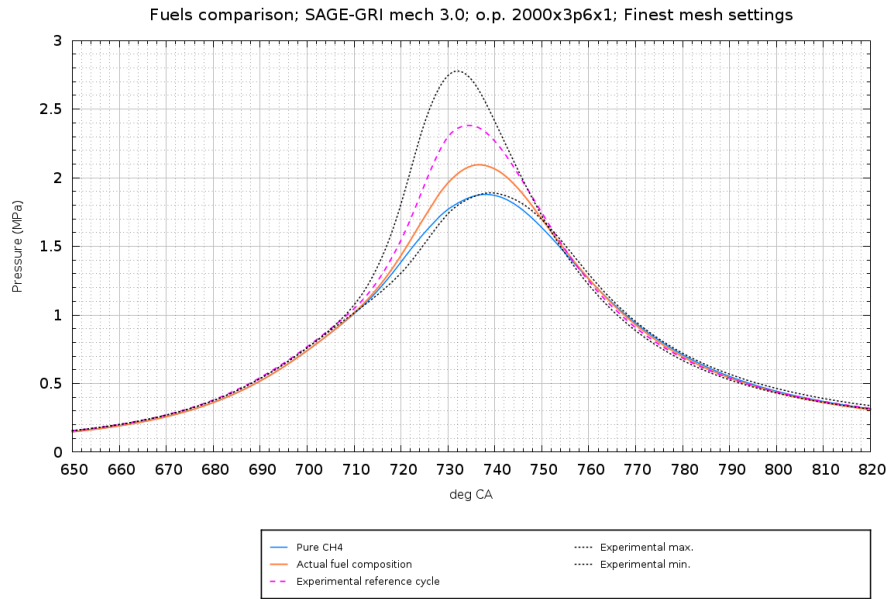


Figure 6.56: Pressure in cylinder 1: Fuels comparison; SAGE-*GRI-Mech 3.0*; *Finest* mesh settings

6.3 2000[rpm] x 7.9[bar] x lambda=1

For what concerns the engine operating point 2000[rpm] x 7.9 [bar] x lambda=1, the simulations in CONVERGE have been carried out just for the fuel *Actual Fuel Composition*, for *Coarse* and *Fine* mesh settings, and for the kinetic mechanisms *GRI-Mech 3.0*, *USC-Mech II* and *Reduced GRI-Mech 3.0*.

Table 6.2 summarizes the cases that have been run.

Table 6.2: O.P. 2000[rpm] x 7.9 [bar] x lambda=1: simulations cases run

Combustion model	Fuel	Mechanism	Mesh settings
SAGE	Actual fuel	<i>GRI-Mech 3.0</i>	Coarse
			Fine
		<i>USC-Mech II</i>	Coarse
			Fine
		<i>Reduced GRI-Mech 3.0</i>	Coarse
			Fine

Coarse mesh settings

Figure 6.57 shows a comparison between the results obtained with the simulation SAGE-*GRI-Mech 3.0* and the experimental data in the matter of the Pressure in cylinder 1. The image is focused on the range between 620÷850 crank angle degree.

Excluding the first cycle, one can notice that the mechanism provides good results with this mesh settings: the peak pressure value, i.e. p_{peak} , is about 4.2 MPa, like that of the experimental reference cycle. The simulation crank angle degree corresponding

SAGE-GRI mech 3.0 and exp. data comparison; COARSE mesh settings; o.p. 2000x7p9x1; Actual fuel comp.

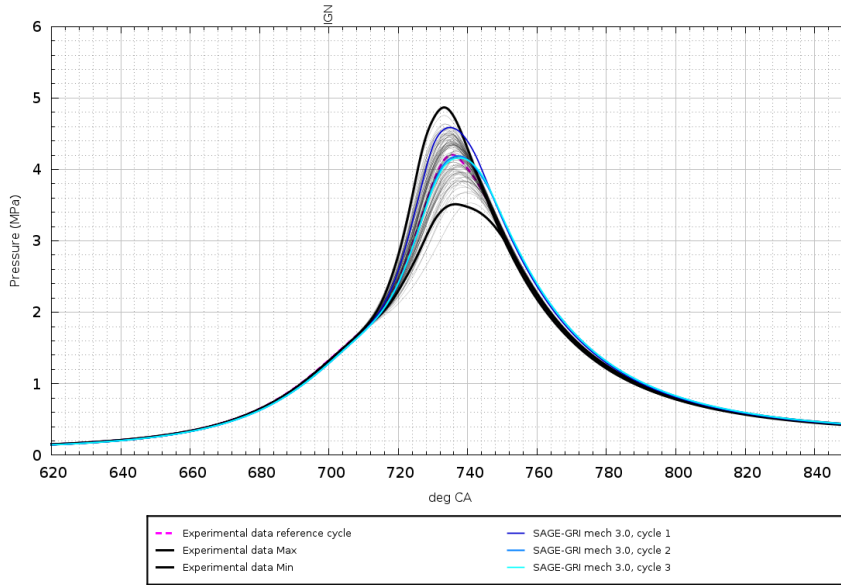


Figure 6.57: Pressure in cylinder 1: SAGE-*GRI-Mech 3.0* and experimental data, Coarse mesh settings, Actual fuel composition

to the peak pressure in cylinder 1, i.e. θ_{peak} is about 736 deg, while the experimental one happens to be about 734 deg.

The pressure at the *SA*, i.e. the value of pressure in cylinder 1 corresponding to 700 crank angle degree, is about 1.4 MPa, for both experimental data and simulation result.

Note that, after 740 deg, the model overestimates a bit the pressure values, so it does not describe perfectly the "burn out" phase, but the results can be still considered good.

The runtime of this simulation has been almost 20 hours per cycle, using 5 nodes corresponding to 30 cores.

Figures 6.58 and 6.59 respectively show the Heat release rate and the Integrated Heat release plot for both simulation results obtained with SAGE-*GRI-Mech 3.0* and experimental data.

The *HRR* and *IHR* of the model look a bit overestimated with respect to the experimental one; this was expected, as the model pressure profiles tend to overestimate the experimental values after a certain crank angle deg.

Figure 6.60 shows a comparison between the pressure curves obtained with SAGE-*USC-Mech II* model and the experimental ones.

Results are not bad, but are underestimated in the crank angle degree range 710÷750, and then become quite overestimated.

Figure 6.61 reports the Heat release rate for both simulation results obtained with SAGE-*USC-Mech II* and experimental data, while 6.62 shows the Integrated Heat release.

The *HRR* and *IHR* of the model look a bit underestimated with respect to the experimental one until 735 crank angle deg, while it becomes overestimated after that. This behaviour was actually expected once seen the pressure curves comparison between model and experimental data.

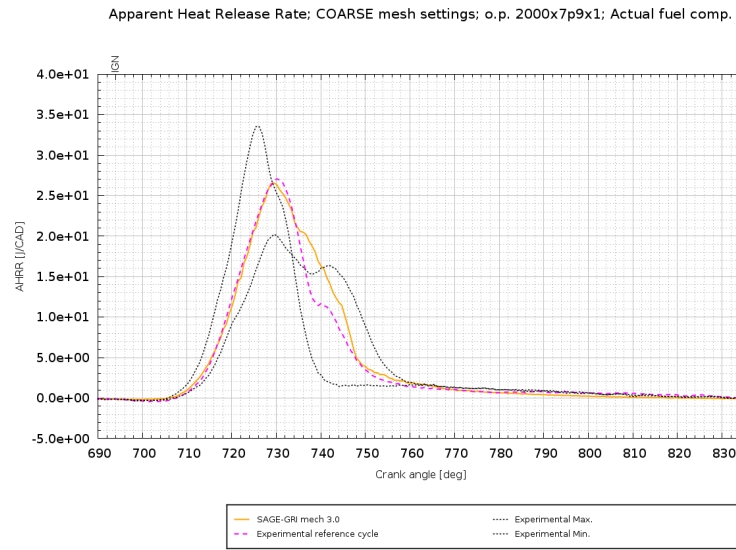


Figure 6.58: Heat release rate in cylinder 1: SAGE-*GRI-Mech 3.0* and experimental data, Coarse mesh settings, Actual fuel composition

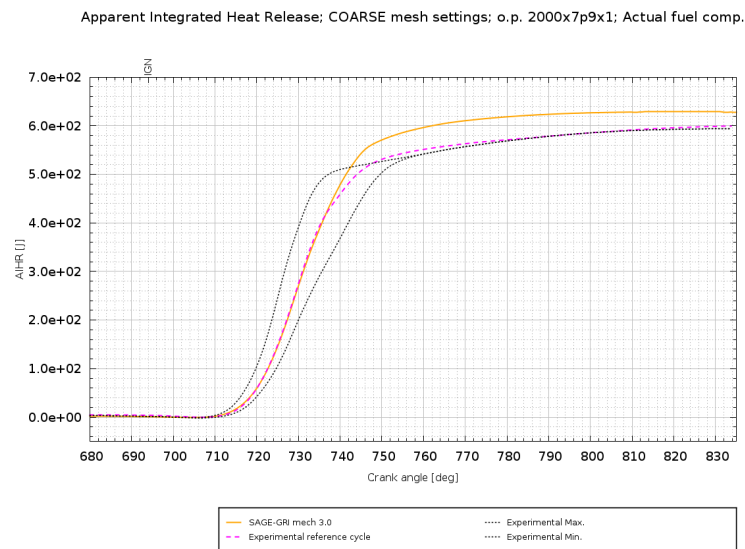


Figure 6.59: Integrated heat rate in cylinder 1: SAGE-*GRI-Mech 3.0* and experimental data, Coarse mesh settings, Actual fuel composition

Therefore, this mesh can be considered not the best choice for this mechanism. The runtime of this simulation has been about 25 hours per cycle, using 5 nodes corresponding to 30 cores.

Figure 6.63 shows the SAGE-*Reduced GRI-Mech 3.0* model results for pressure in cylinder 1, compared to the experimental curves.

The second simulation cycle matches the experimental reference cycle quite perfectly, as the peak pressure happens at almost the same crank angle and has the same value, as well as the pressure at the spark advance; nevertheless, results are a little bit overestimated for the crank angles degrees above 750 deg.

Figures 6.64 and 6.65 show the Heat release rate and the Integrated Heat release, respectively, for what concerns SAGE-*Reduced GRI-Mech 3.0* model and experimen-

SAGE-USC mech II and exp. data comparison; COARSE mesh settings; o.p. 2000x7p9x1; Actual fuel

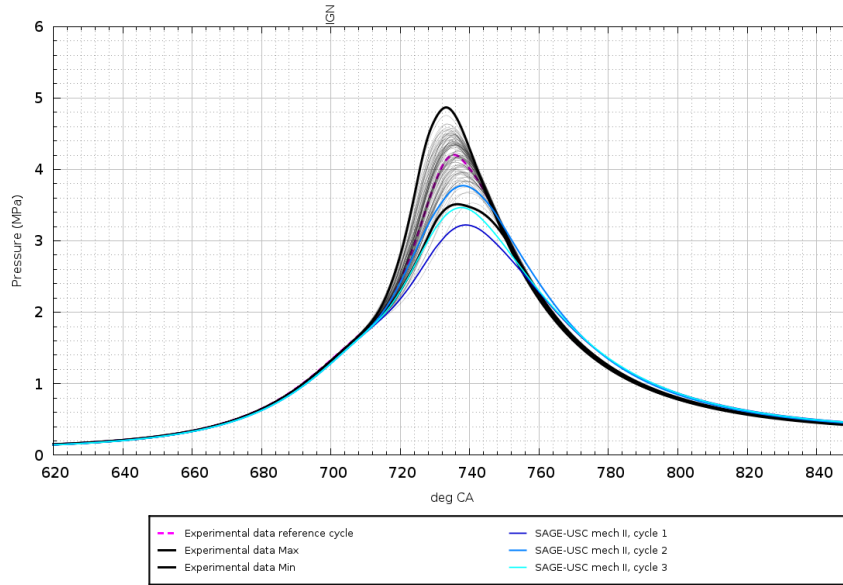


Figure 6.60: Pressure in cylinder 1: SAGE-USC-Mech II and experimental data, Coarse mesh settings, Actual fuel composition

Apparent Heat Release Rate; COARSE mesh settings; o.p. 2000x7p9x1; Actual fuel comp.

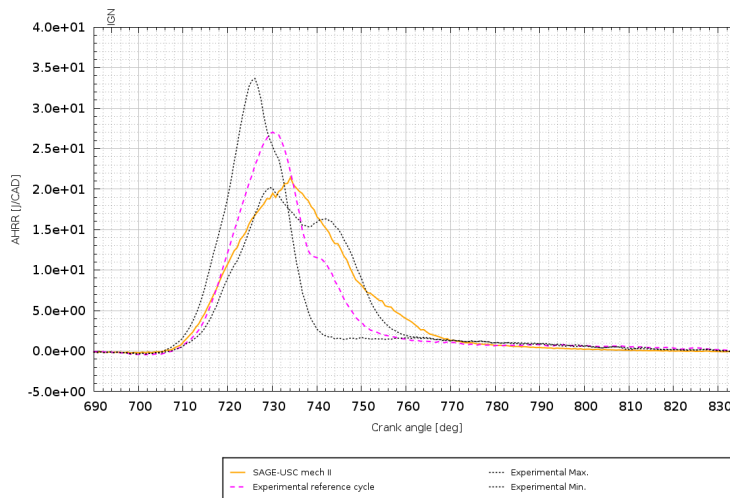


Figure 6.61: Heat release rate in cylinder 1: SAGE-USC-Mech II and experimental data, Coarse mesh settings, Actual fuel composition

tal data.

As it can be noticed, the results are quite good, as the model trend follows the experimental one quite well. The model *IHR* is a slightly overestimated with respect to the experimental values after crank angle 740 deg; this happens also for the *HHR* and the pressure profile.

This mesh can be thus considered a good choice if coupled with this mechanism. Some adjustments have to be done, but the results can be considered satisfactory.

The runtime of this simulation has been 17.73 hours per cycle, using 5 nodes corresponding to 30 cores.

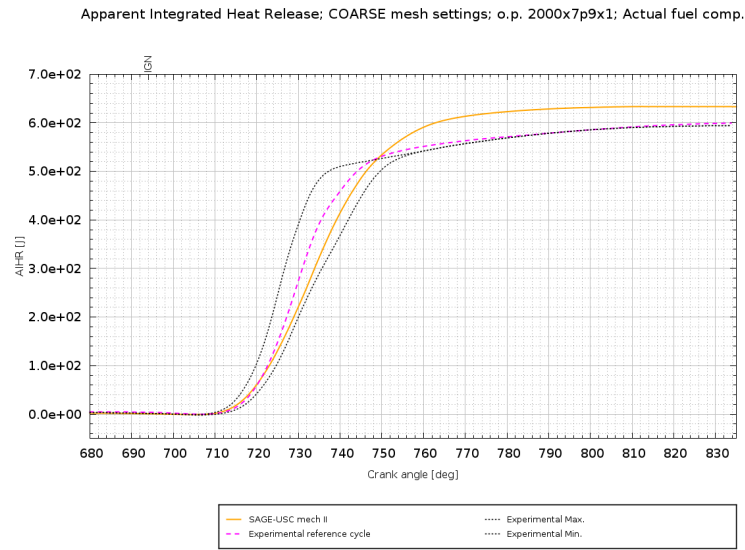


Figure 6.62: Integrated heat release in cylinder 1: SAGE-USC-Mech II and experimental data, Coarse mesh settings, Actual fuel composition

SAGE-Reduced_GRI mech 3.0 and exp. data comparison; COARSE mesh settings; o.p. 2000x7p9x1; Actual fuel

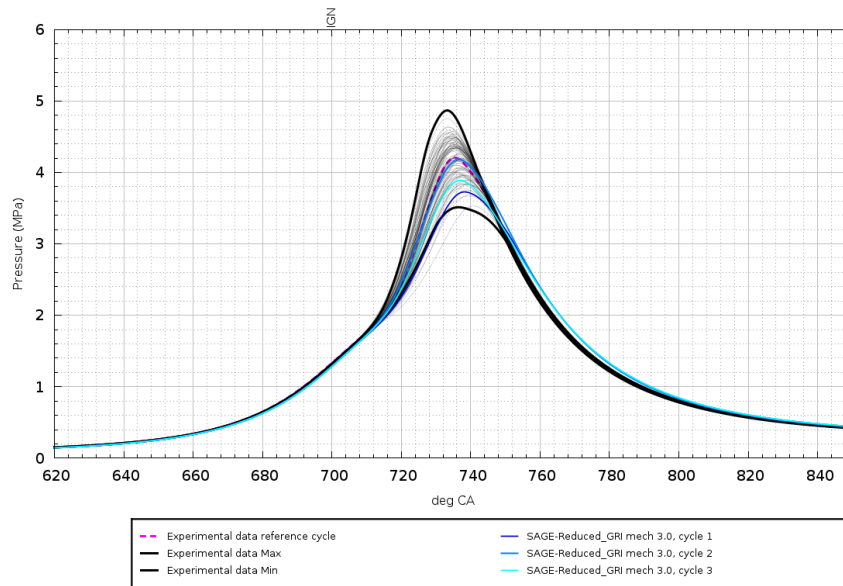


Figure 6.63: Pressure in cylinder 1: SAGE-Reduced GRI-Mech 3.0 and experimental data, Coarse mesh settings, Actual fuel composition

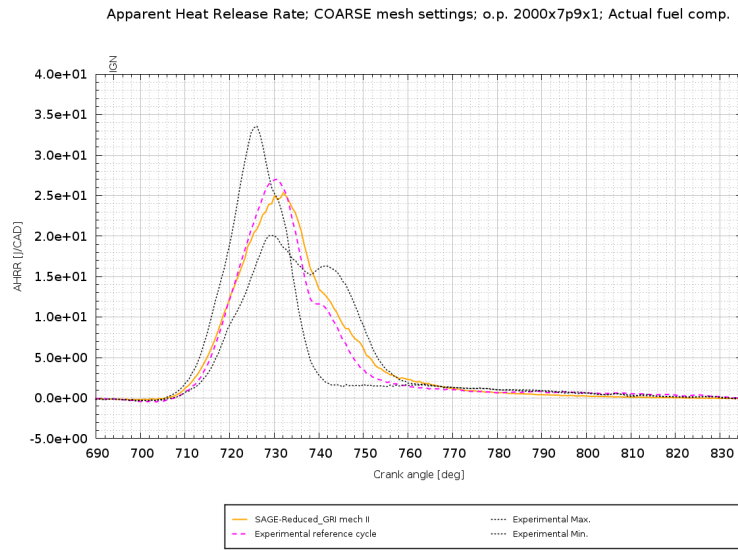


Figure 6.64: Heat release rate in cylinder 1: SAGE-Reduced *GRI-Mech 3.0* and experimental data, Coarse mesh settings, Actual fuel composition

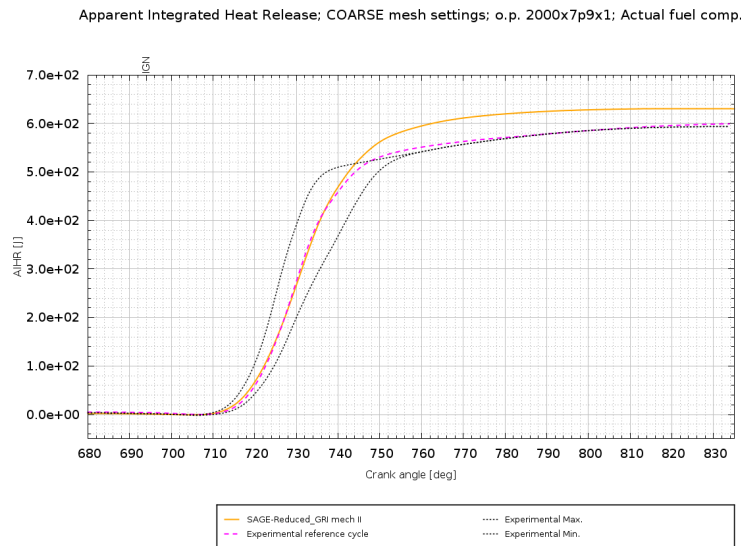


Figure 6.65: Integrated heat release in cylinder 1: SAGE-Reduced *GRI-Mech 3.0* and experimental data, Coarse mesh settings, Actual fuel composition

Fine mesh settings

Figure 6.66 shows a comparison between the results obtained with the simulation SAGE-*GRI-Mech 3.0* and the experimental data for what concerns the Pressure in cylinder 1. The image is focused on the range between 620÷850 crank angle degree. The simulation results can be considered good, but quite overestimated with respect to the experimental pressure values.

Figures 6.67 and 6.68 show that the model trend follows the experimental one quite well, but are slightly overestimated with respect to the experimental values. This mesh can be considered thus quite when coupled with this mechanism. The runtime of this simulation has been 36.652 hours per cycle, using 5 nodes corresponding to 30 cores.

SAGE-GRI mech 3.0 and exp. data comparison; Fine mesh settings; o.p. 2000x7p9x1; Actual fuel comp.

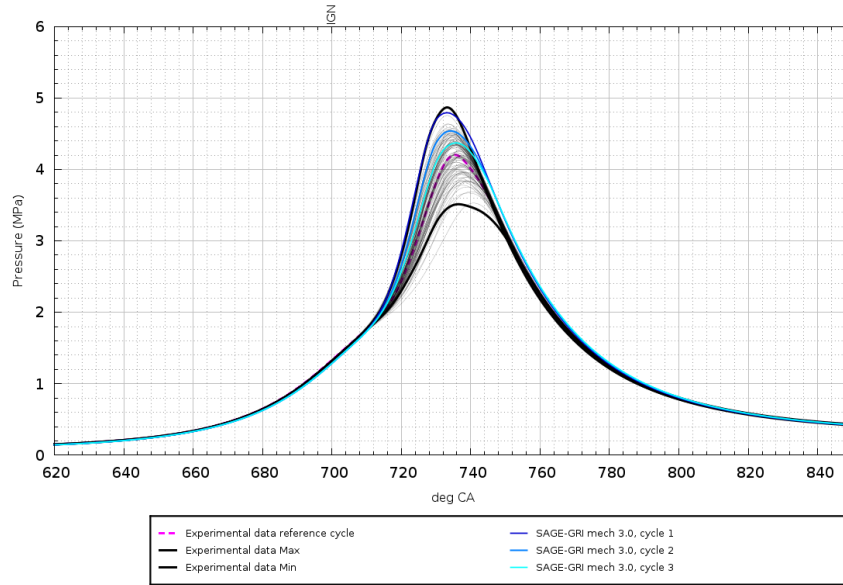


Figure 6.66: Pressure in cylinder 1: SAGE-GRI-Mech 3.0 and experimental data, Fine mesh settings, Actual fuel composition

Apparent Heat Release Rate; FINE mesh settings; o.p. 2000x7p9x1; Actual fuel comp.

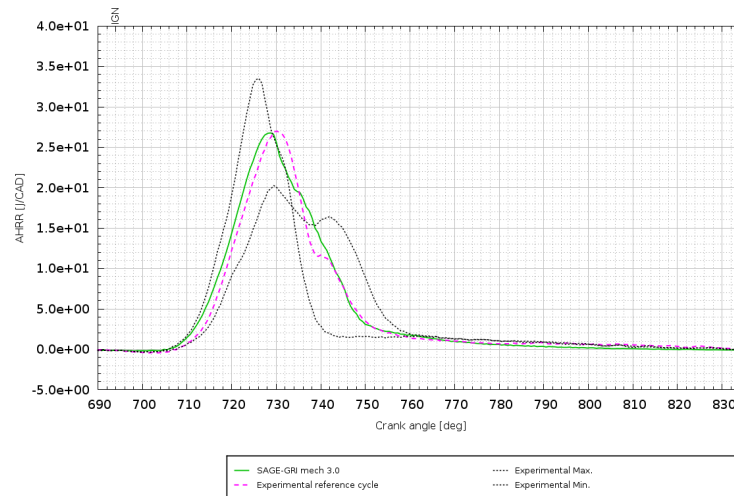


Figure 6.67: Heat release rate in cylinder 1: SAGE-GRI-Mech 3.0 and experimental data, Fine mesh settings, Actual fuel composition

Figures 6.69, 6.70 and 6.71 respectively show the results got with SAGE-USC-Mech II with the *Fine* mesh compared to experimental data, respectively for pressure in cylinder, heat release rate and integrated heat release.

The figures show that the model trend follows the experimental one quite well. This mesh can be considered thus quite when coupled with this mechanism. Notice that this case is the best simulation got with SAGE-USC-Mech II. The runtime of this simulation has been 56.87 hours per cycle, using 5 nodes corresponding to 30 cores.

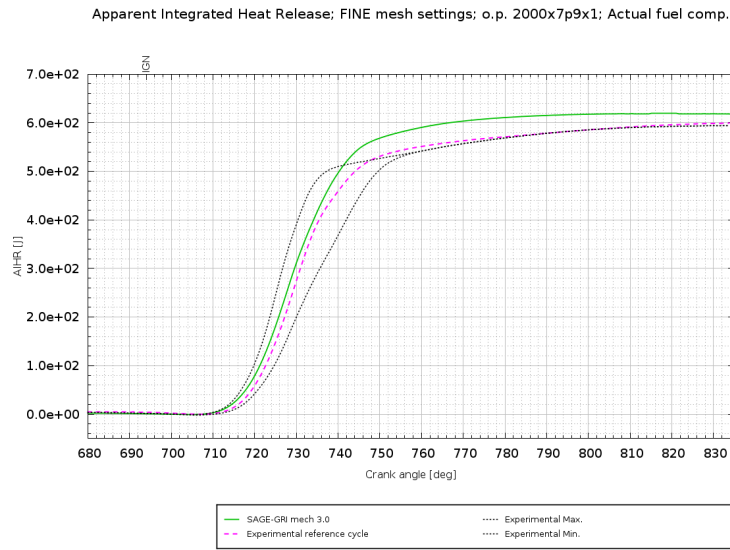


Figure 6.68: Integrated heat rate in cylinder 1: SAGE-*GRI-Mech 3.0* and experimental data, Fine mesh settings, Actual fuel composition

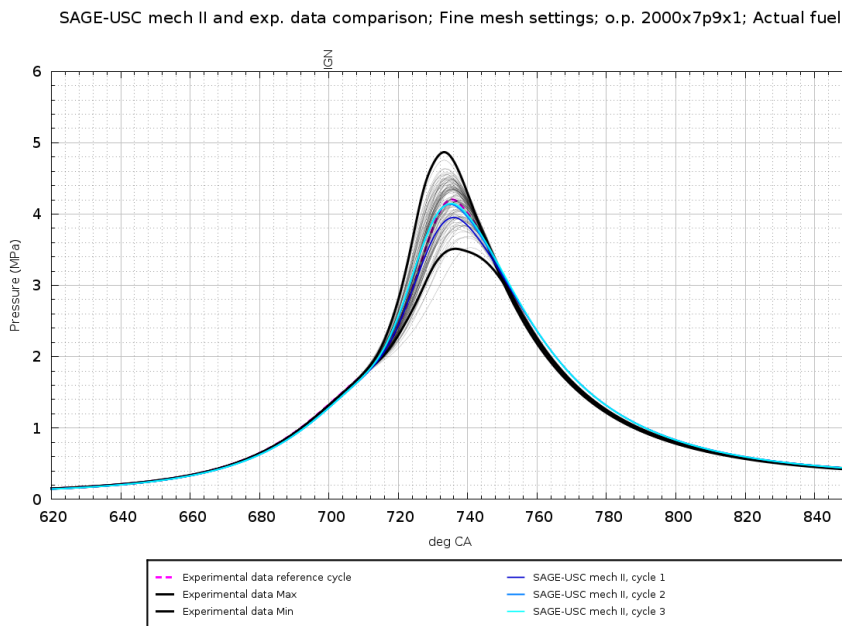


Figure 6.69: Pressure in cylinder 1: SAGE-*USC-Mech II* and experimental data, Fine mesh settings, Actual fuel composition

Figure 6.72 shows the pressure curve obtained with SAGE-*Reduced GRI-Mech 3.0* model, compared with the experimental data available.

The model matches the experimental data quite perfectly. The peak pressure value of the simulation reference cycle, i.e. p_{peak} , is about 4.2 MPa, so the same value of that of the experimental reference cycle. The simulation crank angle degree corresponding to the peak pressure in cylinder 1, i.e. θ_{peak} , is the same of the experimental data, namely 734 deg.

The pressure at the *SA*, i.e. the value of pressure in cylinder 1 corresponding to

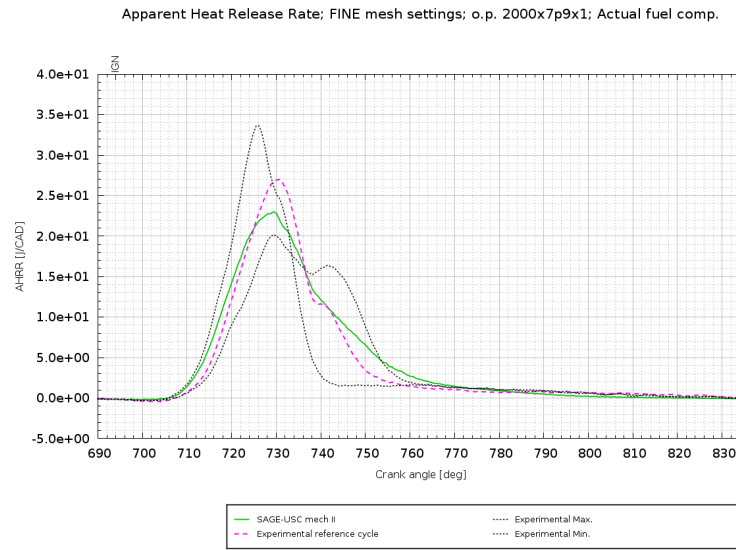


Figure 6.70: Heat release rate in cylinder 1: SAGE-USC-Mech II and experimental data, Fine mesh settings, Actual fuel composition

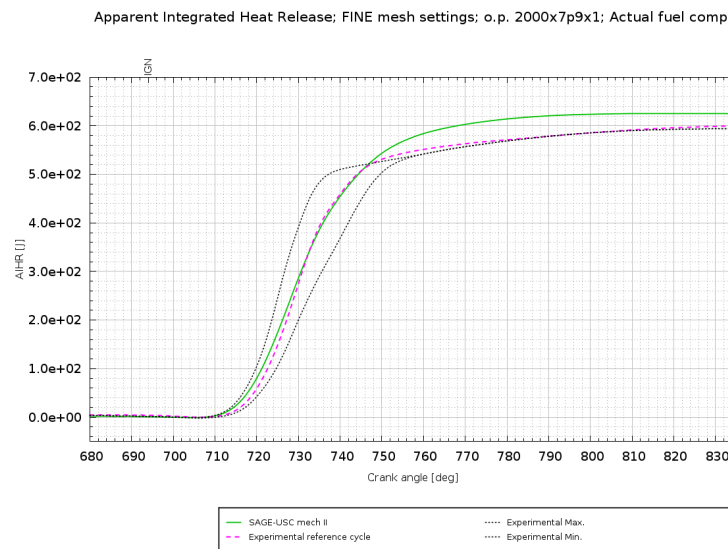


Figure 6.71: Integrated heat rate in cylinder 1: SAGE-USC-Mech II and experimental data, Fine mesh settings, Actual fuel composition

700 crank angle degree, is about 1.4 MPa, for both experimental data and simulation result.

Figures 6.73 and 6.74 show the Heat release rate and the Integrated Heat release, respectively, for what concerns SAGE-Reduced GRI-Mech 3.0 model and experimental data.

As it can be noticed, the results are good, as the model trend follows the experimental one quite well. The model *IHR* is a slightly overestimated with respect to the experimental values after crank angle 745 deg; this happens also for the *HHR* and the pressure profile.

This mesh can be considered thus a good choice if coupled with this mechanism. Some adjustments have to be done, but the results can be considered satisfactory.

SAGE-Reduced_GRI mech 3.0 and exp. data comparison; Fine mesh settings; o.p. 2000x7p9x1; Actual fuel

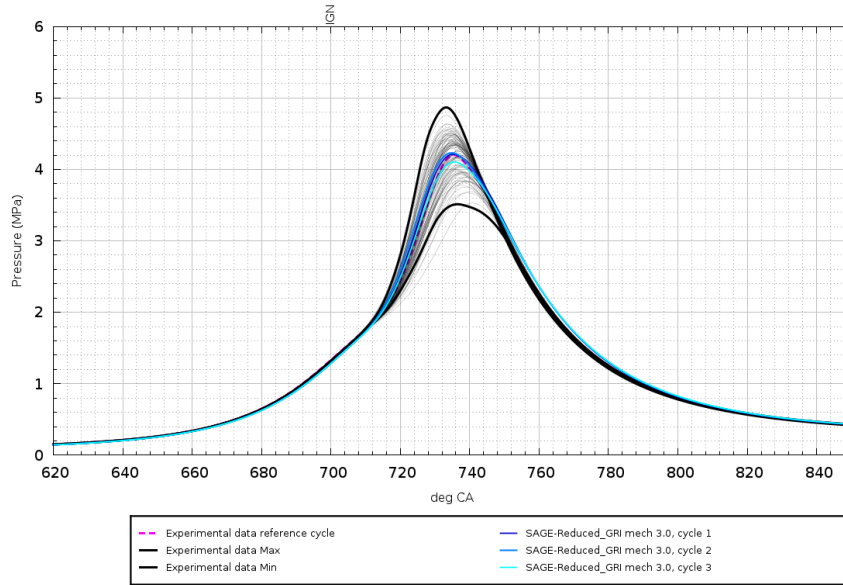


Figure 6.72: Pressure in cylinder 1: SAGE-Reduced GRI-Mech 3.0 and experimental data, Fine mesh settings, Actual fuel composition

Apparent Heat Release Rate; FINE mesh settings; o.p. 2000x7p9x1; Actual fuel comp.

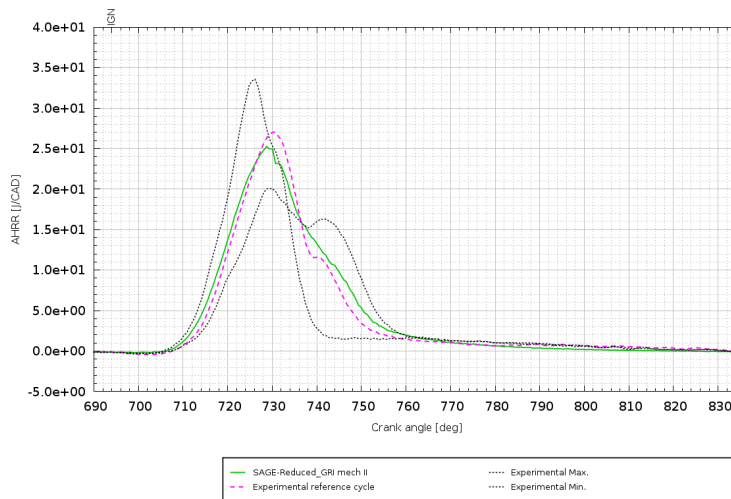


Figure 6.73: Heat release rate in cylinder 1: SAGE-Reduced GRI-Mech 3.0 and experimental data, Fine mesh settings, Actual fuel composition

The runtime of this simulation has been 33.26 hours per cycle, using 5 nodes corresponding to 30 cores.

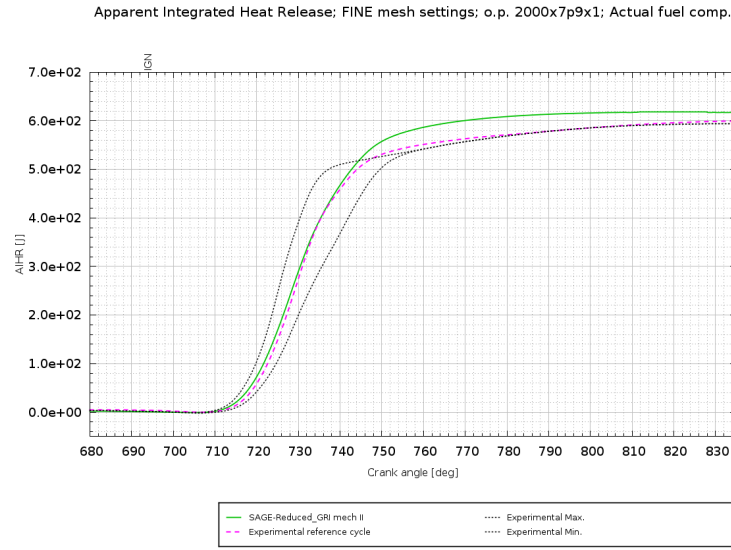


Figure 6.74: Integrated heat rate in cylinder 1: SAGE-Reduced *GRI-Mech 3.0* and experimental data, Fine mesh settings, Actual fuel composition

6.4 3300[rpm] x 7.9[bar] x lambda=1

For what concerns the engine operating point 3300[rpm] x 7.9 [bar] x lambda=1, the simulations in CONVERGE have been carried out just for the fuel *Actual Fuel Composition*, for *Fine* mesh settings, and for the kinetic mechanisms *GRI-Mech 3.0*, *USC-Mech II* and *Reduced GRI-Mech 3.0*.

Table 6.3 summarizes the cases that have been run.

Figure 6.75 displays the resulting pressure curves in cylinder 1 got using SAGE-*GRI-*

Table 6.3: O.P. 3300[rpm] x 7.9 [bar] x lambda=1: simulations cases run

Combustion model	Fuel	Mechanism	Mesh settings
SAGE	Actual fuel	<i>GRI-Mech 3.0</i>	Fine
		<i>USC-Mech II</i>	Fine
		<i>Reduced GRI-Mech 3.0</i>	Fine

Mech 3.0 model with *Fine* mesh settings for this new operating point.

The results are quite good, as the pressure profiles of the simulation cycles are inside the range described by the experimental curves carrying the maximum and minimum peak; nevertheless, the model cycles are not particularly close to the experimental reference cycle for the crank angle degrees around the combustion phase.

One can notice also that the value of the pressure at the spark advance, which for this operating point happens to be at 694 crank angle degree, is not the same for model and for experimental data: the simulation provides underestimated amplitudes, but the different is really small.

The runtime of this simulation has been about 30 hours per cycle, using 5 nodes corresponding to 30 cores.

Figures 6.76 and 6.77 respectively show the results in the matter of pressure in cylinder 1 obtained with SAGE-*USC-Mech II* and SAGE-*Reduced GRI-Mech 3.0* models with *Fine* mesh settings for the new operating point.

One can notice that these mechanisms do not perform good in this case, even if the

SAGE-GRI mech 3.0 and exp. data comparison; FINE mesh settings; o.p. 3300x7p9x1; Actual fuel comp.

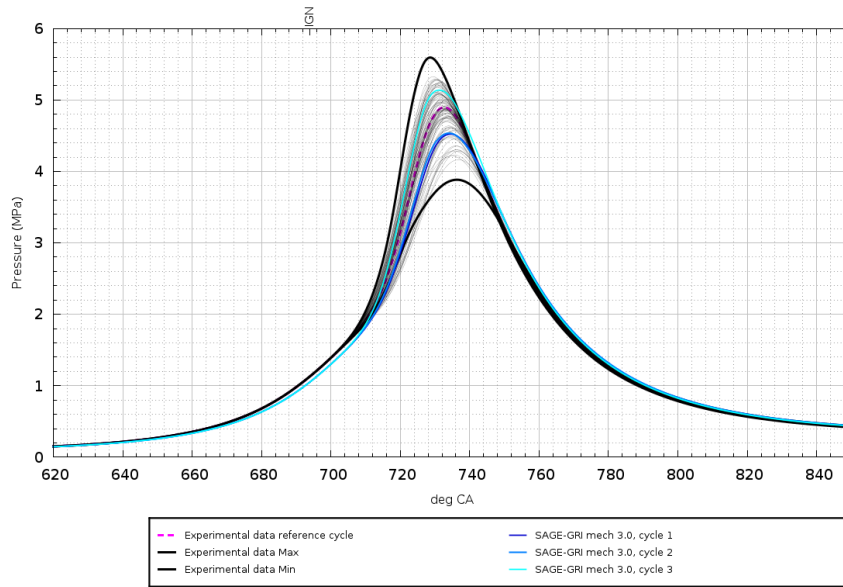


Figure 6.75: Pressure in cylinder 1: SAGE-GRI-Mech 3.0 and experimental data, Fine mesh settings, Actual fuel composition

Reduced GRI-Mech 3.0 behaves better than the other one. In particular, the pressure curves are underestimated with respect to the experimental ones.

The heat release rate and the integrated heat release have not been computed, since

SAGE-USC mech II and exp. data comparison; FINE mesh settings; o.p. 3300x7p9x1; Actual fuel comp.

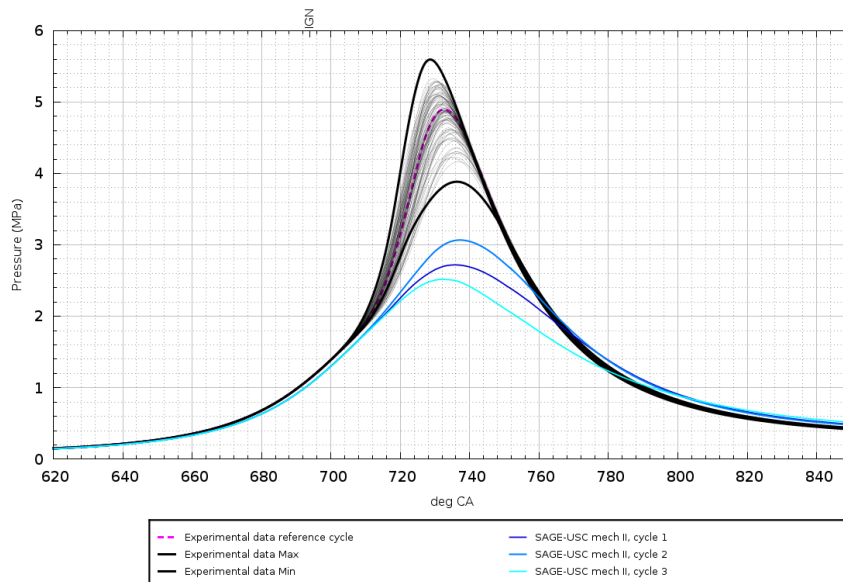


Figure 6.76: Pressure in cylinder 1: SAGE-USC-Mech II and experimental data, Fine mesh settings, Actual fuel composition

just looking at the pressure plots one can understand that some adjustments on the model must be made.

SAGE-Reduced_GRI mech 3.0 and exp. data comparison; FINE mesh settings; o.p. 3300x7p9x1; Actual fuel comp.

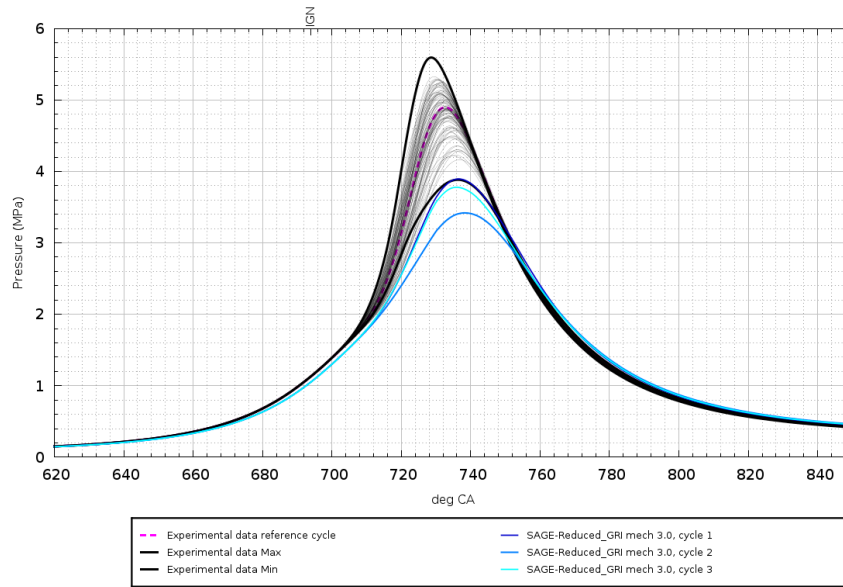


Figure 6.77: Pressure in cylinder 1: SAGE-Reduced GRI-Mech 3.0 and experimental data, Fine mesh settings, Actual fuel composition

The runtime of these simulations has been about 56.95 hours per cycle for the SAGE-USC-Mech II, and for the SAGE-Reduced GRI-Mech 3.0 about 28.95 hours per cycle, using 5 nodes corresponding to 30 cores.

6.5 Conclusions and future developments

In this thesis project lots of CFD simulations (more than 75) have been run. This gave the opportunity to reach a good knowledge of the *SAGE-Detailed Chemistry* model, which is able to simulate in a very effective way the complicated phenomena involving combustion in natural gas engines.

The thorough validation of the different reaction mechanisms used, i.e. *GRI-Mech 3.0*, *USC-Mech II* and *AramcoMech 2.0*, showed that the reactions and the species involved in them are realistic, as they follow satisfactorily the experimental data found in literature. For high pressure conditions, the difference between model results and reality increases, but the trends are the same and the magnitudes of the variables studied, i.e. *ignition delay* and *laminar flame speed*, do not differ too much. The validation has been carried out for pure methane in air.

The section dealing with the mechanisms reduction showed that both the *skeletal* and the *dynamic* techniques are worthwhile with a suitable mesh. The former has been used to reduced the mechanism that turned out to be the one that most of the times provides the best results for the engine simulations and is the less time consuming, i.e. the *GRI-Mech 3.0*. Its *skeletal* reduction, which has been made by selecting particular species to be saved, generated the mechanism named as *Reduced GRI-Mech 3.0*. This mechanism has been validated against the aforementioned experimental data, and it turned out to be very efficient.

The *dynamic* reduction (DMR) has been carried out for the *GRI-Mech 3.0* and the *USC-Mech II* during some engine simulations and provided good results; it is therefore a CONVERGE tool that is definitely recommended for this kind of applications. For what matters the engine simulations, three operating points have been treated, with three different mesh settings ("*Coarse*", "*Fine*" and "*Finest*"), and two different fuel compositions ("*Pure CH₄*" and "*Actual fuel composition*").

The analysis carried out on the engine operating point 2000[rpm]x3.6[bar]x $\lambda=1$ has been deeper than those regarding the others. For this operating point, it has been seen that the *GRI-Mech 3.0* is the mechanism which usually performs as the best one, especially coupled with the *Fine* mesh when using *Pure CH₄* as fuel, and with the *Coarse* mesh when considering the *Actual fuel composition*.

The *USC-Mech II* is able to provide satisfying results when sustained by the *Fine* mesh with *Actual fuel composition*, while, for the same mesh and fuel, the *Reduced GRI-Mech 3.0* gives very good results. The latter case shows that is possible to get optimal results for small runtime.

The *AramcoMech2.0* turned out to be the mechanism that requires the highest runtime and memory. The engine simulation case with the "*Coarse*" mesh and *Pure CH₄* has been the only one that has been brought to conclusion, as the runtime for the other cases was overly long, and persistent restarts were to be made because of memory problems. It is, in fact, a very detailed mechanism, involving lots of reactions and species, so lack of speed has to be expected, especially if coupled to a fine mesh. The results provided by the only completed simulation have not been satisfying, so one can understand that high number of reactions and species does not necessarily entail accuracy.

In all the cases, as expected, using the *Actual fuel composition* provides more accurate results: adding very small percentages of species different from CH₄ can really affect the results. In conclusion, it can be said that this approximation of the engine fuel is optimal.

For what concerns the mesh settings taken into account, the "*Coarse*" and the "*Fine*" meshes can be considered good, especially the latter one, as it provides good results when coupled with all the mechanisms. In all the cases the "*Finest*" mesh does not yield satisfying results, as they always turn out to be underestimated with respect to the experimental data and those provided by the other simulations with the "*Coarse*" and the "*Fine*" meshes. Investigation of the reasons why this happens has been accomplished, and it was found out that with this mesh the y^+ of the simulations

happen to be out of the range chosen for the model, i.e. $20 < y^+ < 200$, during the combustion phase, and therefore the *Law of Wall* does not produce physically realistic results.

The simulations results got for the engine operating point 2000[rpm]x7.9[bar] with lambda=1 are quite satisfying, but some model adjustments should be made in order to fix the issue of the overestimation of the pressure values in the burn out phase.

For what matters the engine operating point 3300[rpm]x7.9[bar] with lambda=1, the simulations run do not provide particularly good results, especially for the *USC-Mech II* and the *Reduced GRI-Mech 3.0*. As a first instance, one of the reasons why this happens can be traced out to the higher engine speed; this could be an issue for the next projects.

Another interesting matter for future developments could be the addition of hydrogen into the fuel composition; experimental data for this case are already available in Politecnico di Torino. The mechanisms considered in this thesis project should be validated also for the new fuel, and one should check whether they can be suitable also for engine simulations.

Acknowledgements

With boundless love and appreciation, I would like to extend my heartfelt gratitude to all the people who supported and helped me in bringing my studies to reality.

First of all, I would love to thank my supervisor at CONVERGENT SCIENCE GmbH, Dr. Rainer Rothbauer, for having believed in me and given me the great occasion to join his team as intern, to access to the equipments and research facilities in order to develop this thesis project, which made me grow up under so many aspects.

My deepest thanks also go to my supervisor at Politecnico di Torino, Prof. Daniela Misul, whose kindness, patience and support are limitless. Sincere thanks also to my co-supervisor, Prof. Mirko Baratta, for his insightful comments and assistance. I will always be grateful to you for having included me into your project, giving me the opportunity to having had this exceptional experience.

Special thanks also to the rest of the CONVERGENT SCIENCE team: Jyothish, Mattia, Vera, Ivona, Pietro, Matteo, Suresh, Edith, and Bugra, for all the support and help they gave me.

Finally, I would like to say a huge "thank you" to all the *loved ones*, that really helped me by supporting and sometimes even putting up with me.

To my mother, for being my most stable benchmark and for having always sustained with all her love and resources.

To my brother Francesco and all my family because, despite the distance, are always there for me.

To my girlfriend Valeria, for being always on my side, no matter what.

To my "old" friends and the wonderful people I met in Torino, for all the moments of lightheartedness that only they can give me, for all the occasions for constructive dialogue, their advices and their frankness, which I always keep as treasures.

Nomenclature

- \mathbf{a} : acceleration vector, [m/s^2];
- a_i : acceleration in the i -th direction, [m/s^2];
- C : reaction constant [*unit depending on the order of reaction*];
- c_i : mass fraction of species i , [-];
- c_p : specific heat at constant pressure, [$J/(kg \cdot K)$];
- c_v : specific heat at constant volume, [$J/(kg \cdot K)$];
- D_t : turbulent diffusion;
- e : total energy per unit mass, [J/kg];
- E_a : activation energy, [kJ/mol];
- E_t : total energy per unit volume, [J/m^3];
- \mathbf{F} : force vector, [N];
- F_i : force in the i -th direction, [N];
- \mathbf{f} : body force vector, [N];
- f_i : body force in the i -th direction, [N];
- HRR : heat release rate, [J/deg];
- IHR : integrated heat release, [J];
- k : coefficient of thermal diffusivity, [$W/(m \cdot K)$];
- $K_{b,i}$: backward reaction rate for the l -th reaction;
- $K_{f,i}$: forward reaction rate for the l -th reaction;
- K_t : the turbulent conductivity;
- l : characteristic length, [m];
- m : mass, [kg];
- \dot{m} : mass flow rate, [kg/s];
- Ma : Mach number;
- \mathcal{M} : molecular weight, [kg/mol];
- n : reaction exponential constant;
- p : pressure, [bar];

Q : heat, [J];
 Q_b : heat supplied, [J];
 Q_l : heat loss, [J];
 \mathbf{q} : heat flux vector, [W/m²];
 P_{ij} : shear tensor;
 Pr : Prandtl number;
 R : individual gas constant, [J/(kg · K)];
 \mathcal{R} : universal gas constant (=83140.34), [J/(kg · mol · K)];
 Re : Reynolds number;
 \mathbf{S} : oriented surface, [m²];
 S_{ij} : mean strain rate tensor;
 T : temperature, [K];
 t : time, [s];
 u : characteristic speed, [m/s];
 u^+ : dimensionless velocity, [-];
 V : volume, [m³];
 \mathbf{v} : velocity vector, [m/s];
 v_i : velocity in the i -th direction, [m/s];
 w_{cl} : combustion laminar speed, [m/s];
 w_r : reaction velocity, [m/s];
 Y_i : mass fraction of the i th species [-];
 y^+ : Normalized wall distance [-];
 α : air-fuel ratio (=ratio between the mass of air and the mass of fuel), [-];
 γ : ratio between c_p and c_v , [-];
 ε : dissipation of turbulent kinetic energy;
 λ (*lambda*) : equivalence air-fuel ratio (=ratio between actual air-fuel ratio and the stoichiometric air-fuel ratio), [-];
 μ : dynamic viscosity coefficient, [N · s/m²];
 ν : kinematic viscosity coefficient, [m²/s];
 $\nu'_{l,i}, \nu''_{l,i}$: stoichiometric coefficients for the i -th reactant;
 ρ : density, [kg/m³];
 τ_a : ignition delay, [s];
 τ_{ii} : normal stress in the i -th direction, [N/m²];
 τ_{ij} : shear stress in directions i and j , [N/m²];
 ϕ : fuel-air equivalence ratio (=ratio of the fuel to air ratio), [-];

Φ : dissipation function;

$\dot{\omega}_i$: rate of production of species i due to chemical reactions;

χ_b : mass fraction of burned fuel, [-];

$[X_i]$: molar concentration of the i -th species, [$kmol/m^3$];

$\frac{\partial(\cdot)}{\partial t}$: time derivative;

$\frac{D(\cdot)}{Dt}$: substantial derivative;

∇ : vector differential operator;

$\nabla(\cdot)$: gradient;

$\nabla \cdot (\cdot)$: divergence;

$\nabla^2(\cdot)$: Laplacian;

Acronyms

- A/F:** Air to Fuel ratio;
- AMR:** Adaptive Mesh Refinement;
- BC:** Boundary condition;
- BDC:** Bottom dead centre;
- C2C:** Cycle to Cycle;
- CAD:** Crank Angle Degree;
- CEQ:** Chemical Equilibrium;
- CFD:** Computational Fluid Dynamics;
- CNG:** Compressed Natural Gas;
- CR:** Compression ratio;
- CRF:** Centro di ricerche FIAT;
- CTC:** Characteristic Time Combustion;
- DENERG:** Dipartimento di Energia (Politecnico di Torino);
- DNS:** Direct Numerical Simulation;
- DRG:** Directed Relation Graph;
- DRGEP:** Directed Relation Graph with Error Propagation;
- DRGEP-SA:** Directed Relation Graph with Error Propagation and Sensitivity Analysis;
- DMR:** Dynamic Mechanism Reduction;
- ECFM:** Extended Coherent Flame Model;
- ECFM3Z:** Extended Coherent Flame Model with the 3Z mixing model;
- EGR:** Exhaust Gas Recirculation;
- EVC:** Exhaust valve closing;
- EVO:** Exhaust valve opening;
- FGM:** Flamelet Generated Manifold;
- FIAT:** Fabbrica Italiana Automobili Torino;
- GRI:** Gas Research Institute;

HF: High frequency;
HR: Heat release;
HRR: Heat release rate;
ICE: Internal combustion engine;
IC: Initial condition;
IGN: Ignition;
IHR: Integrated heat release;
IVC: Intake valve closing;
IVO: Intake valve opening;
LES: Large Eddy Simulation;
LF: Low frequency;
LFS: Laminar flame speed;
MFB: Mass fraction burned;
ODE: Ordinary differential equation;
RIF: Representative Interactive Flamelet;
SA: Spark advance;
TDC: Top dead centre;
TKE: Turbulent Kinetic Energy;
UEGO: Universal Exhaust Gas-Oxygen;
USC: description

List of figures

- Figure 2.1** Surface forces in the x-direction exerted on the fluid element, from [4];
- Figure 2.2** CONVERGE CFD software logo;
- Figure 2.3** Example of *Base grid*;
- Figure 2.4** Examples of *Fixed Embedding*, fig. 2.4a example 1 (Nozzle), fig. 2.4b example 2 (Boundary), fig. 2.4c example 3 (Cylinder);
- Figure 2.5** *Adaptive Mesh Refinement (AMR)*, fig. 2.5a AMR, fig. 2.5b Example 1: AMR capturing flapping jet found in intake flow simulation, fig. 2.5c Example 2: AMR capturing flame front for spark-ignited engine simulation using detailed chemistry;
- Figure 3.1** Engine and test bench under construction;
- Figure 3.2** Intake system, Figure 3.2a Throttle body: wire control of throttle opening, Figure 3.2b Throttle body: frontal view of the butterfly valve, Figure 3.2c Turbocharger, Figure 3.2d Inter-cooler air-water;
- Figure 3.3** *Tartarini* Meta M pressure regulator, Figure 3.3a High pressure sensor *Keller Pa 22 M*, Figure 3.3b Low pressure sensor *Kavlico P4000*, Figure 3.3c *Tartarini* pressure regulator;
- Figure 3.4** Gas feeding rail;
- Figure 3.5** Pressure sensors, Figure 3.5a Piezo-resistive traducer 4073 A10 by *Kistler*, Figure 3.5b Miniaturized piezo-resistive traducer 4005BASF by *Kistler*, Figure 3.5c *Kistler* piezo-electric traducer 6052C;
- Figure 3.6** Intake pressure transducers location;
- Figure 3.7** Dynamo-meter FE 260-S by *Borghini and Saveri*;
- Figure 3.8** Experimental data plot: Pressure in cylinder, complete engine cycle, O.P. 2000 [rpm] x 3.6 [bar] x lambda=1;
- Figure 3.9** Experimental data plot: Pressure in cylinder, zoom around peak Pressure, O.P. 2000 [rpm] x 3.6 [bar] x lambda=1;
- Figure 3.10** Experimental data plot: Pressure in cylinder, complete engine cycle, O.P. 2000 [rpm] x 7.9 [bar] x lambda=1;
- Figure 3.11** Experimental data plot: Pressure in cylinder, zoom around peak Pressure, O.P. 2000 [rpm] x 7.9 [bar] x lambda=1;
- Figure 3.12** Experimental data plot: Pressure in cylinder, complete engine cycle, O.P. 3300 [rpm] x 7.9 [bar] x lambda=1;

- Figure 3.13** Experimental data plot: Pressure in cylinder, zoom around peak Pressure, O.P. 3300 [rpm] x 7.9 [bar] x lambda=1;
- Figure 4.1** Engine CAD geometry, Figure 4.1a Engine CAD geometry (view 1), Figure 4.1b Engine CAD geometry (view 2), Figure 4.1c Engine CAD geometry (view 3);
- Figure 4.2** Regions;
- Figure 4.3** Ignition modelling;
- Figure 4.4** Modelling Engine Spark with Energy Sources, fig. 4.4a Ignition modelling: geometry, fig. 4.4b Additional embedding;
- Figure 5.1** *GRI-Mech 3.0*: mech.dat file (partial);
- Figure 5.2** *GRI-Mech 3.0*: therm.dat file (partial);
- Figure 5.3** *GRI-Mech 3.0*: transport.dat file (partial);
- Figure 5.4** Ignition delay for $p = 0.4\text{MPa}$, $\phi = 2$;
- Figure 5.5** Ignition delay at spark conditions for o.p. 2000 [rpm] x 3.6 [bar] x lambda=1: 694 deg crank angle, $p = 7$ bar, $\phi = 1[-]$;
- Figure 5.6** Ignition delay at engine conditions for o.p. 2000 [rpm] x 3.6 [bar] x lambda=1: 710 deg crank angle, $p = 7$ bar, $\phi = 1[-]$;
- Figure 5.7** Laminar flame speed for pure CH_4 , $p = 1\text{bar}$, $T = 298\text{K}$;
- Figure 5.8** Laminar flame speed for pure CH_4 , $p = 5\text{bar}$, $T = 400\text{K}$;
- Figure 5.9** Laminar flame speed for pure CH_4 , $p = 5\text{bar}$, $T = 500\text{K}$;
- Figure 5.10** Laminar flame speed for pure CH_4 , $p = 5\text{bar}$, $T = 600\text{K}$;
- Figure 5.11** Laminar flame speed for pure CH_4 , $p = 20\text{bar}$, $T = 400\text{K}$;
- Figure 5.12** Laminar flame speed for pure CH_4 , $p = 20\text{bar}$, $T = 500\text{K}$;
- Figure 5.13** Laminar flame speed at spark conditions for o.p. 2000 [rpm] x 3.6 [bar] x lambda=1: 694 deg crank angle, $p = 7$ bar, $T = 700\text{K}$;
- Figure 5.14** Laminar flame speed at engine conditions for o.p. 2000 [rpm] x 3.6 [bar] x lambda=1: 694 deg crank angle, $p = 10$ bar, $T = 800\text{K}$;
- Figure 5.15** Laminar flame speed at peak pressure conditions for o.p. 2000 [rpm] x 3.6 [bar] x lambda=1: 734 deg crank angle, $p = 25$ bar, $T = 1900\text{K}$;
- Figure 5.16** Simplified example of directed relation graph (DRG), Original DRG (a), DRG reduced (b), from [3];
- Figure 5.17** Detailed GRI-Mech 3.0 vs Reduced GRI-Mech 3.0: Ignition delay for $p = 0.4\text{MPa}$, $\phi = 2$;
- Figure 5.19** Detailed GRI-Mech 3.0 vs Reduced GRI-Mech 3.0: Laminar flame speed for pure CH_4 , $p = 1\text{bar}$, $T = 298\text{K}$;
- Figure 5.20** Detailed GRI-Mech 3.0 vs Reduced GRI-Mech 3.0: Laminar flame speed for pure CH_4 , $p = 5\text{bar}$, $T = 400\text{K}$;
- Figure 5.21** Detailed GRI-Mech 3.0 vs Reduced GRI-Mech 3.0: Laminar flame speed for pure CH_4 , $p = 5\text{bar}$, $T = 500\text{K}$;

- Figure 5.22** Detailed GRI-Mech 3.0 vs Reduced GRI-Mech 3.0: Laminar flame speed for pure CH₄, $p = 5\text{bar}$, $T = 600\text{K}$;
- Figure 5.23** Detailed GRI-Mech 3.0 vs Reduced GRI-Mech 3.0: Laminar flame speed for pure CH₄, $p = 20\text{bar}$, $T = 400\text{K}$;
- Figure 5.24** Detailed GRI-Mech 3.0 vs Reduced GRI-Mech 3.0: Laminar flame speed for pure CH₄, $p = 20\text{bar}$, $T = 500\text{K}$;
- Figure 5.25** Detailed GRI-Mech 3.0 vs Reduced GRI-Mech 3.0: Laminar flame speed at spark conditions for o.p. 2000 [rpm] x 3.6 [bar] x lambda=1: 694 deg crank angle, $p = 7\text{bar}$, $T = 700\text{K}$;
- Figure 5.26** Detailed GRI-Mech 3.0 vs Reduced GRI-Mech 3.0: Laminar flame speed at peak pressure conditions for o.p. 2000 [rpm] x 3.6 [bar] x lambda=1: 734 deg crank angle, $p = 25\text{bar}$, $T = 1900\text{K}$;
- Figure 6.1** Pressure in cylinder 1: SAGE-*GRI-Mech 3.0* and experimental data, Coarse mesh settings, Pure CH₄;
- Figure 6.2** Heat release rate (HRR): SAGE-*GRI-Mech 3.0* and experimental data, Coarse mesh settings, Pure CH₄;
- Figure 6.3** Integrated Heat release (IHR): SAGE-*GRI-Mech 3.0* and experimental data, Coarse mesh settings, Pure CH₄;
- Figure 6.4** Pressure in cylinder 1: SAGE-*USC-Mech II* and experimental data, Coarse mesh settings, Pure CH₄;
- Figure 6.5** Heat release rate (HRR): SAGE-*USC-Mech II* and experimental data, Coarse mesh settings, Pure CH₄;
- Figure 6.6** Integrated Heat release (IHR): SAGE-*USC-Mech II* and experimental data, Coarse mesh settings, Pure CH₄;
- Figure 6.7** Pressure in cylinder 1: SAGE-*AramcoMech 2.0* and experimental data, Coarse mesh settings, Pure CH₄;
- Figure 6.8** Heat release rate (HRR): SAGE-*Aramco-Mech2.0* and experimental data, Coarse mesh settings, Pure CH₄;
- Figure 6.9** Integrated Heat release (IHR): SAGE-*Aramco-Mech2.0* and experimental data, Coarse mesh settings, Pure CH₄;
- Figure 6.10** Pressure in cylinder 1: SAGE-*Reduced GRI-Mech 3.0* and experimental data, Coarse mesh settings, Pure CH₄;
- Figure 6.11** Heat release rate (HRR): SAGE-*Reduced GRI-Mech 3.0* and experimental data, Coarse mesh settings, Pure CH₄;
- Figure 6.12** Integrated Heat release (IHR): SAGE-*Reduced GRI-Mech 3.0* and experimental data, Coarse mesh settings, Pure CH₄;
- Figure 6.13** Pressure in cylinder 1: SAGE-*GRI-Mech 3.0* and experimental data, Finest mesh settings, Pure CH₄;
- Figure 6.14** Heat release rate (HRR): SAGE-*GRI-Mech 3.0* and experimental data, Finest mesh settings, Pure CH₄;
- Figure 6.15** Integrated Heat release (IHR): SAGE-*GRI-Mech 3.0* and experimental data, Finest mesh settings, Pure CH₄;
- Figure 6.16** Pressure in cylinder 1: SAGE-*USC-Mech II* and experimental data, Finest mesh settings, Pure CH₄;

- Figure 6.17** Heat release rate (HRR): SAGE-*USC-Mech II* and experimental data, Finest mesh settings, Pure CH₄;
- Figure 6.18** Integrated Heat release (IHR): SAGE-*USC-Mech II* and experimental data, Finest mesh settings, Pure CH₄;
- Figure 6.19** Pressure in cylinder 1: SAGE-*Reduced GRI-Mech 3.0* and experimental data, Finest mesh settings, Pure CH₄;
- Figure 6.20** Heat release rate (HRR): SAGE-*Reduced GRI-Mech 3.0* and experimental data, Finest mesh settings, Pure CH₄;
- Figure 6.21** Integrated Heat release (IHR): SAGE-*Reduced GRI-Mech 3.0* and experimental data, Finest mesh settings, Pure CH₄;
- Figure 6.22** Pressure in cylinder 1: SAGE-*GRI-Mech 3.0* and experimental data, Fine mesh settings, Pure CH₄;
- Figure 6.23** Heat release rate (HRR): SAGE-*GRI-Mech 3.0* and experimental data, Fine mesh settings, Pure CH₄;
- Figure 6.24** Integrated Heat release (IHR): SAGE-*GRI-Mech 3.0* and experimental data, Fine mesh settings, Pure CH₄;
- Figure 6.25** Pressure in cylinder 1: SAGE-*USC-Mech II* and experimental data, Fine mesh settings, Pure CH₄;
- Figure 6.26** Heat release rate (HRR): SAGE-*USC-Mech II* and experimental data, Fine mesh settings, Pure CH₄;
- Figure 6.27** Integrated Heat release (IHR): SAGE-*USC-Mech II* and experimental data, Fine mesh settings, Pure CH₄;
- Figure 6.28** Pressure in cylinder 1: SAGE-*Reduced GRI-Mech 3.0* and experimental data, Fine mesh settings, Pure CH₄;
- Figure 6.29** Heat release rate (HRR): SAGE-*Reduced GRI-Mech 3.0* and experimental data, Fine mesh settings, Pure CH₄;
- Figure 6.30** Integrated Heat release (IHR): SAGE-*Reduced GRI-Mech 3.0* and experimental data, Fine mesh settings, Pure CH₄;
- Figure 6.31** Pressure in cylinder 1: SAGE-*GRI-Mech 3.0 (DMR)* and experimental data, Fine mesh settings, Pure CH₄;
- Figure 6.32** Heat release rate (HRR): SAGE-*GRI-Mech 3.0 (DMR)* and experimental data, Fine mesh settings, Pure CH₄;
- Figure 6.33** Integrated Heat release (IHR): SAGE-*GRI-Mech 3.0 (DMR)* and experimental data, Fine mesh settings, Pure CH₄;
- Figure 6.34** Pressure in cylinder 1: SAGE-*USC-Mech II (DMR)* and experimental data, Fine mesh settings, Pure CH₄;
- Figure 6.35** Heat release rate (HRR): SAGE-*USC-Mech II (DMR)* and experimental data, Fine mesh settings, Pure CH₄;
- Figure 6.36** Integrated Heat release (IHR): SAGE-*USC-Mech II (DMR)* and experimental data, Fine mesh settings, Pure CH₄;
- Figure 6.37** Pressure in cylinder 1: Mechanisms comparison, Coarse mesh settings, Pure CH₄;

- Figure 6.38** Pressure in cylinder 1: Mechanisms comparison, Finest mesh settings, Pure CH₄;
- Figure 6.39** Pressure in cylinder 1: Mechanisms comparison, Fine mesh settings, Pure CH₄;
- Figure 6.40** Pressure in cylinder 1: Mesh settings comparison; experimental data vs SAGE-GRI-Mech 3.0;
- Figure 6.41** Number of cells cylinder 1: Mesh settings comparison; SAGE-GRI-Mech 3.0;
- Figure 6.42** Mesh settings comparison on *Velocity*, SAGE-GRI-Mech 3.0 with Pure CH₄, Figure 6.42a *Velocity: Coarse* mesh settings, SAGE-GRI-Mech 3.0 with Pure CH₄, Figure 6.42b *Velocity: Fine* mesh settings, SAGE-GRI-Mech 3.0 with Pure CH₄, Figure 6.42c *Velocity: Finest* mesh settings, SAGE-GRI-Mech 3.0 with Pure CH₄;
- Figure 6.43** Mesh settings comparison on *Temperature* (Iso-surface at $T = 1500\text{K}$), SAGE-GRI-Mech 3.0 with Pure CH₄, Figure 6.43a *Temperature* (Iso-surface at $T = 1500\text{K}$): *Coarse* mesh settings, SAGE-GRI-Mech 3.0 with Pure CH₄, Figure 6.43b *Temperature* (Iso-surface at $T = 1500\text{K}$): *Fine* mesh settings, SAGE-GRI-Mech 3.0 with Pure CH₄, Figure 6.43c *Temperature* (Iso-surface at $T = 1500\text{K}$): *Finest* mesh settings, SAGE-GRI-Mech 3.0 with Pure CH₄;
- Figure 6.44** *TKE*: Mesh settings comparison, SAGE-GRI-Mech 3.0 with Pure CH₄, Figure 6.44a *TKE: Coarse* mesh settings, SAGE-GRI-Mech 3.0 with Pure CH₄, Figure 6.44b *TKE: Fine* mesh settings, SAGE-GRI-Mech 3.0 with Pure CH₄, Figure 6.44c *TKE: Finest* mesh settings, SAGE-GRI-Mech 3.0 with Pure CH₄;
- Figure 6.45** Mesh settings comparison on *TKE* from above, Figure 6.45a *TKE* from above: *Coarse* mesh settings, SAGE-GRI-Mech 3.0 with Pure CH₄, Figure 6.45b *TKE* from above: *Fine* mesh settings, SAGE-GRI-Mech 3.0 with Pure CH₄, Figure 6.45c *TKE* from above: *Finest* mesh settings, SAGE-GRI-Mech 3.0 with Pure CH₄;
- Figure 6.46** Mesh settings comparison on y^+ , SAGE-GRI-Mech 3.0 with Pure CH₄, Figure 6.46a y^+ : *Coarse* mesh settings, SAGE-GRI-Mech 3.0 with Pure CH₄, Figure 6.46b y^+ : *Fine* mesh settings, SAGE-GRI-Mech 3.0 with Pure CH₄, Figure 6.46c y^+ : *Finest* mesh settings, SAGE-GRI-Mech 3.0 with Pure CH₄;
- Figure 6.47** y^+ on the LINER: Mesh settings comparison; SAGE-GRI-Mech 3.0;
- Figure 6.48** Pressure in cylinder 1: Mesh settings comparison; experimental data vs SAGE-USC-Mech II;
- Figure 6.49** Pressure in cylinder 1: Mesh settings comparison; experimental data vs SAGE-Reduced GRI-Mech 3.0;
- Figure 6.50** Pressure in cylinder 1: Fuels comparison; SAGE-GRI-Mech 3.0; *Coarse* mesh settings;
- Figure 6.51** Pressure in cylinder 1: Fuels comparison; SAGE-USC-Mech II; *Coarse* mesh settings;
- Figure 6.52** Pressure in cylinder 1: Fuels comparison; SAGE-Reduced GRI-Mech 3.0; *Coarse* mesh settings;
- Figure 6.53** Pressure in cylinder 1: Fuels comparison; SAGE-GRI-Mech 3.0; *Fine* mesh settings;

Figure 6.54 Pressure in cylinder 1: Fuels comparison; SAGE-*USC-Mech II*; *Fine* mesh settings;

Figure 6.55 Pressure in cylinder 1: Fuels comparison; SAGE-*Reduced GRI-Mech 3.0*; *Fine* mesh settings;

Figure 6.56 Pressure in cylinder 1: Fuels comparison; SAGE-*GRI-Mech 3.0*; *Finest* mesh settings;

Figure 6.57 Pressure in cylinder 1: SAGE-*GRI-Mech 3.0* and experimental data, Coarse mesh settings, Actual fuel composition;

Figure 6.58 Heat release rate in cylinder 1: SAGE-*GRI-Mech 3.0* and experimental data, Coarse mesh settings, Actual fuel composition;

Figure 6.59 Integrated heat rate in cylinder 1: SAGE-*GRI-Mech 3.0* and experimental data, Coarse mesh settings, Actual fuel composition;

Figure 6.60 Pressure in cylinder 1: SAGE-*USC-Mech II* and experimental data, Coarse mesh settings, Actual fuel composition;

Figure 6.61 Heat release rate in cylinder 1: SAGE-*USC-Mech II* and experimental data, Coarse mesh settings, Actual fuel composition;

Figure 6.62 Integrated heat release in cylinder 1: SAGE-*USC-Mech II* and experimental data, Coarse mesh settings, Actual fuel composition;

Figure 6.63 Pressure in cylinder 1: SAGE-*Reduced GRI-Mech 3.0* and experimental data, Coarse mesh settings, Actual fuel composition;

Figure 6.64 Heat release rate in cylinder 1: SAGE-*Reduced GRI-Mech 3.0* and experimental data, Coarse mesh settings, Actual fuel composition;

Figure 6.65 Integrated heat release in cylinder 1: SAGE-*Reduced GRI-Mech 3.0* and experimental data, Coarse mesh settings, Actual fuel composition;

Figure 6.66 Pressure in cylinder 1: SAGE-*GRI-Mech 3.0* and experimental data, *Fine* mesh settings, Actual fuel composition;

Figure 6.67 Heat release rate in cylinder 1: SAGE-*GRI-Mech 3.0* and experimental data, *Fine* mesh settings, Actual fuel composition;

Figure 6.68 Integrated heat rate in cylinder 1: SAGE-*GRI-Mech 3.0* and experimental data, *Fine* mesh settings, Actual fuel composition;

Figure 6.69 Pressure in cylinder 1: SAGE-*USC-Mech II* and experimental data, *Fine* mesh settings, Actual fuel composition;

Figure 6.70 Heat release rate in cylinder 1: SAGE-*USC-Mech II* and experimental data, *Fine* mesh settings, Actual fuel composition;

Figure 6.71 Integrated heat rate in cylinder 1: SAGE-*USC-Mech II* and experimental data, *Fine* mesh settings, Actual fuel composition;

Figure 6.72 Pressure in cylinder 1: SAGE-*Reduced GRI-Mech 3.0* and experimental data, *Fine* mesh settings, Actual fuel composition;

Figure 6.73 Heat release rate in cylinder 1: SAGE-*Reduced GRI-Mech 3.0* and experimental data, *Fine* mesh settings, Actual fuel composition;

Figure 6.74 Integrated heat rate in cylinder 1: SAGE-*Reduced GRI-Mech 3.0* and experimental data, *Fine* mesh settings, Actual fuel composition;

Figure 6.75 Pressure in cylinder 1: SAGE-*GRI-Mech 3.0* and experimental data, Fine mesh settings, Actual fuel composition;

Figure 6.76 Pressure in cylinder 1: SAGE-*USC-Mech II* and experimental data, Fine mesh settings, Actual fuel composition;

Figure 6.77 Pressure in cylinder 1: SAGE-*Reduced GRI-Mech 3.0* and experimental data, Fine mesh settings, Actual fuel composition.

List of tables

Table 2.1: RANS Turbulence models, from [1];

Table 3.1: *Fiat FIRE 1.4 16V Turbo CNG* engine main data;

Table 3.2: Engine operating points considered;

Table 4.1: COARSE mesh settings: Fixed embeddings settings specifications;

Table 4.2: COARSE mesh settings: AMR settings specifications;

Table 4.3: FINE mesh settings: AMR settings specifications;

Table 4.4: FINEST mesh settings: Fixed embeddings settings specifications;

Table 4.5: FINEST mesh settings: AMR settings specifications;

Table 5.1: Mechanisms specifications;

Table 5.2: Mechanisms validation cases for laminar flame speed;

Table 6.1: O.P. 2000[rpm] x 3.6 [bar] x lambda=1: simulations cases run;

Table 6.2: O.P. 2000[rpm] x 7.9 [bar] x lambda=1: simulations cases run;

Table 6.3: O.P. 3300[rpm] x 7.9 [bar] x lambda=1: simulations cases run.

Bibliography

- [1] "An Introduction To Computational Fluid Dynamics: The Finite Volume Method"; Second edition; H. K. VERSTEEG, W. MALALASEKERA;
- [2] "Computational Methods for Fluid Dynamics"; 3rd edition; J.H. FERZIGER, M.PERIC;
- [3] "CONVERGE v2.3 Manual" Richards, K. J. Senecal, P. K., and Pomraning, E., Convergent Science, Inc., Madison, WI (2017);
- [4] "COMPUTATIONAL FLUID DYNAMICS, The Basics with Applications", John D. Anderson, Jr., Department of Aerospace Engineering, University of Maryland, McGraw-Hill, Inc.;
- [5] "NUMERICAL DESIGN OF THERMAL SYSTEMS", Second edition, Adriano Sciacovelli, Vittorio Verda, Romano Borchiellini, CLUT;
- [7] "Computational Fluid Mechanics and Heat transfer", Third edition, Richard H. Pletcher, John C. Tannehill, Dale A. Anderson
- [8] "Simulation of the ensemble and cycle-resolved combustion process in a NG-H2 engine", Paolo De Angelis, Master's thesis, Politecnico di Torino;
- [9] Michael F. J. Brunt and Andrew L. Emtage. "Evaluation of Burn Rate Routines and Analysis Errors". In: *SAE Technical Paper*. 970037. SAE International, Feb. 1997;
- [10] Peter Bradshaw and George P. Huang, "The Law of Wall in Turbulent Flow.", Proceedings: Mathematical and Physical Sciences, vol. 451, no. 1941, 1995, pp. 165-188, JSTOR, www.jstor.org/stable/52798;
- [11] "An Introduction to Combustion: Concepts and Applications", Stephen R. Turns, Second edition, McGraw-Hill Higher Education;
- [12] "Development of an enhanced LFS model of methane-hydrogen blends for IC engine applications", Damiano Mauro, Master's thesis, Politecnico di Torino;
- [13] "Motori a combustione interna" G. Ferrari. Il Capitello, 1996. ISBN: 9788874889716;
- [14] "3D-CFD Simulation of Combustion Process in a NG Engine by Adopting a LFS Submodel from Detailed Kinetic Mechanism", Prashant Goel, Master's thesis, Politecnico di Torino;
- [15] "CHEMICAL KINETICS", Edited by Vivek Patel;
- [16] "IGNITION DELAY CHARACTERISTICS OF METHANE FUELS", L. J. SPADACCINI and M. B. COLKET III, United Technologies Research Center, East Hartford, CT06108, U.S.A.;